Fabrication and characterization of a magnetic tunnel transistor with an epitaxial spin valve by the shadow mask technique

Dissertation

zur Erlangung des Doktorgrades der Naturwissenschaften
(Dr. rer. nat.)
der Fakultät für Physik
der Universität Regensburg

vorgelegt von

Julien Vigroux
aus Paris

2010

Promotionsgesuch eingereicht am: 25.03.2010
Die Arbeit wurde angeleitet von: Prof. Dr. Günther Bayreuther
Datum des Promotionskolloquiums: 19.08.2010

Prüfungsausschuss:

Vorsitzender: Prof. Dr . J. Schliemann

Erstgutachter: Prof. Dr . G. Bayreuther

Zweitgutachter: Prof. Dr . J. Repp

Weiterer Prüfer: Prof. Dr . C. Strunk

Contents

List of Figures **iii**

Nomenclature **v**

1 Introduction **1**
1.1 Two terminal spintronics 1
1.2 Hot electron devices 3
1.3 Spin polarized hot electron transistor 4

2 Theory of the Magnetic Tunnel Transistor **7**
2.1 Tunnel barrier 7
2.1.1 Operation Principle 7
2.1.2 Tunnel emitter 10
2.2 Transport in the metallic base 11
2.2.1 Spin valve 12
2.2.2 Hot electron scattering in the spin valve base 14
2.3 Schottky diodes 19
2.3.1 Principle 19
2.3.2 Forward bias characteristics 20
2.3.3 Reverse bias characteristics 21
2.3.4 Schottky collector 21
2.4 Transport properties in a MTT:a phenomenological model 24
2.5 Transport properties of the magnetic tunnel transistor 25
2.5.1 Bias dependence of the collector current 25
2.5.2 Influence of structural defects 28
2.5.3 Temperature dependence of the magneto-current ratio 28
2.5.4 Contribution of the purely ballistic electrons 29

3 Experimental procedures **33**
3.1 Deposition Setup 33
3.2 Sample fabrication 36
3.2.1 Substrate preparation 36
3.2.2 Layer structure and mask layout 39
3.2.3 Epitaxial spin valve growth 41

3.2.4 Tunnel barrier deposition . . . 43
3.2.5 Insulation pads and top contacts . . . 46
3.2.6 Comment on the shadow mask process . . . 48
3.2.7 Bonding . . . 49
3.3 Electrical measurement setup . . . 49

4 Magnetic properties **51**
4.1 Room temperature properties . . . 51
4.2 Temperature dependence . . . 55

5 Electrical properties **59**
5.1 Schottky diodes . . . 59
5.1.1 Influence of the patterning method . . . 61
5.1.2 Influence of the donor concentration . . . 64
5.1.3 Summary . . . 65
5.2 Tunnel emitter barrier . . . 65
5.2.1 Aluminum oxide:natural oxidation . . . 65
5.2.2 Aluminum oxide:plasma oxidation . . . 66
5.2.3 Magnesium oxide . . . 67
5.2.4 Applicability for MTT purposes . . . 68

6 Spin dependent transport in the magnetic tunnel transistor **71**
6.1 Requirements for collector current measurement . . . 71
6.2 Magneto-current ratio measurements . . . 72
6.3 Energy dependence . . . 74
6.4 Conclusions and outlook . . . 79

7 Summary and outlook **81**

Appendix **87**

A Simulation framework **87**
A.1 Hot electron emission . . . 87
A.2 Hot electron transport in the base . . . 89
A.3 Collection at the metal-semiconductor interface . . . 90

Bilibography **95**

List of Figures

1.1 Types of metal base hot electron transistor . . . 3
1.2 Operation principle of the MTT . . . 4

2.1 Principle of a tunnel barrier . . . 8
2.2 Electronic distribution of the injected hot electrons . . . 12
2.3 Spin valve principle . . . 13
2.4 Electron-electron relaxation processes . . . 15
2.5 Inelastic mean free path and spin asymmetry in Ni and Fe . . . 17
2.6 Effect of defect scattering on the electronic distribution . . . 18
2.7 Energy diagram of a metal-semiconductor contact . . . 19
2.8 Bandstrucure of GaAs . . . 21
2.9 Emitter voltage dependence of the collector current . . . 26
2.10 Influence of the base material on the MCR . . . 27
2.11 Influence of defect scattering on the collector current . . . 29
2.12 Temperature dependence of the MCR . . . 30
2.13 Contribution of non ballistic electrons to the collector current . . . 31

3.1 Deposition chamber . . . 34
3.2 Shadow mask system . . . 35
3.3 RHEED pattern of a GaAs (001) surface prepared by annealing and ion etching . . . 37
3.4 AFM scan of an overannealed GaAs (001) surface . . . 38
3.5 GaAs(001) surface prepared by an HCl etch . . . 39
3.6 Mask layout . . . 40
3.7 RHEED patterns of the metallic base layers . . . 42
3.8 RHEED pattern of aluminum grown on epitaxial FeCo . . . 43
3.9 Plasma oxidation setup. . . . 44
3.10 DC reactive sputtering process . . . 47
3.11 SEM picture of a MTT . . . 48

4.1 Room temperature MOKE measurement of the epitaxial spin valve . 52
4.2 In-plane GMR measured at room temperature . . . 54
4.3 Temperature dependence of the in-plane GMR . . . 55

4.4 Temperature dependence of the in plane GMR for a sample with rough interfaces 56

5.1 Room temperature I(V) characteristics of FeCo/GaAs(001) Schottky diodes grown on Ga- and As-terminated GaAs 60
5.2 Temperature dependent J(V) curves for FeCo/GaAs(001) Schottky diodes structured by in situ shadow mask and optical lithography . . 62
5.3 I(V) characteristics for different temperatures for two FeCo/GaAs diodes using two different dopant concentrations 64
5.4 I(V) curve of naturally oxidized aluminum oxide tunnel barrier 66
5.5 I(V) curve of plasma oxidized aluminum oxide tunnel barrier 67
5.6 I(V) curve of a magnesium oxide tunnel barrier 68

6.1 Electrical connections in a MTT 72
6.2 Magneto current ratio for a sample whose substrate was prepared by HCl 73
6.3 Magneto current ratio for a sample whose substrate was prepared by annealing and sputtering 74
6.4 Emitter voltage dependence of the collector current 75
6.5 Emitter voltage dependence of the MCR 76
6.6 Emitter voltage dependence of the transfer ratio 78

A.1 Flowchart of the simulation procedure in the base 91

Nomenclature

AFM	atomic force microscopy
BEEM	ballistic electron emission spectroscopy
CIP	current in plane
CPP	current perpendicular to the plane
DSM	digital sourcemeter
FM	ferromagnetic
GMR	giant magnetoresistance
IMFP	inelastic mean free path
MBE	molecular beam epitaxy
MBT	metal base transistor
MC	monte carlo
MCR	magneto current ratio
MOKE	magneto optical Kerr effect
MOM	metal-oxide-metal
MOMS	metal-oxide-metal-semiconductor
MTJ	magnetic tunnel junction
MTT	magnetic tunnel transistor
QMR	quantum mechanical reflection
RHEED	reflection high energy electron diffraction
SBH	Schottky barrier height
SC	semiconductor
SMS	semiconductor-metal-semiconductor
SSW	spontaneous spin wave
SVT	spin valve transistor
TFE	thermally assisted field emission
TMR	tunnel magnetoresistance
TSD	target substrate distance

Chapter 1

Introduction

This thesis is concerned with the study of spin polarized hot electron transport in the Magnetic Tunnel Transistor (MTT). This device is one of the many examples of so called spintronic devices where both charge and spin of the electrons are used. In most electronic devices, the motion of electrons is controlled by their charge and the electrons are essentially non spin polarized, i.e. there are as many spin up as spin down electrons. In spintronic devices on the other hand, the transport of electrons takes place in materials where the properties are different for the spin up and spin down electrons.

In the specific case of the MTT, its design is based on the integration of a spintronic two terminal component within a three terminal hot electron transistor. We will here first briefly present the concept of two terminals spintronic elements. The architecture of metal base hot electron transistor will then be described. Finally, the basic operation principle of the MTT will be discussed.

1.1 Two terminal spintronics

The first spintronic device to be fabricated and studied was a two terminal device consisting of a Fe/Cr multilayer which resistance was found to be dependent on an externally applied magnetic field[1, 2]. This effect called Giant Magneto Resistance (GMR), which discovery was awarded by a shared Nobel prize for Fert and Gruenberg in 2007, could be explained by the different resistivities of the ferromagnetic components of the multilayer for electrons whose spins were parallel or antiparallel to the layers magnetization. The industrial applicability of GMR devices was quickly recognized and the first commercial GMR read heads for computer hard drives were released less than 10 years after their discovery, in 1997 by IBM. The discovery of the GMR effect together with its tremendous commercial success led to the rapid development of a new field of research at the interface between magnetism and electronics named spin-electronics or spintronics.

In essence, GMR read heads are based on two terminal devices called spin valves, which consist in their simplest form of a non magnetic metallic spacer material sand-

wiched between two ferromagnetic electrodes. The orientation of the ferromagnetic electrodes' magnetization can be changed independently by applying an external magnetic field so that they can be either parallel or antiparallel. In the ferromagnets, due to the exchange splitting of the bands, the resistivities are different for majority and minority electrons (in this thesis, the convention will be to consider majority (minority) electrons as the electrons whose spin magnetic moments are aligned parallel (antiparallel) to the magnetization of the ferromagnet). As a result, the resistance of a spin valve will vary depending on whether the magnetizations of the ferromagnetic (FM) layers are parallel or antiparallel to each other, i.e. depending on the strength of the applied magnetic field. The antiparallel state will correspond to a high resistance state because all electrons will be strongly scattered whereas the parallel state will correspond to a low resistance state where only minority electrons will be strongly scattered. The normalized difference of those resistances is used to measure the efficiency of the spin valve elements and is usually below 5% for trilayers at room temperature. Two geometries exist depending on the direction of the current: The Current In Plane (CIP) geometry where the current is along the interface plane and the Current Perpendicular to the Plane (CPP) where the current is driven perpendicular to the interfaces.

Another major breakthrough was achieved by replacing the metallic spacer by a thin non magnetic insulator. The electrons would in this case tunnel through the insulator from one FM electrode to the other creating a Magnetic Tunnel Junction (MTJ). Assuming that the tunneling process conserves the spin, the tunneling resistance will essentially depend on the density of states in the negatively biased electrode and on the density of vacancies in the positively biased electrode, both of which are spin split. Thus, as in the case of spin valves, a variation of the resistance is observed between the case where the magnetizations are parallel and antiparallel. However, this effect relies here solely on the spin asymmetry of density of states and the different electronic mobilities have no influence (assuming the barrier is amorphous). Although the MTJ design was demonstrated at 4.2 K by Jullière in 1975[3], its reproducible realization at RT was only achieved in 1995[4]. The first MTJs used amorphous aluminum oxide with which the Tunnel Magneto Resistance (TMR= $(R_{\mathrm{P}} - R_{\mathrm{AP}})/R_{\mathrm{P}}$) reached a maximum of about 70%. More recently, TMR of more than 600% at room temperature[5] have been reached through the use of MgO barriers.

GMR and TMR elements are both two terminal spintronic component and will constitute one of the three building blocks in the MTT. The rest of the MTT architecture is directly inspired by past research that was pursued starting in the 60's on hot electron transistors.

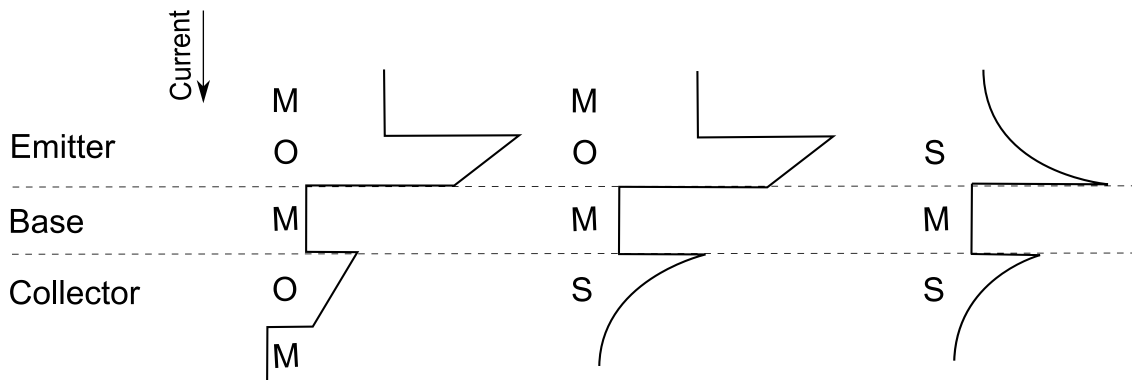

Figure 1.1: The different types of ballistic hot electron transistor with a metallic base

1.2 Hot electron devices

Historically the first hot electron solid state device was proposed by Mead [6]. His device was constituted of two MOM (metal-oxide-metal) structures in series (fig. 1.1). In the first MOM structure, the oxide is made thin enough for electrons to be able to tunnel through it. In the second on the other hand, a thick oxide is used so as to prevent any tunneling. The operation principle is as follows: electrons are injected through the first tunnel barrier (referred to as the emitter barrier) into the thin metallic base. Their energy distribution is centered around the energy eV where V is the bias voltage between the emitter and the base. In the purely ballistic picture (base thickness$\ll$inelastic mean free path), if this bias voltage is high enough, the hot electrons will have enough energy to overcome the second tunnel barrier (collector barrier) and a collector current will be detected. However, due to the very short inelastic mean free path (IMFP) in metals, the ballistic condition is practically never fulfilled and some relaxation takes place within the base. As a result, some of the hot electrons will lose some energy due to their interaction with the thermal electron bath and the lattice. In the operating range of such a transistor, if a hot electron undergoes such a scattering event, the energy loss will be most likely high enough for its energy to be reduced to below the collector barrier's height. In other words, only electrons that haven't been inelastically scattered will participate to the collector current.

This type of device was of interest for high speed operation due to the very low transit time and the small resistance of the metallic layer leading to small RC constant. The main drawback was the low gain which was mostly related to the very strong losses due to backscattering from the oxide layers. Later version of this type of ballistic transistors therefore employed a Metal-Semiconductor (MS) barrier as a collector (MOMS transistor) in order to increase the collection efficiency. Finally, thermionic emission has been used instead of tunneling injection by replacing the tunnel barrier emitter by a Schottky barrier as well (SMS transistors). The replacement of the oxide layer where a lot of electrons were scattered by SM and

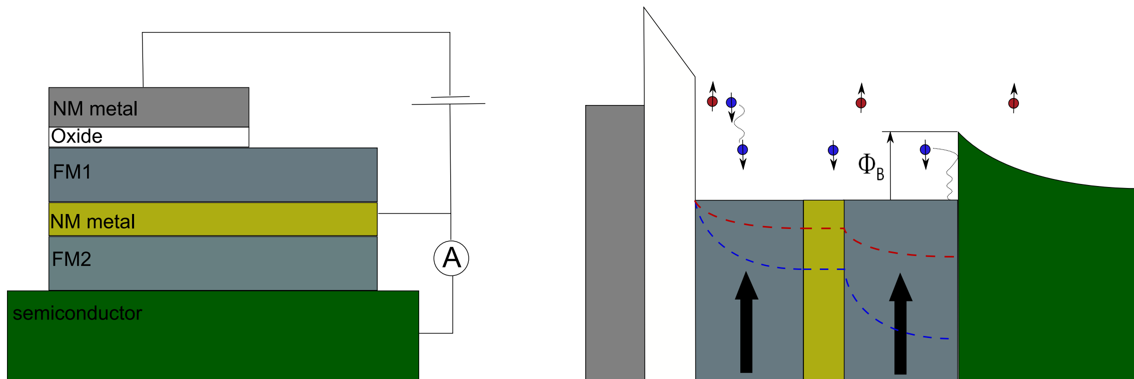

Figure 1.2: Description of a Magnetic tunnel transistor
(Left) Layer stacking
(Right) Energy diagram. The red and blue dashed lines represent the probability of not being scattered for majority and minority electrons respectively

MS interfaces led to a significant improvement of the gain which however still remained below 0.5. The SMS transistor is sometimes referred to as a Metal Base Transistor (MBT). An extension of those ideas led in the 80s to the development of the Tunneling Hot Electron Amplifier (THETA) [7] which structure is based on the same principle as a MOMOM transistor but which uses n doped GaAs instead of the metallic electrodes and AlGaAs instead of the oxide barriers. One of the main interest of those type of structure was their possible use as a spectroscopic tool. Due to the fact that the height of both the thin emitter and the thick collector AlGaAs barriers could be varied by varying the bias voltage, insight in the energy dependence of the transport properties of hot electrons in the base n-type GaAs layer could be obtained. Another development based on the architecture of the MOMS structure came to light in 1988, when Bell and Kaiser demonstrated an electron spectroscopy technique called Ballistic Electron Emission Spectroscopy (BEEM)[8]. The difference with the original MOMS transistor was that a STM tip was used to inject the electrons into the metallic base, thus yielding a lateral resolution of only a few nm. This very powerful tool has been later on used extensively to study hot electron transport in metals and get new insight in the properties of various metal semiconductor interfaces (for a review see for instance [9]). Furthermore, extensive theoretical work has been furnished in order to assess the experimental observation made by BEEM, providing a theoretical framework that applies to a large extent to the MTT as well.

1.3 Spin polarized hot electron transistor

From the above discussion, it is clear that the replacement of the metallic base in such a hot electron transistor by a GMR element should yield a magnetic field dependence of the collector current. Substantial work has been dedicated to the creation and study of spintronics hot electron transistor based either on the SMS

(Spin Valve transistor[10][11]), the MOMS (Magnetic Tunnel Transistor[12][13]) and the MOMOM architecture [14][15]. Their operation principles are similar and only the injection and collection mechanisms differ depending on the nature of the barriers used. Here, we will focus on the principle ruling the operation of MTTs. The left part of figure 1.2 depicts the layer stacking of a MTT. It is constituted of a non magnetic metal and a thin oxide layer forming the tunnel emitter, a spin valve base and a semiconductor collector. On the right part of figure 1.2 the energy diagram of a MTT is shown. As in the case of MOMS transistors, hot electrons are injected into the base and only the electrons which energies are higher than the Schottky barrier height ϕ_B will be collected. Given that the bias voltage across the tunnel emitter barrier is higher than the collector barrier height, the ratio of the injected current to the collected current will be, to a first order approximation, determined by the relative amount of electrons that relax in the metallic base due to their interaction with the electron bath and the lattice. A standard attenuation law yields the amount of ballistic electrons after traveling a distance d in the metallic base to be proportional to $\exp(-d/\lambda)$ where λ is the so called attenuation length. λ can be viewed as the characteristic length describing the efficiency of the scattering mechanisms in preventing the electrons to reach the collector. It combines the influence of all the scattering processes present in the layers and at the interfaces. The current corresponding to the hot ballistic electrons overcoming the Schottky barrier (collector current) will thus decay exponentially with the spin valve thickness. Furthermore, due to the ferromagnetic nature of the metals used in the spin valve base, the attenuation length is longer for the majority electrons than for minority electrons ($\lambda_\uparrow > \lambda_\downarrow$). As in the case of a normal CPP GMR stack, the asymmetry in the transmission will lead to a magnetic dependence of the collector current. However, the exponential attenuation will give rise to much higher effects than for a CPP GMR. Magnetic Current Ratio (MCR= $(I_{\text{col}}^{\text{P}} - I_{\text{col}}^{\text{AP}})/I_{\text{col}}^{\text{AP}}$) of up to 3400% have been observed [16]. Another attractive feature of MTTs is their potential use as spin injector. Since the transport is ballistic, the well known conductivity mismatch problem does not apply. Efficient spin injection in GaAs[17] and Si[18] have been demonstrated with this type of structure. For those reasons, the MTT structure is potentially interesting both as a magnetic field sensor and as a means to inject spin polarized current in semiconductors.

As in the case of metal base transistor, the main limitation resides in the low transfer ratio (defined as the ratio of the current collected in the semiconductor to the current emitted through the tunnel barrier). In best cases, this ratio is about $1{\cdot}10^{-4}$. The low current density it yields is for instance particularly problematic when MTTs are to be used as spin injector, since the detection of the injected spin becomes harder as the injected current density drops. Most of the studies made so far on MTT (or SVT) structures have been using polycrystalline layers. The high density of structural defects related to the different grain boundaries is however believed to be responsible for a reduction of the transfer ratio by several

orders of magnitude [19]. Experimental reports have in the meantime shown that the use of epitaxial layers in the base can yield a substantial increase of the transfer ratio[13][20]. Recently, an experimental thesis has been dedicated to the study of MTTs with epitaxial FeCo/Au/FeCo spin valve base [21]. However, it was found that the transfer ratio was at best on the order of $1{\cdot}10^{-9}$ at 11K. The low transfer ratio was in this case due rather to the poor quality of the tunnel barrier than to scattering on defects in the base. The aim of this thesis is to pursue the work made on MTT with epitaxial spin valve bases in order to reach a state where the improvement resulting from the use of epitaxial layers can be assessed. Furthermore, a new structuring method was developed based on thin film deposition through shadow masks. The use of such a method is intended to get rid of the different problems arising, mostly at the Schottky and tunnel barriers, from the patterning of MTTs by optical lithography and dry etching. Another substantial advantage of the shadow mask technique resides in the fact that the structuring is independent on the materials used, thereby allowing a reliable assessment of the relative pros and cons of different materials.

This thesis is structured as follows:

Chapter 2 is concerned with the theory of the MTT. After first describing the operation and properties of its building blocks, the influence of different external parameters on the electrical output of the MTT will be presented. This discussion will be supported by the results of numerical simulations of the spin polarized hot electron transport in the MTT. **Chapter 3** will present the experimental procedures used for the successful deposition of MTTs with epitaxial spin valve base by the shadow mask technique. In **Chapter 4** the experimental results concerning the magnetic behavior of the epitaxial spin valves defining the electrical response of the MTTs to an applied magnetic field will be shown. **Chapter 5** will be concerned with the electrical characterization of the Schottky and tunnel barriers. In the case of Schottky barriers, a special emphasis will be put on the comparison between the quality of diodes patterned in situ by shadow mask or ex situ by optical lithography. As for the tunnel barriers, the comparative merits of several barrier material will be discussed when applied to the use as an emitter barrier in a MTT. In **Chapter 6** the experimental results concerning the MTT itself will be presented and discussed. In the **Appendix**, a description of the numerical framework and physical assumptions used for the simulations presented in chapter 2 will be made.

Chapter 2

Theory of the Magnetic Tunnel Transistor

As was briefly presented in the introduction, the three building blocks of the MTT are the tunnel emitter, the spin valve base and the Schottky collector. In this chapter, the principles ruling the operation of each of these elements will be first described and will be followed by a discussion of the relevant aspects concerning their use in the MTT. A simple phenomenological model will then be presented together with its shortcomings. Finally, results of numerical simulations using a more accurate model will be used as a basis for a further discussion about the influence of several parameters such as electron energies, temperature or sample structural quality on the transport behavior in the MTT.

2.1 Tunnel barrier

The tunnel barrier is used in the MTT as an emitter barrier. As such, its properties will define the initial state of the electronic distribution and therefore influence the transport in the whole MTT structure. The basic operation principle of tunnel barriers will first be presented in (2.1.1) and a qualitative description of the electronic distribution exiting the emitter in the MTT will be made in (2.1.2)

2.1.1 Operation Principle

The quantum tunneling effect is the effect through which an electron has a non-zero probability of traversing a potential barrier higher than its energy. This pure quantum mechanical effect is rendered possible by the fact that, in the case of an incoming wavefunction on a potential barrier, although most of the intensity will be reflected, the transmitted part of the wavefunction of the electron will decay exponentially within the potential barrier. If the barrier is thin enough for the squared wavefunction to be non-zero on the other side of the barrier, there is a possibility for the electron to go or “tunnel” through the barrier (Fig. 2.1 left). The

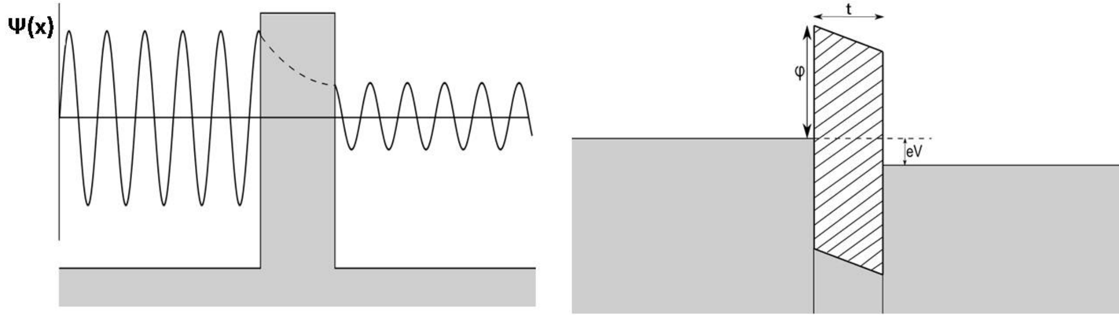

Figure 2.1: Basic principle of a tunnel barrier:
(a) Evolution of the single electron wave function through a potential barrier.
(b)Bandstructure diagram of a tunnel barrier in the case where a negative bias is applied to the left electrode

most direct way to experimentally observe this effect is by creating a metal-insulator-metal structure where the insulating layer is very thin (1-2nm). At equilibrium, the Fermi levels of the two electrodes will be equal. The tunnel current from the left electrode to the right one will be the same as the one from the right electrode to the left and the total current will be zero. By applying a bias voltage across the barrier V, the Fermi levels will shift by an energy eV (Fig. 2.1 right) creating a measurable current imbalance. In the general case, the tunnel current from the left to the right electrode will be the integral over the energy of the product of the three following factors:

- the density of states in the left electrode $\rho_{\mathrm{l}}(E)$ times the occupation probability $f(E)$ ($f(E)$ denotes the Fermi-Dirac distribution at the energy E)
- the density of states in the right electrode $\rho_{\mathrm{r}}(E+eV)$ times the probability for a state to be unoccupied in the right electrode $1-f(E+eV)$
- the transition matrix element squared$|M|^2$

or

$$I_{\mathrm{l}\to\mathrm{r}}(V)=\int_{-\infty}^{+\infty}\rho_{\mathrm{l}}(E)f(E).\left|M\right|^2.\rho_{\mathrm{r}}(E+eV)\left[1-f(E+eV)\right]dE$$

Simmons[22][23] used the WKB approximation to calculate $|M|^2$. He obtained an analytic formula for the tunnel current over a trapezoidal barrier:

$$I(V,T)=\left(\frac{e^2}{2\pi h}10^6\right)\frac{A}{d^2}\left[1+\frac{3.10^{-7}d^2T^2}{\beta}\right].\left[\beta\exp\left(-\alpha\sqrt{\beta}\right)-\gamma\exp\left(-\alpha\sqrt{\gamma}\right)\right]; \tag{2.1}$$

where

$$\alpha=\frac{4\pi\sqrt{2me}}{h}10^{-9}d;\qquad \beta=\varphi-\frac{V}{2};\qquad \gamma=\varphi+\frac{V}{2};$$

The area A is given in $[\mu m^2]$, the effective barrier height φ in $[eV]$, the barrier thickness d in $[nm]$, the voltage V in $[V]$, the current I in $[A]$ and the temperature T in $[K]$. e and m are the electron's charge and mass and h is the Planck's constant. For low voltages where $eV \ll \varphi$ the relation $I(V)$ is linear. At moderate voltages, Simmons showed that the current-voltage relation can be approximated to $I(V) \propto x_1V + x_2V^3$ which reproduces accurately most of the experimental $I(V)$ curves. In practice, the differential conductance G is often measured instead of the current. In this case, the Simmons model predict a roughly parabolic $G(V)$ relation at moderate voltages. Despite the good agreement between this theory and experimental data, it fails to reproduce a property often observed. Indeed, it assumes a perfectly symmetrical barrier and thus the $I(V)$ relation is necessarily symmetrical. However in practice, some discrepancies in the transmission of both interfaces (different electrode materials, contamination at one of the interfaces) often lead to asymmetric current voltage relations. Brinkmann [24] refined the model of Simmons to introduce an additional parameter, the barrier asymmetry $\Delta\varphi$, with which he could indeed predict that the difference in interface transmission induces asymmetric $I(V)$ curves. Both models are readily used to fit experimental data in order to extract the effective barrier thicknesses and height. The good quality of such a fit is often taken as a proof for tunneling being the sole transport mechanism involved. This fact finds its origin in the definition by Rowell of a set of criteria that could be independently used to identify electron tunneling in superconductor - insulator - superconductor junctions [25]. In the case where the electrodes materials are not superconducting, three criteria remain:

1. The current increases exponentially with decreasing thicknesses
2. The $G(V)$ relation follows a parabola at moderate voltages
3. A weak insulator-like variation of the conductance with temperature

We can immediately see that out of the three criteria, the second one is the easiest to check experimentally. However, upon close examination of those criteria, it turns out that not all of them are reliable. Akerman [26] used a superconductor - insulator-ferromagnet structure to assess their relevance when taken as a proof for tunneling. The first and second criteria could be satisfied as well when small contact points called pinholes existed between the two electrodes. In this case, part of the current flows through those pinholes in an ohmic manner. The temperature dependence of the resistance, related to the third criterion, however proved to differ depending on the presence or absence of pinholes. Only when the barrier was completely closed could the insulating-like behavior of the temperature variation of the conductance be recovered. Furthermore, Akerman found that the noise and instability of the junctions were strongly increased if pinholes were present.

In experimental barriers, the insulating layer is usually less than 2nm thick. Within this range of thicknesses, some spatial variation of the thickness or the

oxide's stoichiometry cannot be excluded. The first Rowell criterion indicates that the current increases exponentially with decreasing thickness. This means that in practice, the current flow through a tunnel barrier will vary from site to site. A way to look into this point was found by measuring the local current through an uncapped naturally oxidized cobalt layer with the help of a conducting AFM in contact mode [27]. The authors found that the current density can vary by several orders of magnitude within one sample (the indicated rms roughness was 0.5nm) and concluded that the transport of electrons takes place primarily only at a few sites where the transmission is increased due to a local reduction of barrier thickness or height. In light of those results, the relevance of the Simmons-like models is questionable as it relies on a planar theory, excluding *de facto* any lateral spatial variation of the thickness and barrier height. One can however extend this planar model to take into account interfacial roughness by using a given distribution of barrier thicknesses [28] (for instance a Gaussian distribution of standard deviation σ) and integrating the current density equation over this distribution. As it turns out, the inclusion of roughness changes the shape of the $G(V)$ curve such that it reduces the accuracy of the barrier height and thicknesses as extracted from a fit by the planar Simmons model: for applied biases less than the barrier height, the net conductance resembles that of a barrier whose effective thickness is nearly two-and-a-half σ below the mean thickness.

One of the most critical aspects for the use of a tunnel emitter in MTTs is the magnitude of the breakdown voltage. There have been many reports over the last 15 years of the breakdown voltage for thin tunnel barriers and a large scatter exists among the published data. These strong variations are related to the dependence of the breakdown voltage on the barrier chemical and structural quality as well as the structuring methods used (masks are usually known to reduce the breakdown voltage due to an enhancement of the electric field at the non sharp edges [29]). A distinction is usually made between intrinsic and extrinsic breakdown[30]. In the former, the breakdown occurs due to voltage stress-induced degradation of the insulator and appears as a non reversible jump in the I(V) curves. The latter is related to pinholes in the insulator. Extrinsic breakdown's signature is a slow reduction of the tunneling resistance scaling with the voltage$\times$time product. This slow reduction correspond to an increase of the pinhole size.

2.1.2 Tunnel emitter

The properties of the electrons injected from the metal emitter through the tunnel barrier, inside the metallic base is of foremost importance to the understanding of the basic properties of the magnetic tunnel transistor as it defines the initial state for the electronic transport in this device. The Schottky collection barrier acts as a high pass energy filter with a cut off energy slightly below the Schottky barrier height (some tunneling cannot be excluded). This means that the width of

the energy distribution of the injected electrons will have a direct influence on the current gain of the transistor. Furthermore, as will be explained more thoroughly in section (2.3.4), an electron can be collected in the semiconductor only if there are empty states that match its energy **and** its parallel component of the wavevector. An understanding of the wavevector distribution of the injected electrons is thus equally relevant as of the energy distribution. In order to have a qualitative estimation of the shape of the electronic distribution exiting the tunnel barrier, we use a simple model based on the Monte Carlo (MC) algorithm. The program used is described at length in the Appendix A.1 and only the main aspects concerning the transport across the tunnel barrier will be shortly summarized here. Electronic states are randomly selected within the relevant phase space of the metal emitter through a rejection algorithm. The contribution of a state to the tunneling current is then given by the product of 4 terms:

1. The occupation probability in the metal emitter $P_{occ}(E)$
2. the probability for a state to be unoccupied in the base $P_{vac}(E)$
3. the incident charge flux on the tunnel barrier which is proportional to the projection of the electronic velocity perpendicular to the interface $\hbar k_{\perp}/m$
4. the tunneling probability $P_{WKB}(E_{\perp})$

The tunnel current density is then given by:

$$J_{base} = eN\frac{\hbar}{m}\sum k_{\perp}P_{occ}(E)P_{vac}(E)P_{WKB}(E_{\perp})$$

where e is the electronic charge and N is a prefactor that corresponds to the sampling density. The sum is over the sampled states. The transmission probability, defined as the product of the three probabilities listed above, is shown in figure 2.2 top left panel for different bias voltages. We can see that, as V is increased the transmission probability increases. Furthermore the energy distribution of the injected electrons in the base is always peaked around V. If we plot the transmission probability versus the wavevector components in the emitter parallel and perpendicular to the interface (fig 2.2 top right panel) we see that the electrons are strongly forward focused with a distribution centered around zero for $k_{\parallel}$ and around the Fermi wavevector k_F for $k_{\perp}$. The width of both distributions depends primarily, at a given temperature on the barrier thickness t, through the exponential dependence of the WKB factor on t. As t decreases, the transmission probability increases exponentially yielding thus a wider wavevector distribution (Fig. 2.2 bottom panels).

2.2 Transport in the metallic base

The base of the MTT is constituted by a spin valve trilayer and is responsible for the magnetic dependence of the collector current. The basic principle of a spin valve

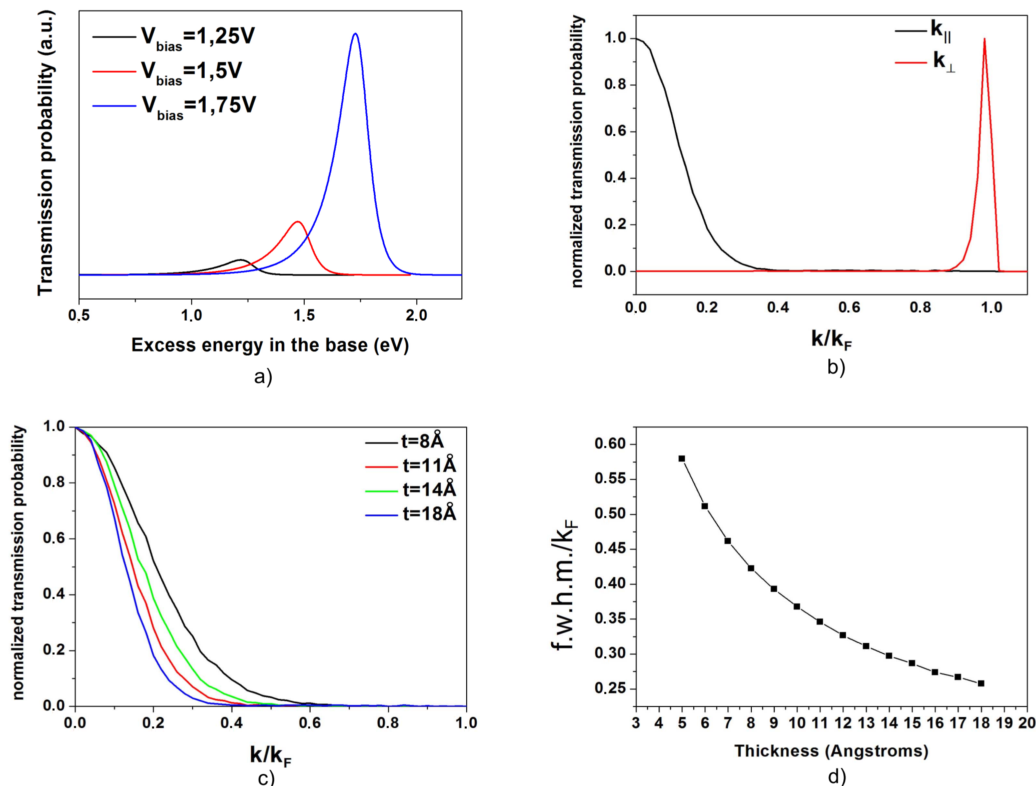

Figure 2.2: Simulation results using the model described in appendix A:
(a)Transmission probability versus excess energy in the base for different bias voltages.
(b)Normalized transmission probability versus the parallel and perpendicular component of the wave vector in the emitter metal.
(c) Normalized transmission probability versus the parallel component of the wave vector in the emitter metal for different barrier thicknesses.
(d) Evolution with the barrier thickness of the full width at half maximum of the transmission probability as plotted in (c)

together with its layer stacking will described in (2.2.1). Then the fundamental mechanisms ruling hot electron transport in the MTT base will be addressed in (2.2.2)

2.2.1 Spin valve

A spin valve is a spintronic element based on the effect called giant magneto resistance (GMR). It is constituted, in its simplest form of three layers: two ferromagnetic materials separated by a non magnetic metallic spacer. Upon applying a voltage across the element (fig 2.3), the measured current will depend on the relative orientation of the magnetizations due to the GMR effect.

The transport in each layer can be described according to the semi classical theory of Drude for Fermi transport by the relation between the resistivity ρ and the

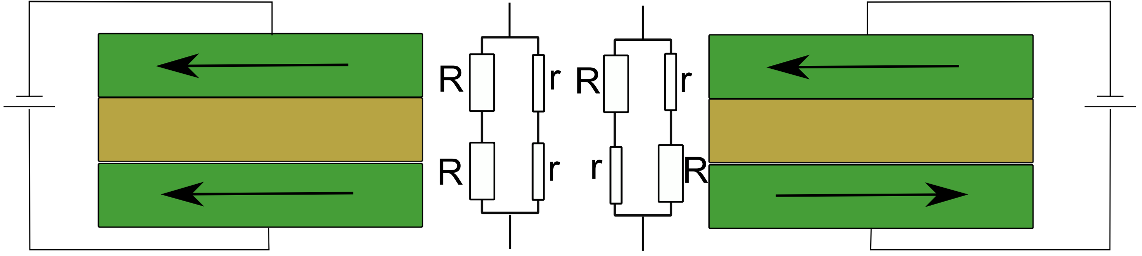

Figure 2.3: Schematic layer structure of a spin valve in a parallel (left) and antiparallel (right) state with the associated equivalent resistor circuit diagramm

scattering time τ, $\rho = m/(ne^2\tau)$, in which m and e are the electron mass and charge and n is the density of electrons contributing to the transport. In ferromagnets, the density of states is exchange split. The available phase space to scatter into will therefore be different for spin up and spin down. This implies that the scattering times for the majority and the minority electrons will be different. Accordingly there will also be a discrepancy between the related resistivities, ρ_{maj} and ρ_{min}. In the limit of zero spin mixing, the transport of electrons through each FM layer can be approximated as being constituted by the parallel transport of the two spin channels. We define a low resistance r (resistance of a single ferromagnetic layer for the majority electrons) and a high resistance R (resistance of a single ferromagnetic layer for the minority electrons). The resistor diagram equivalent to the spin valve immediately gives the resistances in the parallel and antiparallel cases, R_P and R_{AP}:

$$R_P = \frac{2rR}{r+R} \quad \text{and} \quad R_{AP} = \frac{r+R}{2}$$

The GMR is then defined as

$$GMR = \frac{R_{AP} - R_P}{R_P}$$

The value of the GMR for trilayer is typically of a few % and tends to decrease with increasing temperature due primarily to the increased electron-magnon scattering.

In practice, several types of CPP (Current Perpendicular to the Plane) spin valves have been developed. The main difference lies in the type of method used to obtain a state where the magnetizations of the ferromagnetic layers are antiparallel. In a first type, the ferromagnetic layers can be coupled antiferromagnetically through interlayer exchange coupling. Another possibility is to pin one of the layer to a thick antiferromagnet through exchange bias while the other layer remains free. Finally, one can choose a system where the coercive fields of the ferromagnetic layer are different. Such a spin valve is called a pseudo spin-valve. When the spin valves are to be used within a MTT, not all those methods are applicable. The interlayer exchange coupled spin-valves are usually restricted to a given range of thicknesses that might conflict with the requirements for signal optimization of a MTT. The

use of a pinned spin valve would drastically reduce the output current due to the presence of the thick antiferromagnet as the pinning layer. In contrast, a pseudo spin-valve can operate in a wide range of thicknesses without the addition of any extra layer, making it a suitable choice. However, the mechanisms influencing the magnitude of the coercive fields have to be carefully identified in order to ensure a maximum operational range.

2.2.2 Hot electron scattering in the spin valve base

In a GMR element, the electrons carrying the current all have energies close to the Fermi level. One of the condition for a scattering event to take place, is that the electron finds an unoccupied state to scatter into. The maximum energy loss due to scattering event is thus given by the thermal broadening of the Fermi-Dirac distribution, namely $3kT \cong 0.08eV$ at $T = 300K$. Thus only elastic or quasi elastic scattering can occur. In contrast to this, the energetic range of operation for a MTT lies between the Schottky barrier height $\Phi_B \cong 0.7eV$ and the tunnel barrier height $\varphi \cong 1.8eV$ (for aluminum oxide). The density of unoccupied state in the spin valve metals is in this case very high and electrons will undergo both elastic and inelastic scattering. Magnetic excitations, which are expected to induce a spin asymmetry in the scattering of hot electrons in ferromagnets, are classified into electron-hole excitations (Stoner excitations) and collective excitations (Spin waves). In the rest of this section, we will first summarize the relevant aspects of both scattering types for the transport of a MTT and then comment on elastic defect scattering which as will be shown in (2.5.2) accounts for the biggest reduction of the output current in MTTs.

Electron-electron inelastic scattering

The electron-electron scattering finds its origin in the Coulomb interaction. Through its effect, an electron with an energy higher than the Fermi energy can interact with a thermal electron and "share" with it part of its energy thus exciting an electron-hole pair. Electron-electron scattering can be classified into three different types. Figure 2.4 describes the possible processes through which an electron-hole pair can be excited via Coulomb interaction with a majority hot electron. The symmetrical processes are of course valid for an interaction with a minority spin electron. In the process (a), an incoming majority electron relaxes into a majority hole and excites a minority electron leaving a minority hole behind. The process (b) is similar to (a) except for the fact that the majority hot electron excites a majority electron-hole pair. In the process (c), the hot electron loses an energy E_i and excites an electron hole pair. In this case both majority and minority electron hole pair can be excited. It is to be noted that in all cases the spin of each individual electron is conserved. The processes (a) and (b) are called exchange processes and (c) is called direct process. A Stoner excitation is defined as an electron-hole pair with opposite

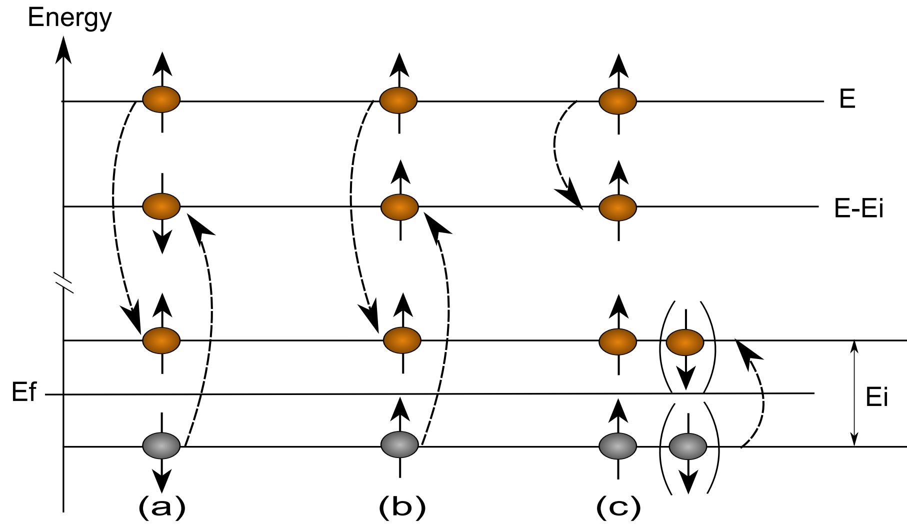

Figure 2.4: Possible processes for electron-electron interaction

spin (process (a)). The process (a) is referred to as a spin flip process whereas (b) and (c) are called non spin flip processes. In terms of scattering probability, the spin flip and non spin flip processes are comparable [31][32]. The non spin flip processes show almost no spin asymmetry. On the other hand, the spin flip process (Stoner excitations) shows a strong asymmetry between the two spin channels. The case where a minority electron relaxes into a minority state and excites a majority electron above the Fermi level is more likely to happen than the symmetrical case. This is because there are more minority states than majority states above the Fermi level and more majority electrons below. This configuration favors the creation of a minority electron-majority hole pair. The minority hot electrons will therefore thermalize faster than the majority. The asymmetry of the spin flip process will depend on the detailed bandstructure of the ferromagnet[33, 31]. In the energetic range of a MTT, the energy loss due to electron-electron scattering is usually so high that the electrons undergoing such a scattering event won't retain enough energy to overcome the Schottky barrier and thus won't participate to the collector current. As a result, electron-electron scattering will reduce the current in the minority channel more strongly than the majority channel and it is considered as the main source of spin asymmetry in MTTs.

Spin wave scattering

Spin waves are collective excitations of a spin system which can be considered as a quantum of spin reversal. In a ferromagnet, the energy cost for one electron to flip its spin is high, due to the strong exchange interaction with the neighboring electrons. It is energetically more favorable for the spin system to be in a configuration where each spin makes a slight angle with its neighbors in such a way that the overall magnetization is reduced by two Bohr magneton. In this case the transverse component of the spins will vary spatially as a plane wave and the relation describ-

ing the relative angle between two neighboring spins will be the same as the one describing the spatial variations of a plane wave of wave vector $\vec{q}$. Accordingly, the spin wave energy (i.e. the energy cost induced by the reduction of the magnetization by two μ_B) will follow a dispersion relation $E = Dq^2$ where D, the spin stiffness is related to the exchange coupling constant J. This means that the energy cost of a spin wave can be extremely low when $\vec{q} \approx 0$ (for an isotropic system).

The above description is valid only when q is small. Indeed, depending on the wavevector magnitude, different spin wave regimes exist related to different magnetic interaction. The exchange interaction, responsible for the existence of ferromagnetism, is very strong but has a range of action of typically a few angstroms and will thus be important for large wavevectors spin waves. On the other hand, the dipolar interaction has a much lower strength but is mediated over long distances and will become the relevant interaction for small wavevectors. Small wavevectors spin waves can be described through a macroscopic continuum model that neglects the details of the microscopic system under consideration. For exchange dominated spin waves whose wavevectors can be of the same order of magnitude as the reciprocal interatomic distance, a true microscopic description is required and one usually uses a quasi particle approach. As a rule of thumb, one can consider that spin waves with wavevector $q < 10^{-3}\text{Å}^{-1}$ belong to the dipolar regime and those with $q > 10^{-3}\text{Å}^{-1}$ to the exchange regime [34].

Due to the fact that a spin wave has a spin momentum, scattering of electrons on spin waves will always induce a spin flip. The conservation of angular momentum further implies that majority electrons can only absorb a spin wave while minority electrons can only emit one. It has been shown both theoretically[32] and experimentally[35] that spin waves contribute effectively to the spin dependence of the inelastic mean free path (IMFP) in ferromagnets. The asymmetry is created by spontaneous spin wave emission (SSW) which is possible only for minority electrons. SSW is independent on the temperature and is present even a T=0K. Furthermore, SSW has been calculated to dominate the low energy part (below 1eV) of the excitation spectrum in itinerant ferromagnets[35].

Apart from SSW emission, there exits as well a thermal component that allows both spin wave absorption and emission. The maximum energy of those thermally excited spin waves is determined by the extent of the thermal broadening of the Bose Einstein statistics. At a temperature of 300K, the maximum possible thermal spin wave energy will be roughly $E_{max} \cong 60meV$. This means that, within the range of interest for the energy involved in the transport processes of a MTT, the scattering with thermal spin waves will be almost exclusively quasi elastic. Furthermore, the rate at which majority electrons absorb thermal spin waves is the same as the rate at which minority electrons emit spin waves $\tau_{SW\uparrow} = \tau_{SW\downarrow}$[36]. Thus, scattering on thermal spin waves contrary to SSW emission will not directly induce a spin asymmetry in the overall electronic scattering in a MTT.

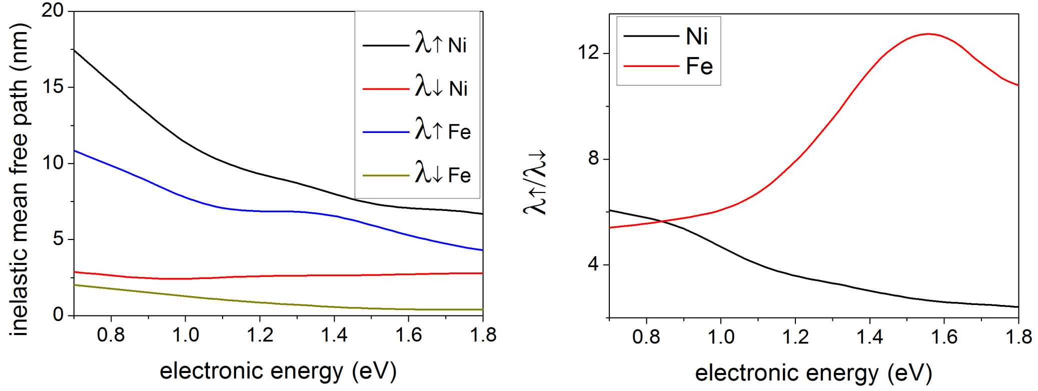

Figure 2.5: inelastic mean free path and spin asymmetry in Ni and Fe from [37]

Inelastic mean free path

The contributions of the inelastic processes mentioned above are usually taken into account through the inelastic mean free path (IMFP). In a recent theoretical study, Zhukov and coworkers calculated the IMFP for Fe and Ni [37, 38]. Very good quantitative agreement is found between their calculated IMFPs and experimental values extracted from [12]. The values of the IMFP they obtained are plotted in figure 2.5. Both in the case of Ni and Fe we can see that the IMFP for the majority electrons decreases with increasing energies as a result of the increase of the phase space for the hot electrons to scatter into. Furthermore, it can be seen that the majority IMFP of Fe changes its curvature at energies close to 1.4eV. The minority IMFP are found to be in comparison almost constant. However, some small variations can still be observed, especially for Fe where a slight increase of $\lambda_\downarrow$ can be observed from an energy of 0.9 eV on. A direct consequence of the slight differences in the variations of the IMFP can be seen in the right panel of figure 2.5 where the ratio $\lambda_\uparrow/\lambda_\downarrow$ is plotted. Whereas for Ni $\lambda_\uparrow/\lambda_\downarrow$ constantly decreases, a maximum is observed in the case of Fe. This is of practical importance in the case of MTTs as the magnitude of the electrical response to an applied magnetic field will depend on the spin asymmetry of the material. In the general case, the IMFP can be described, for a given energy as the product of the inelastic lifetime with the group velocity. Zhukov and coworkers calculated the contribution of each factor to the IMFP. It was found that the origin of the spin asymmetry of the IMFP is different in the two ferromagnets. In Ni, the spin asymmetry stems from the difference in the lifetime whereas in Fe it stems form the differences in the group velocity. In the meantime, this assertion has been confirmed for Fe[39].

Scattering on defects in the bulk and at the interfaces

Depending on the degree of crystallinity and the quality of the interfaces, defects can exist in a MTT under different forms (point imperfections, vacancies, stacking

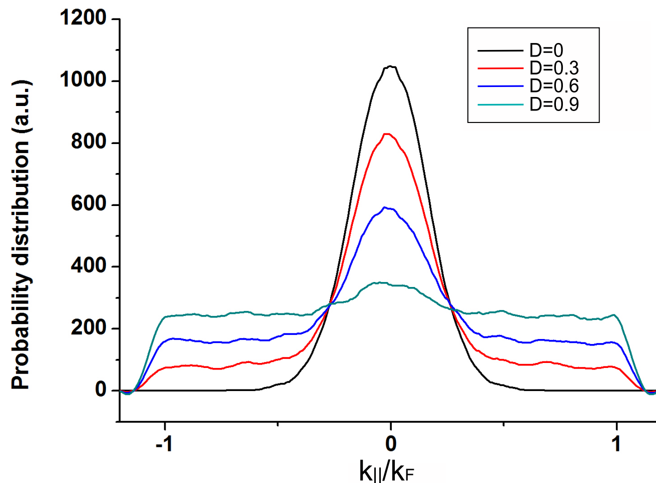

Figure 2.6: The effect of elastic defect scattering on the parallel component of the wavevector of the electronic distribution in a MTT. The parameter D corresponds to the probability for electrons to be scattered at the interfaces.

faults, dislocations...). Those defects will affect the electronic transport by creating scattering centers where the ionic potential is different than in the rest of the layer considered. The mass of those defects is usually orders of magnitude higher than the electronic mass and defect scattering can thus be considered as a purely elastic mechanism. Furthermore, it has been shown that defect scattering is a process mostly independent on the spin orientation [11] [19]. The effect on the electronic distribution will be to redistribute the electrons over the phase space in a spin independent manner. In most theoretical treatments of transport in a MTT, SVT or BEEM, defect scattering is assumed to be isotropic[40][19]. Under such an assumption, we can use the simulation scheme described in appendix A to calculate the influence of defect on the transport properties in a MTT. Figure 2.6 depicts the $k_{\|}$-resolved distribution of electrons in a MTT after traveling through the spin valve and right before collection for different values of the defect scattering parameter D. The scattering factor D, corresponds to the probability of an electron to be scattered by a defect at an interface (same probability for all the interfaces). We can see that for $D = 0$, the electronic distribution is a gaussian centered at $k_{\|} = 0$. As D is increased, the electron distribution flattens and states with higher $k_{\|}$ become occupied. Eventually, the electron distribution becomes so spread that an almost fully isotropic distribution is obtained. Although defect scattering is considered here only at the interfaces, a similar behavior would occur when bulk scattering is present. As will be seen in the section (2.5.2), defect scattering is one of the main process involved in the reduction of the overall transmission in a MTT.

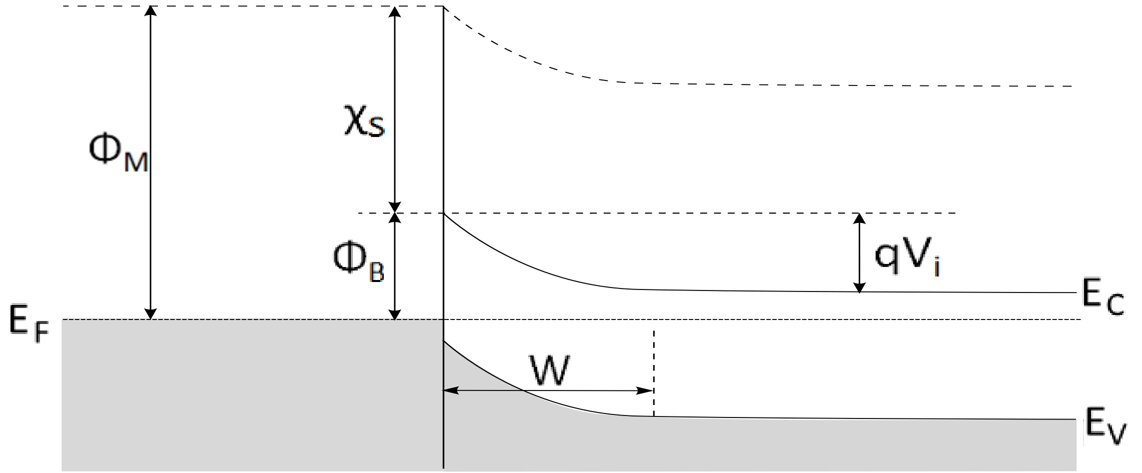

Figure 2.7: Energy diagram of a metal-semiconductor contact at thermal equilibrium

2.3 Schottky diodes

2.3.1 Principle

When a metal is brought in contact with a semiconductor (SC), a potential barrier is formed arising from the separation of charges at the metal-SC interfaces. The height of this barrier Φ_B is given by the relation

$$\Phi_{\mathrm{B}} = \Phi_{\mathrm{M}} - \chi_{\mathrm{S}},$$

where Φ_{M} is the work function in the metal and χ_{S} is the electronic affinity in the SC. This results in a high resistance region in the SC depleted from mobile carriers. As depicted in figure 2.7 for a n-type SC and in the case where Φ_M is higher than χ_{S}, upon contacting of the two surfaces, electrons from the conduction band of the SC will flow into the metal until an equilibrium is reached where both Fermi levels are equal. There is a positive charge on the SC side of the interface created by ionized donors and the electrons which cross over into the metal form a thin sheet of negative charge. The density of donors being orders of magnitude smaller in the SC than the electron concentration in the metal, the voltage drop V_{i} is concentrated in the SC. The spatial extent W of the region at the SC interface where the electrons are depleted, the so called depletion layer, can be calculated through the relation

$$W = \sqrt{\frac{2\epsilon_{\mathrm{s}}\epsilon_0 V_{\mathrm{i}}}{eN_{\mathrm{D}}}},$$

where N_{D} is the donor concentration. By varying N_{D}, one can therefore vary the width of the depletion layer. Depending W, several competing transport processes have to be considered:

1. *Thermionic emission*, where the electrons are excited to an energy level higher

than Φ_B.

2. *Field emission* corresponds to tunneling through the barrier.

3. *Thermionic Field emission* which is a temperature assisted field emission process.

In the case of a MTT, thermionic emission is desired as the Schottky barrier is meant to cut off the part of the electron distribution whose energy is smaller than Φ_B. Processes 2. and 3. are relevant for high doping where the barrier width becomes small. Typically for GaAs, this corresponds to doping levels above 5.10^{17} donors/cm^{-3}.

2.3.2 Forward bias characteristics

When a positive voltage V is applied on the metallic side while the SC remains grounded, the Schottky barrier is said to be forward biased. In this case, the Fermi level in the SC becomes higher than in the metal ($E_{FS} = E_{FM} + qV$) and the band-bending is reduced to $q(V_i - V)$. The electrons in the SC now see a reduced barrier and the current density from the SC to the metal $J_{S\to M}$ is increased as compared to its equilibrium value. By applying thermionic emission theory in which the current is integrated over all electrons that have enough kinetic energy perpendicular to the interface to overcome the barrier (process (1)), one finds:

$$J_{S\to M}(V) = \left(\frac{4\pi m^* k^2}{h^3}\right) T^2 \exp\left[-\frac{q\Phi_B}{kT}\right] \exp\left[\frac{qV}{kT}\right]$$

The current density $J_{S\to M}$ in the other direction is independent of the applied voltage (without taking into account the image force) and is then simply $J_{S\to M}(V = 0)$. The total current density is thus:

$$J = J_{S\to M} - J_{M\to S} = AT^2 \exp\left[-\frac{q\Phi_B}{kT}\right] \left(\exp\left[\frac{qV}{kT}\right] - 1\right).$$

A is the Richardson constant

$$A = \left(\frac{4\pi m^* k^2}{h^3}\right).$$

In practice, electrons being scattered in the SC before reaching the maximum of the barrier and quantum mechanical reflexion lead to an effective Richardson constant A^* which is dependent on the SC. In data analysis of experimental I(V) curves an ideality factor n is used to account for the departure from the pure thermionic emission process. n equals to 1 in the ideal case and increases as the transport processes deviates from the thermionic emission case. Finally the current density in

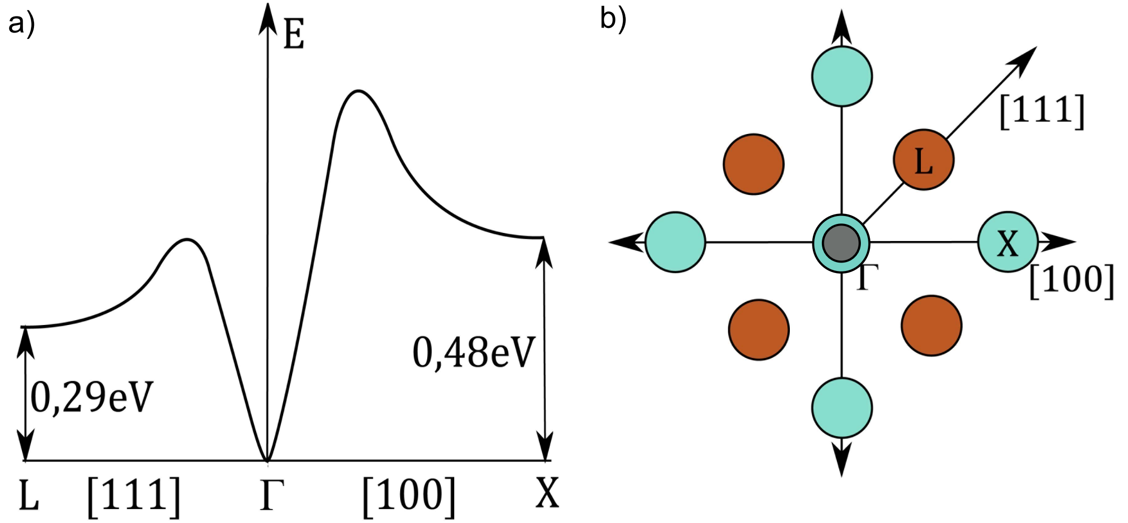

Figure 2.8: (a) Bandstructure of the conduction band in GaAs
(b) Interface Brillouin zone of the GaAs (001) surface. The labeled axis show the projection of the [100] and [111] axis on this surface

the forward direction is given by:

$$J = A^{*}T^{2} \exp\left[-\frac{q\Phi_{\mathrm{B}}}{kT}\right]\left(\exp\left[\frac{qV}{nkT}\right] - 1\right) \tag{2.2}$$

For GaAs, $A^{*} = 4.4\mathrm{Acm}^{-2}\mathrm{K}^{-2}$[41].

2.3.3 Reverse bias characteristics

According to thermionic emission theory, the reverse current density should saturate at a value of

$$J_{\mathrm{R}} = \left(\frac{4\pi m^{*}k^{2}}{h^{3}}\right) T^{2} \exp\left[-\frac{q\Phi_{\mathrm{B}}}{kT}\right]$$

However, in practice, no saturation is observed. A possible explanation for this is a variation of the barrier height with the applied voltage. Image force, interfacial oxide layer or intermixing/defects all induce a voltage dependency of the barrier height. The non saturation of the reverse current can stem as well from tunneling through the barrier. In reverse bias, the potential barrier can become thin enough near the top for the electrons to be able to tunnel through the barrier before reaching the barrier's maximum. Around room temperature, thermally assisted field emission becomes relevant for GaAs for doping $N_{\mathrm{D}} > 2.10^{16}\mathrm{cm}^{-3}$ in the reverse direction[42]

2.3.4 Schottky collector

The regime of interest in the case of a MTT is a special case as compared to the previous description of the transport properties of Schottky barriers. Here, the

barrier is completely unbiased and hot electrons simply impinge on it due to the velocity they gained when first emitted. In their original theory of BEEM[8], Bell and Kaiser used a simple model to describe the collection conditions of hot electrons at the Schottky interface. This model can be applied indifferently to a BEEM transport measurement or to a MTT since the spin polarization of the hot electrons has no influence on the collection mechanisms. Electrons were to be collected if:

- the energy is conserved
- the parallel component of the wavevector is conserved

Those conservation rules directly imply that part of the electron beam will be reflected at the SC interface as there will be no available states in the SC satisfying them. More generally, the magnitude of the collector current and its energy and momentum distributions will depend on the detailed band structure of the SC. When GaAs is used as a collector, 3 transport channels are taken into account corresponding to the 3 valleys Γ, X and L (Fig.2.8).

Assuming isotropic spherical valleys, for a given kinetic energy E_{k} such that $E_k - \Phi_{\mathrm{i}} > 0$, where Φ_{i} is the Schottky barrier height for the considered valley, Γ, X or L, the constant energy surfaces are spherical with a radius r_{i}.

$$r_{\mathrm{i}} = \frac{\sqrt{2m_{\mathrm{i}}^{*}\left[E_{\mathrm{k}} - (E_{\mathrm{F}} - E_{\mathrm{C}}) - q\Phi_{\mathrm{i}}\right]}}{\hbar}$$

Collection will take place if the parallel component of the wavevector is inscribed within a cone of projection of the constant energy spheres onto the interface Brillouin zone. In other words, the conditions on energy and parallel momentum conservation define a maximum angle, or acceptance cone for each valley within which the electrons' wavevectors will have to lie for them to be collected. In order to fit the emitter bias dependence of the collector current in BEEM experiments, six fitting parameters are commonly used: one threshold energy (or Schottky barrier height) and one magnitude factor for each valley[43]. The magnitude factor corresponds to the relative amount of electrons transiting through the different valleys. In the purely ballistic picture and assuming quadratic dispersion relation in the base and in the emitter, the wavevector distribution of the electrons emitted in the base is strongly forward focused. As a result, most of the collected current should transit through the Γ and the central X valleys. One would therefore expect the magnitude factors for the L and the outcentered X valleys to be small. However the values required to fit experimental BEEM curves yield much higher magnitude factors for the outcentered L and X valleys than the expected ones[44]. In order to address this fact, the $k_{||}$ distribution can be probed by changing the semiconducting substrate orientation, while keeping the tunneling and propagation condition through the metallic layer fixed. Schowalter and Lee [45] investigated this point by measuring the BEEM current in Au films grown on Si(100) and Si(111). Although the (100) directions has

available states around the Γ point and the (111) has none, the measured collector current was found to be quite insensitive on the crystallographic orientation of the substrate. This contradicts the pure ballistic description of BEEM transport as it implies that the $k_{||}$ distribution is somewhat homogeneously spread over the IBZ. In an attempt to improve the Bell-Kaiser theory, Smith *et al.* have incorporated elastic scattering at the metal semiconductor interfaces[46]. The method was to first assume that E and $k_{||}$ are good quantum numbers and calculate the eigenstates of the Hamiltonian describing the transport over an ideal interface. A perturbation is then added that effectively redistributes the electrons over the eigenstates. The transport through the metal is assumed to be purely ballistic. The strength of this perturbation (directly related here to the density of structural defects at the interface) is then fitted to experimental data. The authors found that this interface elastic scattering probability has to be extremely large (close to 1) in order to even out the collector currents on Si(111) and Si(100). Although this approach clearly demonstrates the importance of elastic defect scattering as a randomizing mechanism for the parallel wavevector distribution, the localization of all elastic scattering centers at the interface remains questionable.

Assuming all the conditions mentioned above are fulfilled (i.e. there is a state in the SC that matches the energy and wavevector of the impinging electron and no defect scattering at the interface hinders its collection), there is still a chance that the electrons are reflected back at the interface. This is due to a quantum mechanical effect called quantum mechanical reflection (QMR), related to the fact the wave function has to be amplitude and phase matched on both sides of the barrier. Crowell and Sze have calculated the effect of QMR in hot electron SMS transistor [47]. They found that the transmission increases with the excess energy but remains substantial over the operating regime of a MTT. Although those calculations used a Schottky injector instead of a tunnel barrier, one can expect, due to the similar emitted electron distributions, that the order of magnitude of the quantum mechanical reflection stays the same in the case of a MTT. Those calculations included only QMR as a possible backscattering mechanism at the MS interface. However, due to the image force, the potential maximum lies inside the SC, a few Å away from the interface. The electrons can therefore be scattered by phonons in the SC before reaching this maximum and lose enough energy to fall below the transmission threshold. Similarly, this scattering mechanism can preclude collection by scattering the electrons out of the acceptance cone. An estimation of the magnitude of quantum mechanical reflection and phonon backscattering at a Schottky barrier in BEEM can be found in the study of Lee and Schowalter [48] at temperatures of 300K and 77K. The combined effect of the two backscattering mechanisms was shown to yield a transmission probability of only a few percent at room temperature. At both temperatures the combined action of QMR and phonon scattering led to a roughly energy independent transmission.

2.4 Transport properties in a MTT:a phenomenological model

As has been seen in the previous sections, the transport in the MTT is rather complex as it combines the influence of each of its building blocks. On an experimental level, the only possibility to assess the magnitude of the transmission through a MTT is through the measure of the collector current. For the quantification of experimental data and the extraction of effective attenuation length, a simple phenomenological model is often used to fit the data. As in the two current model, mixing of the two spin channels is excluded. In the case of a MTT with two ferromagnetic layers, the collector currents in the parallel (P) and antiparallel (AP) states can be expressed as being proportional to:

$$I_C^{\mathrm{P}} \propto T_{\mathrm{maj}}^{\mathrm{FM_1}} T_{\mathrm{maj}}^{\mathrm{FM_2}} + T_{\mathrm{min}}^{\mathrm{FM_1}} T_{\mathrm{min}}^{\mathrm{FM_2}},$$

$$I_C^{\mathrm{AP}} \propto T_{\mathrm{maj}}^{\mathrm{FM_1}} T_{\mathrm{min}}^{\mathrm{FM_2}} + T_{\mathrm{min}}^{\mathrm{FM_1}} T_{\mathrm{maj}}^{\mathrm{FM_2}}.$$

As for metal base transistors[49], an exponential attenuation is assumed to express the transmission through a single layer such that

$$T_{\mathrm{maj(min)}}^{\mathrm{FM_i}} = \alpha_{\mathrm{i}} \exp\left(-\frac{t}{\lambda_{\mathrm{maj(min)}}^{\mathrm{FM_i}}}\right),$$

where α_{i} corresponds to the interface transmissivity. α_{i} typically accounts for the different interface elastic scatterings such as defect scattering or reflections due to bandstructure mismatch. $\lambda_{\mathrm{maj(min)}}^{\mathrm{FM_i}}$ is the hot majority (minority) electrons attenuation length and its inverse is defined by Matthiesen's rule as the sum of the inverse of the attenuation length characteristic of each scattering mechanism in the layers (elastic scattering, Stoner excitations, SSW emission and thermal spin waves). Starting from this model, several refinements can be added in the form of prefactors describing the injection efficiency of the tunnel barrier or the collection efficiency at the Schottky interface. Although this simple model can qualitatively describe some of the characteristic features of the MTT, it overlooks several key elements involved in the transport process of these devices. For instance, the emitter bias dependence or the temperature dependence of the MCR or the influence of the wavevector spread of the injected hot electrons on the magnitude of the collector current cannot be taken into account directly by this model and those effects have to be included in the effective attenuation length. The drawback of this approach is that the attenuation length obtained from the fit of experimental data by this model are highly dependent on the experimental conditions as they include the influences of many and sometimes competing physical processes.

2.5 Transport properties of the magnetic tunnel transistor

In this section the results of numerical simulations conducted within the framework of this thesis will be presented in order to shed some light on the interplay between the physical mechanisms underlying the electrical response of a MTT to an externally applied magnetic field. The complete simulation scheme is described in Appendix and only the results will be presented in this section: The bias dependence of the Magneto Current Ratio (MCR) and its relation to the material properties of the ferromagnetic electrodes will first be examined. Then the influence of structural defects will be studied. We will then discuss the influence of the temperature in the MTT and show how thermal spin wave scattering reduces the spin asymmetry. Finally, an estimation of the part of the collector current that corresponds to truly ballistic electrons will be made for standard experimental conditions. All the graphs presented in this section have been calculated with the aforementioned numerical simulation scheme.

2.5.1 Bias dependence of the collector current

One of the main advantage of MTTs over SVTs is the possibility to study the transport over a given range of electronic energies. As described in section (2.1), the injected electrons will have an energy ditribution centered around eV where V is the voltage applied across the tunnel barrier. MTTs can thus be used as spectroscopic tools to probe the energy dependence of the transport properties of hot electrons in metals and semiconductors. The evolution of the collected current with V however is quite complex as several physical processes ruling the transport in a MTT depend explicitly on the energy of the electrons. The question as to how big an influence those different processes have on the evolution of the collector current with the emitter bias voltage is therefore addressed here. Figure 2.9 shows the collector current in the parallel case calculated within our simulation scheme for a MTT structure consisting of GaAs/Ni(30)/Au(30)/Ni(30)/Al_2O_3/Au in the parallel case. We can see that between $V = \phi_B/e$ (here 0,75V) and $V = 1.2V$, I_{col} increases by several orders of magnitude. The reason for this is twofold: the emitter current I_{em} across the tunnel barrier increases strongly with increasing voltage and the phase space matching the energy and wavevector conditions for collection in the semiconductor scales with $\sqrt{E}$. To distinguish between both effects, one can use the transfer ratio $\alpha = I_{col}/I_{em}$. Its energy dependence is plotted in the inset of the left panel in fig 2.9. We can see that α increases by more than 3 orders of magnitude when the energy is varied between 0,8V and 1,2V. By comparing this value with the increase of the collector current within the same voltage range, we can see that the increase of the collector current with the emitter voltage is mostly due to the augmentation of the phase space in the semiconductor. The GaAs bandstructure is

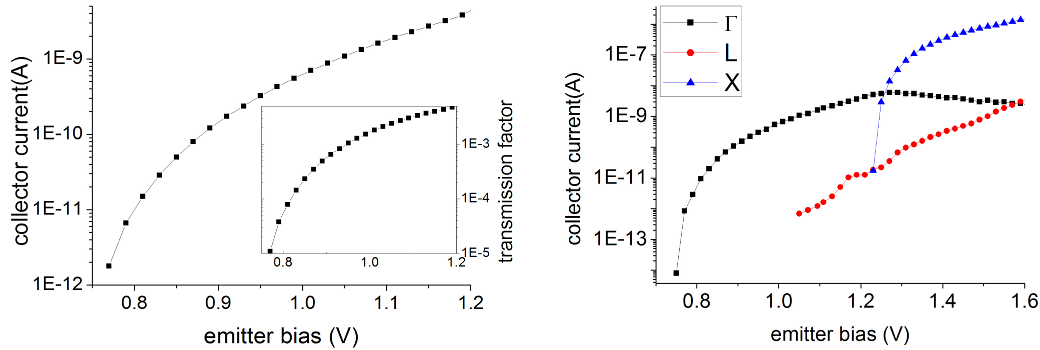

Figure 2.9: Simulated emitter voltage dependence of the collector current in the parallel case for a GaAs/Ni(30)/Au(30)/Ni(30)/Al_2O_3/Au MTT at 11K and without interface scattering:
(left) collector current versus emitter voltage. The inset depicts the evolution of the transfer ratio α
(right) emitter voltage dependence of the contribution of each GaAs valley to the collector current

usually approximated by taking into account three valleys centered at the Γ, L, and X points. The energy separations between the valleys taken here are $d_{\Gamma\mathrm{L}} = 0.29eV$ and $d_{\Gamma\mathrm{X}} = 0.48eV$ and the Schottky barrier height in the Γ valley is $\Phi_\mathrm{B} = 0.75eV$. The right panel in figure 2.9 shows the current collected through each valley. We can see that at low energies, for $E < \Phi_\mathrm{B} + d_{\Gamma\mathrm{L}}$, all the electrons transit in the Γ valley as it is the only valley accessible. As E is increased, states in the L valleys become accessible. However, this is limited to electrons with a high wavevector component parallel to the interface. Due to the fact that the electrons are strongly forward focused due to the tunnel emission, only few electrons will be able to reach the L valleys. Contrary to the L valleys which is centered around zone edges, one of the X valleys is centered around the interface Brillouin zone center. As the effective mass and thus the density of states is much higher in the X than in the Γ valley, as soon as the electrons energy allows it, the electrons will preferentially transit through the X valley. We can indeed see that from $E = \Phi_\mathrm{B} + d_{\Gamma\mathrm{X}}$ on, most of the current is collected in the central X valley. It is to be noted that all the physical processes described so far are spin independent. Consequently, the qualitative features of the collector current in the antiparallel case would be the same.

The differences between $I^\mathrm{P}_\mathrm{col}$ and $I^\mathrm{AP}_\mathrm{col}$ are created during the transit through the spin valve base and can be investigated through the study of the magneto current ratio defined as

$$MCR = \frac{I^\mathrm{P}_\mathrm{col} - I^\mathrm{AP}_\mathrm{col}}{I^\mathrm{AP}_\mathrm{col}}.$$

This ratio will be determined by the relative magnitude of the spin dependent attenuation length in the ferromagnetic layers. As the emitter bias voltage is varied,

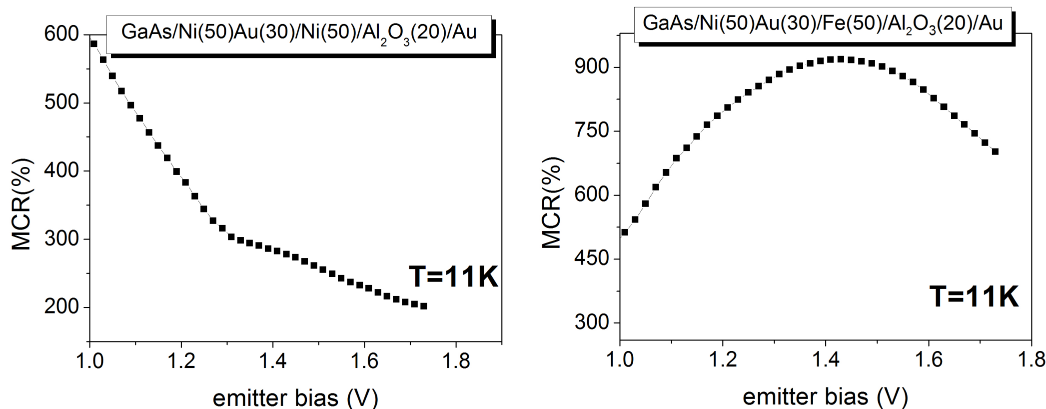

Figure 2.10: Simulation results showing the influence of the base material on the MCR

the hot electrons will probe a different part of the ferromagnets' band structures and their group velocities and relaxation times will vary. Consequently, the magnitude of the MCR will depend on the emitter bias. Furthermore, since the variation of the attenuation length $\lambda_{\uparrow(\downarrow)}$ with the electrons energies is related to the material's band-structure, it is expected that the bias dependence of the MCR will vary qualitatively and quantitatively with the choice of ferromagnetic materials. From the values published by Zhukov and coworkers[37], it can be seen for instance that the evolution of $\lambda_{\uparrow}/\lambda_{\downarrow}$ is qualitatively different for Fe and Ni. As a result, the bias dependence of the MCR is different for those two materials. As an example figure 2.10 shows the simulated emitter bias dependence of the MCR for two MTTs where only one of the ferromagnetic layer differ. We can see that the MTT with a Ni/Au/Ni spin valve base shows a constant decrease of the MCR whereas the one with a Ni/Au/Fe base shows a maximum at about 1.5V. This is in good agreement with an experimental study published in the case of MTTs with a FeCo/Cu/NiFe base[50]. It is to be noted that in the simulation scheme used here, the energy loss caused by any inelastic scattering event (electron-electron scattering or spontaneous spin wave emission) is assumed to be high enough for the scattered electron not to be able to overcome the Schottky barrier. Thus the simulation doesn't take into account the contribution of secondary electrons to the collector current The existence of a maximum in the $MCR(V)$ curve in those simulations is therefore only due to the variation with the energy of the majority and minority attenuation lengths. This non monotonic variation of $MCR(V)$ has been found in other theoretical investigations[51] but the underlying physical reason was to be found in the interplay between electron electron scattering and SSW emission resulting in a spin asymmetry of the secondary electron emission probability.

2.5.2 Influence of structural defects

As shown in section 2.2.2, structural defects act upon the wavevector of the hot electron by randomly redistributing it. We will here address the influence this effect has on the different measurable quantities in a MTT. In the limit of no defect scattering, as has been seen from fig 2.9, most electrons will be collected in the central Γ and X valleys. As D (the scattering parameter defined in section 2.2.2) increases, more and more electrons will be scattered out of the acceptance cone defined by the combination of the collection conditions on the energy and the parallel wavevector. Accordingly, the transfer ratio will decrease by almost three orders of magnitude as can be seen in fig 2.11. This behavior is similar to theoretical results obtained for SVT structures. However those calculations were made for a given excess energy of 0,1eV that was given by the difference between the emitter and collector barrier height. Due to the increase of the collection probability with the electron energy, the influence of defects is expected to vary when the emitter voltage is raised. In order to address this point, the variation of α with D is plotted here for two different emitter voltages. We can see that the transmission reduction with increasing D is stronger at low energies. This observation is consistent with the bandstructure of GaAs: For low energies, electrons with high parallel wavevectors cannot be collected. As the energy increases, electrons can eventually be collected in the outcentered X and L valleys and the effect of defect scattering on the reduction of the transfer ratio is diminished. This fact is clearly visible when comparing the valley contribution to the collector current in the parallel case for D=0 (right panel of fig 2.9) and for D=1 (right panel of fig 2.11). Finally, as the path of the electrons in the base is longer for high parallel wavevectors, the scattering of electrons on defects tends to slightly increase the MCR ($MCR(D=0)/MCR(D=1) \approx 0.9$). However, the reduction of the transmission in the MTT outweighs by far the beneficial effect defects have on the MCR. The minimization of the defect density is therefore highly desired in order to obtain high output devices.

2.5.3 Temperature dependence of the magneto-current ratio

Among the scattering mechanisms involved in the transport of hot electrons the metallic base of a MTT, several mechanisms show a temperature dependence among which phonons and thermal spin waves. Scattering with phonons will only lead to a proportionally similar reduction of both the parallel and the antiparallel collector current and will thus have no influence on the MCR. It has been pointed out as well that the temperature dependence of the spin polarization of hot electrons will have an impact on the collector current in the MTT [51]. However, due to the lack of experimental data on the temperature dependence of the hot electron spin polarization, we will here follow the approach presented by Jansen [52] and focus our attention on the influence of thermal spin waves. Thermal spin waves act on the spin of the electrons they scatter on. The characteristic length for thermal spin

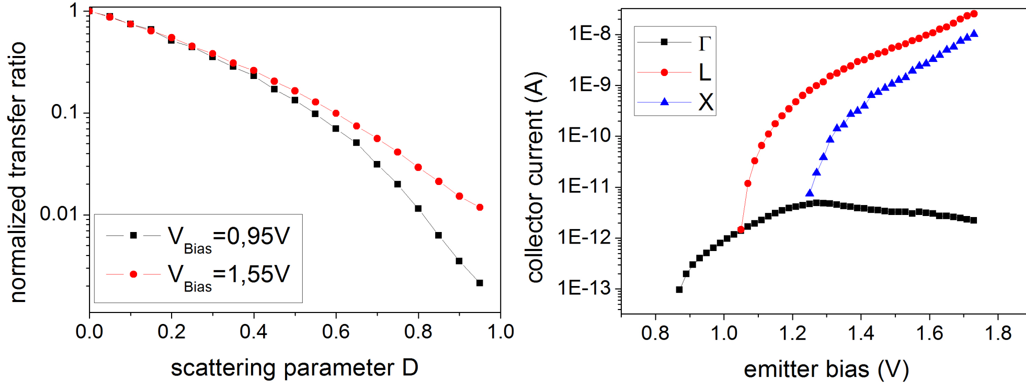

Figure 2.11: Simulation results showing the influence of defect scattering on the transport properties of the MTT:
(left) variation of the transfer ratio with the scattering parameter D
(right) contribution of each conduction channel to the collector current for D=1

wave scattering is the same for minority and majority electrons and thus no spin asymmetry is directly induced by thermal spin wave scattering. However, as the inelastic relaxation lengths are spin dependent, the flipping of a majority (minority) electron spin will increase (decrease) its inelastic scattering probability. Thus the interplay between thermal spin wave scattering and spin dependent inelastic scattering in ferromagnet will induce a temperature dependence of the *effective* attenuation length in MTTs. In order to illustrate this phenomenon, we calculated the density of ballistic hot electrons in an Fe layer of infinite thickness when injected from a Au/Al_2O_3 emitter (figure 2.12). The attenuation here is, due to the absence of a semiconductor collector, only related to the inelastic attenuation of hot electrons in the Fe layer. At T=10K, when the thermal spin wave scattering length is much longer than the inelastic mean free path, the electrons are relaxed at a rate almost equal to the IMFP. When the temperature is increased, the thermal spin wave scattering length gets shorter and some spin mixing between the two spin channels takes place. The majority electrons which undergo a spin-flip will then relax at a faster rate than if their spin had not been flipped and the symmetric effect occurs for the minority electrons. As a result, the attenuation of majority electrons becomes more effective as the temperature increases and the attenuation of minority electrons less effective. This reduction of the spin asymmetry of the relaxation length causes the decrease of the MCR, as plotted in the right panel of figure 2.12 for GaAs/Fe(50)/Au(20)/Fe(50)/Al_2O_3(18)/Au MTT.

2.5.4 Contribution of the purely ballistic electrons

Finally, we would like to address a common misconception in the understanding of the operation principle of the MTT, namely the fact that the collector current is due solely to the ballistic electrons. An example of this misconception can be found

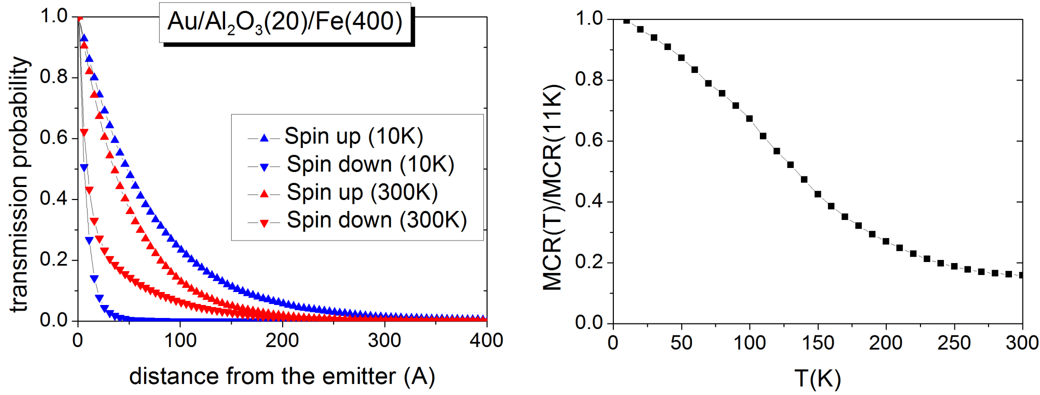

Figure 2.12: Simulation of the influence of the thermal spin wave induced spin mixing:
(left)Inelastic attenuation of hot electrons in $Au/Al_2O_3/Fe$ structure for majority and minority electons at 10K and 300K
(right)temperature dependence of the MCR in a MTT with a Fe(50)/ -Au(30)/Fe(50) spin valve

in the collector current being sometimes referred to as the ballistic current. Another example would be the mere name of the ballistic electron emission spectroscopy technique. As has been shown in the previous theoretical description, several type of elastic scattering have a direct influence on the distribution of the collected electrons and the purely ballistic picture is obviously too simplistic to account for those phenomena. In order to estimate by which amount the collector current is *not* ballistic, we simply counted the amount of electrons having undergone at least one scattering event and that were still collected in the semiconductor and compared it to the total amount of electrons being collected. The results are plotted in figure 2.13 for a GaAs/Fe(50)/Au(30)/Fe(50)/Al_2O_3(18)/Au MTT. The scattering parameter D is taken here to be D=0,6. We can see that at 10K, the collector current is mostly ballistic as long as only the Γ valley is accessible. The small percentage of non ballistic electron corresponds to the electrons elastically scattered on defects who can still enter the Γ valley. When the energies of the electrons become high enough for them to enter the L valley, a strong increase of the non ballistic contribution to the collector current is observable. This is due to the fact that the L valleys have a much higher density of states than the Γ valley and thus the electrons scattered on defects which have a random wavevector distribution will be proportionally more prone to be collected in the L valleys than the ballistic electrons in the Γ valley. Finally when the central X valley becomes accessible, the percentage of ballistic electrons contributing to the collector current remains roughly constant due to the concurrent increase of the phase space in the central X valley that favors the collection of the ballistic electrons and the increase of the phase space in the outcentered valleys where the non ballistic electrons are collected. The same behavior is visible at T=300K, although the variation is damped by the increase of non ballistic

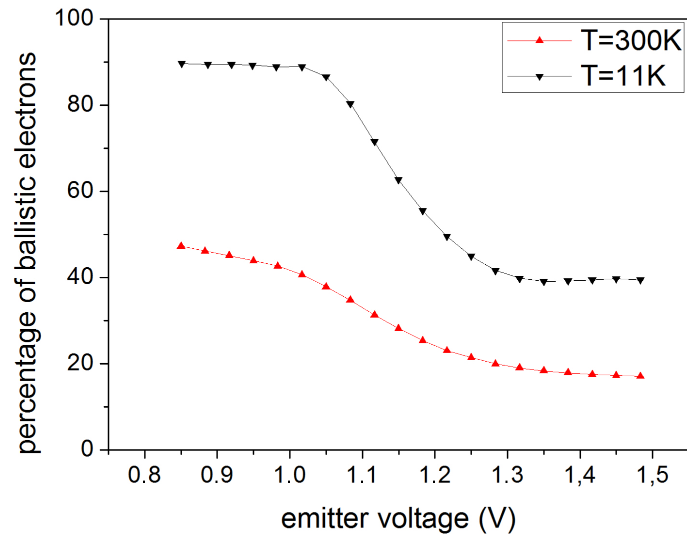

Figure 2.13: Calculated percentage of the collected electrons that are truly ballistic

electrons due to thermal spin waves. Finally, it should be mentioned that the data presented here probably underestimate the real amount of non ballistic electrons since the contribution of secondary electrons is not taken into account.

Chapter 3

Experimental procedures

In this chapter, the experimental methods used for the preparation of a MTT will be presented in detail. First we will describe the deposition setup used to grow the layers. We will then shortly present the layer structure and mask patterns of the MTTs before going through each step of the device fabrication: substrate preparation, growth of the spin valve, deposition of the tunnel barrier, sputtering of the emitter contacts and bonding. The last part will consist in the description of the electrical measurement setup.

3.1 Deposition Setup

The growth of MTTs with epitaxial spin valve base through shadow masks is a complex process requiring the use of both metallic and insulating films. Furthermore, films of a few atomic layers as well as several 100nm thick were needed. For the purpose of the experiment, a deposition setup comprising a MBE chamber including substrate preparation facilities and a sputtering chamber was developed. The MBE chamber was used for the substrate preparation and the deposition of the spin valve whereas the sputtering chamber was used for the rest of the layers. Specific aspects of the MBE technique are the use of very low growth rates (typically 1 atomic layer/minute) and low base pressures which ease the growth of single crystalline layers. In most cases, the degree of crystallinity of the overgrown layers depends directly on the structure of the substrate. In our case, the MBE contained for the substrate preparation a 3keV Varian raster ion gun with an Ar gas inlet and the temperature of the sample could be increased from room temperature to about 650°C. The temperature was measured directly at the sample surface by using a IMPAC pyrometer. For the film deposition, the MBE contained four resistive evaporators capable of temperatures of up to 1500°C. In order to monitor the growth rate and thickness of the deposited material four quartz microbalances were used. The accuracy of the thickness determination was better than 0.1 atomic layer. The surface of the sample could be observed at any time of the process by Reflection High Energy Electron Diffraction (RHEED). The base pressure of the chamber was

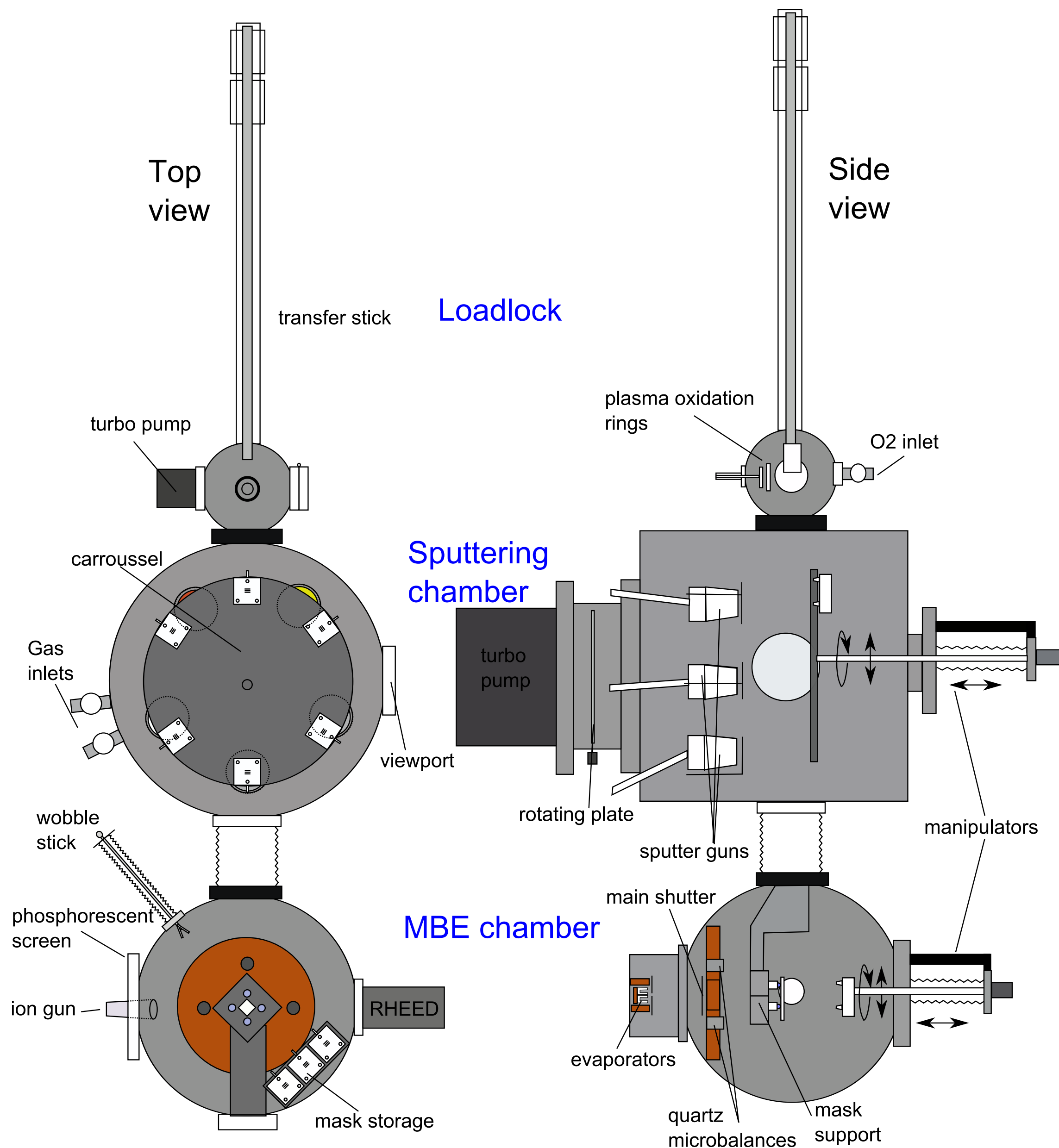

Figure 3.1: deposition setup

1.10^{-10} mbar and during deposition, the pressure was always below 5.10^{-10} mbar.

The sputtering chamber contained five magnetron guns and was connected to the MBE chamber by a gate valve. The sample could thus be transfered from one chamber to the other without vacuum break. The sputtering chamber, with a base pressure of about 3.10^{-8} mbar, could be used for the deposition of metals (in DC mode) as well as thin and thick oxide layers (in reactive or in RF mode). A further possibility to oxidize thin metallic films was added in the loadlock where the films could be oxidized either by natural oxidation or by plasma oxidation. The combination of the MBE and the sputtering techniques together with the possibility to deposit up to nine different materials including conductors and insulators made

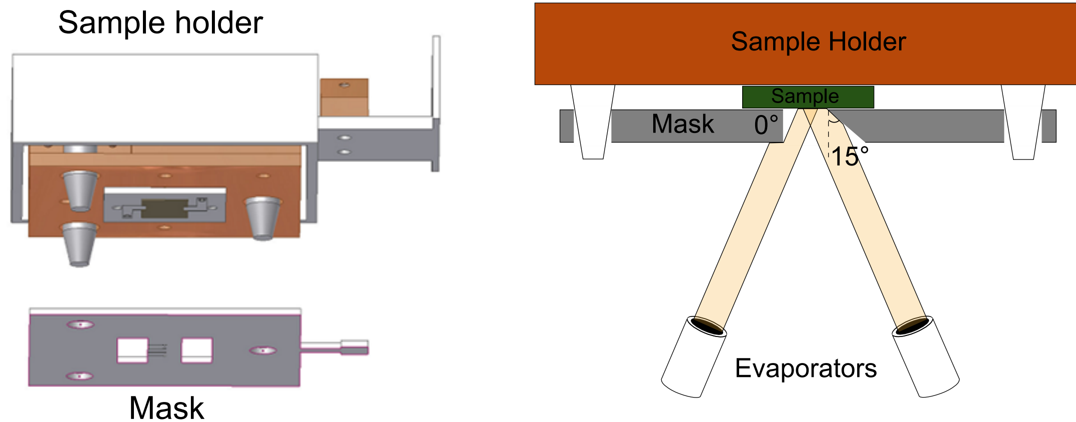

Figure 3.2: Shadow mask system

our deposition setup versatile enough for the successful deposition of MTTs.

In order to exploit at best this versatility, we further included a shadow mask system in both chambers, thereby bypassing the need for optical lithography patterning and its shortcoming regarding process transferability. Up to 4 different masks in the MBE chamber and 6 in the sputtering chamber could be stored. The system we developed is depicted in figure 3.2. The negative pattern of the structures to be deposited were first etched in the center of 1mm thick, 40×40 mm^2 non magnetic steel plates by spark erosion. Since the fabrication of a MTT consist in the superposition of different patterns, several masks were needed for the fabrication of a complete MTT. In order to insure the reproducibility of the positioning of the masks with respect to the sample, we use a self aligning system: Three conical pins are attached to the sample holder and their positions with respect to the sample are kept constant throughout the fabrication process. The masks comprise three holes matching the position of the pins. The self aligning process is achieved by pressing the sample holder against a shadow mask while allowing the shadow mask to freely move laterally. As the pins fit in the holes, due to the conical shape of the pins, the vertical and lateral position of the mask with respect to the sample is set. The pins' height is adjustable in order to setup the distance between the masks and the sample. In the MBE, due to the fact that the mean free path is much longer than the distance source-substrate, the trajectories of the atoms in the molecular beam are roughly straight lines. The four evaporators are positioned next to each others and each of them provides a molecular beam impinging on the substrate with an angle of incidence of about 10° away from the normal to the sample's surface. Due to the finite thickness of the mask and this non normal incidence, the edges of the structures on the masks had to be etched with an angle bigger than the angle of incidence to prevent a shadowing effect. The case where the edges are etched with an angle of 0° and 15° are depicted in the right panel of figure 3.2. Even if most shadowing is removed by this technique, there exist always a non zero distance between the mask

and the sample and some shadow will exist on the side of the structure opposite to the beam. As a result, the structures on the sample will be slightly shifted toward the direction opposite to the incoming direction of the beam. The direction of this shift will thus vary with the evaporator used. The combination of all those elements yields an accuracy in the definition of the structures dimensions and positioning of about a couple of micron. The main limitation of this system is the minimum size of the shadow mask patterns which is about $200\mu m$. This boundary is defined by the diameter of the metallic wire used during the spark erosion process.

3.2 Sample fabrication

3.2.1 Substrate preparation

The first step in the fabrication of a MTT is the preparation of the substrate. The structural quality of the overgrown layers and their resulting electric and magnetic properties will depend to a large extent on the properties of the substrate. The quality of the substrate preparation can be assessed regarding two main aspects: The chemical contamination present at the GaAs surface and the surface structural quality, especially the nature and magnitude of its roughness. We will describe here the methods used to optimize those two aspects.

We start from a commercial GaAs(001) wafer from Wafertech with a dopant concentration of 1-2 10^{16} cm^{-3}. The wafer is first cut into roughly $1 \times 1cm^2$ pieces which is the substrate size used in the deposition setup. During the cutting process, GaAs particles are usually released and part of them will be redeposited on the surface thereby locally increasing the roughness drastically. In order to prevent this from happening, the wafer is coated with photoresist prior to being cut. Once we obtain a substrate with the desired dimensions, the surface is cleaned in an acetone ultrasonic bath for a few minutes and then rinsed with isopropanol. A drop of liquid In/Ga eutectic is then deposited on the reverse side of the substrate. The liquid metal insures that a good thermal contact will exist between the substrate and the sample holder. Furthermore, upon annealing, it will alloy with the GaAs thus forming an Ohmic contact with the GaAs, which is necessary for electrical measurements. The sample is then mounted on the sample holder, introduced in the loadlock of the deposition chamber and finally transfered to the MBE chamber.

Due to its prolonged exposition to atmospheric conditions, the first few nm of GaAs are contaminated with oxygen and carbon. As a result, the surface is amorphous as ascertained by the RHEED picture of such a surface showing only a diffuse background. The first technique considered here to remove those contaminants is the consecutive actions of ion bombardment and annealing. Bombardment of the surface with low energy Ar ions is used to etch away the first topmost atomic layers

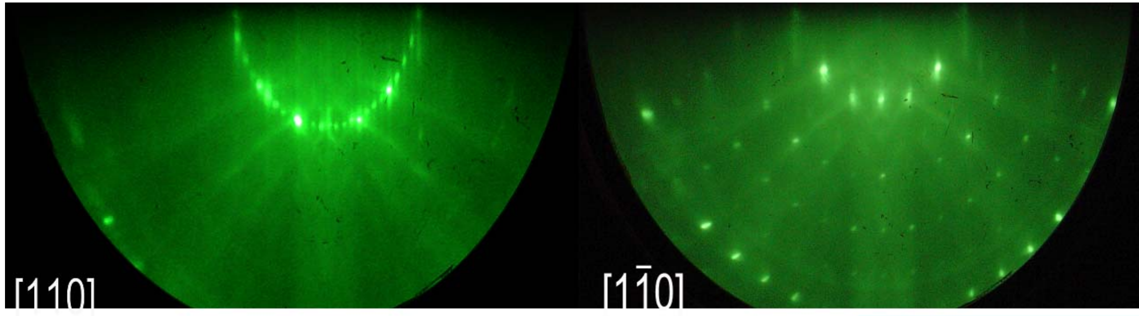

Figure 3.3: RHEED diffraction pattern along the [110] and [1-10] axis of a GaAs (001) surface prepared by ion bombardment and annealing. Along the [110] axis a clear fourfold reconstruction is visible hinting at a pseudo (4×6) reconstruction.

together with their contaminants. This process however induces a high concentration of defects due among others to the incorporation of Ar ions in the GaAs matrix and to the creation of structural vacancies. Those defects can be healed through annealing of the substrate. Indeed, at high temperature, the atomic diffusion is strongly increased which favors the reduction of the defect density at the surface. Furthermore, the embedded Ar atoms will desorb, thereby creating a smooth defect and contaminant free surface. This method is fairly straightforward and has proven to effectively produce high quality GaAs surfaces. Careful attention however has to be taken for the optimization of this process: The etching rate is related to the density and the energy of the ions. Whereas the ion density is always set to a maximum so as to reduce the etching step duration, the energy has to be carefully set as higher energy means faster etching but higher defect concentration. Similarly, the higher the annealing temperature the faster the surface will recover its crystalline quality. However, the well known problem of GaAs dissociation leading to As_2 desorption and the formation of Ga-Ga bonds creating microscopic Ga droplets on the surface at a temperature of about $620°C$ sets an upper temperature boundary for the annealing. In this work we used a method based both on the previous work developed in the AG Bayreuther and on our experimental requirements and capabilities:

1. We start by increasing the substrate temperature while monitoring the reflected beam from the RHEED. At about $500°C$, the native oxide is desorbed and a diffraction pattern becomes visible within a few seconds. This pattern is characteristic of a rough crystalline surfaces where the electron beam interact with a 3D structure rather than a surface. A rms peak to peak roughness of 10nm was measured by ex situ AFM.

2. The surface is sputtered by Ar ions for 2h30. The ions energy is 0.6kV and the Ar pressure is 1.10^{-6} mbar leading to a ion current density on the substrate of $32\mu A.cm^{-2}$

3. The sputtering process is interrupted and the temperature of the substrate is increased in steps of $10°C$ every ten minutes. The increase is stopped when

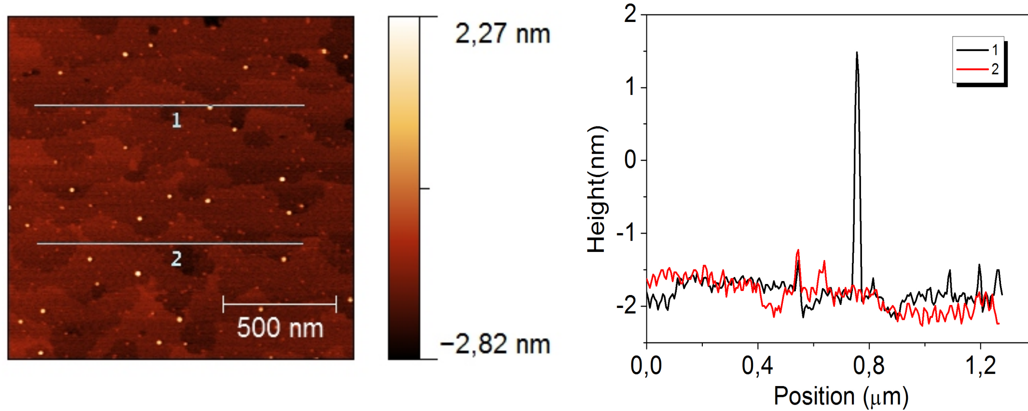

Figure 3.4: Scan of a GaAs surface prepared by ion bombardment and annealing. The dots are Ga droplets originating from a too high annealing temperature.

the RHEED pattern characteristic of a smooth surface, the so called Laue circles, with a (4×6) reconstruction is visible (fig 3.3) or when the maximum temperature of $620°C$ has been reached.

4. If no Laue circles are visible at this temperature, steps 2 and 3 are repeated.

With this method, smooth crystalline GaAs surfaces could be obtained. The measured peak to peak roughness was below 1nm and large atomically flat terraces could be observed. However, due to the narrow temperature window within which a smooth substrate without Ga droplets can be obtained, only a partial reproducibility was achieved. This is related to the fact that the substrate preparation was taking place in the MBE chamber where metals were regularly evaporated: As more and more material is deposited onto the glass window, its reflection index changes and the amount of thermal radiation measured by the pyrometer varies. As a result, the inaccuracy of the temperature readings was slightly increasing with time. The approximate determination of the substrate temperature led to variations of the substrate quality: An overestimation of the temperature resulted in an increase surface roughness. An underestimation of the temperature could in the worst case lead to the appearance of Ga droplets on the substrate as shown on figure 3.4. Depending on the maximum annealing temperature, the heights of those droplets varied between 1 and 15 nm.

Alternatively, the substrates could be prepared by a chemical etching method prior to introduction into the deposition setup. Among the several possibilities, we focused on the use of HCl solutions due to the numerous reports of the higher substrate quality it produces as compared to other chemicals [53][54][55]. Before being mounted on the sample holder, the substrate was dipped in a 37% concentrated HCl solution for 3min and then rinsed with isopropanol. The sample was then mounted on the sample holder and introduced into the chamber's loadlock. In

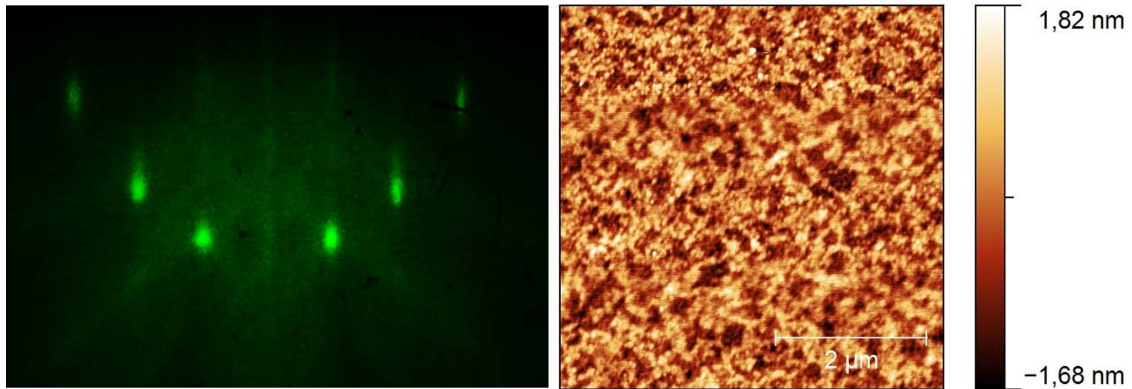

Figure 3.5: RHEED diffraction pattern and AFM scan take ex-situ of a GaAs (001) surface chemically prepared with HCl

order to minimize a reoxidation of the GaAs, the duration of the mounting and introduction was kept below two minutes. Once in the MBE chamber, the RHEED diffraction pattern of the surface was first observed without any further treatment. A clear pattern in between the 3D pattern and a Laue circle was visible, indicating that the surface oxide due to the 2 minutes exposure to air was very thin and that the surface roughness was substantially lower than if the native oxide had been thermally desorbed. We further annealed the substrate at $500°C$ for 30 min to get rid of the potential rest of isopropanol, the water that accumulated on the surface during its exposure to air and potential surface oxides. The RHEED diffraction pattern obtained is shown in figure 3.5 together with an AFM scan of the surface taken ex-situ. The peak to peak roughness is about 2nm which is substantially lower than for the substrates measured right after the thermal desorbtion of the native oxide but more than twice the roughness measured on substrate prepared by sputtering and annealing. In conclusion, this method yields in the end a lower substrate quality than the other one but is obviously much more time efficient. The magnetic and electric characteristics of samples will be influenced to some extent by the substrate structural quality and the effect of both methods on those properties will be presented in the next chapters.

3.2.2 Layer structure and mask layout

A MTT consists in a complex multilayer including semiconducting, metallic and insulating films. In order for each layer to fullfill its purpose, certain technological aspects apart from the growth properties themselves need to be considered carefully. We will here present the layer structure together with the masks used for each layer. The issues relevant to the mask design will also be discussed.

The first step consists in the deposition of a spin valve element onto the semiconductor substrate. As mentioned in a preceding section, the non normal incidence

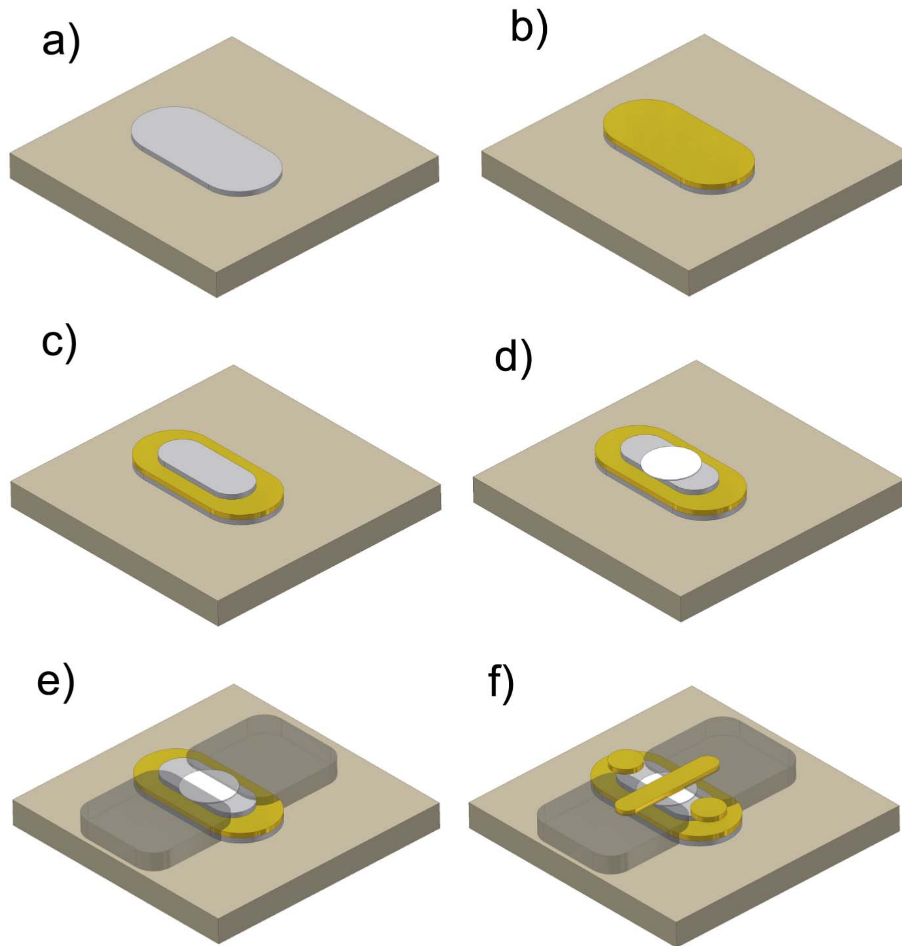

Figure 3.6: layout of the mask patterns and material used for each step in the fabrication of a MTT

of the molecular beam necessarily implies that some shadowing effect takes place during deposition through a mask. The two FM layers of the spin valve need to be separated one from the other by the Au spacer so that no direct FM coupling can exist between them. In order to avoid a contact at the structure edges due to the different impinging direction of the FeCo and Au molecular beams, we used two masks for the spin valve. The shape of the first mask is roughly that of a rectangle which sides are $700\mu m$ and $1200\mu m$ long. Due to the impossibility to machine right angles with the spark erosion technique, the corners are rounded with an angular radius of 150 μm, which is the steel wire's diameter. This mask is used for the first FM layer and the gold spacer (a) and b) in fig. 3.6). The second FM layer is deposited through a mask which has the same shape as the first one but has an area of $400{\times}900\mu m^2$ (c). A circular mask of $500\mu m$ radius is then used for the deposition of the tunnel barrier (d). In order to insulate the emitter contact from the substrate and to reduce the effective tunneling area, a thick Al_2O_3 layer is deposited through a mask such that only a $200\mu m$ wide channel is left open in the center of

the MTT (e). Finally, the base and emitter contacts are deposited through a last mask (f). The width of the stripe used for the emitter contact is $200\mu m$ making thus the active area of the tunnel barrier $200*200\mu m^2$. This area is quite large but was determined by the minimum machining sizes achievable by spark erosion. A positive aspect of the big tunnel barrier area though is that it reduces the tunneling resistance and should thus improve the signal to noise ratio. The two base contacts have a diameter of $300\mu m$.

3.2.3 Epitaxial spin valve growth

The deposition of the spin valve base takes place in the MBE chamber. For the spin valve system, we use a trilayer of $Fe_{34}Co_{66}$/Au/$Fe_{34}Co_{66}$. The $Fe_{34}Co_{66}$ alloy has a bcc structure due to its high Fe content and its lattice constant and growth properties on GaAs (001) resemble the ones of Fe. Its spin polarization is however higher than that of Fe and a higher magneto current ratio is thus to be expected. In the following, FeCo will always refer to the alloy $Fe_{34}Co_{66}$ used here. The lattice constant of bcc-FeCo ($a_{\mathrm{FeCo}} = 2,8266$Å) is almost exactly half of the one of GaAs ($a_{\mathrm{GaAs}} = 5,6532$Å). Gold has a fcc structure in which the distance between nearest neighbor atoms (direction [110] or equivalent) is 2,884Å. The lattice mismatch in the (001) plane between FeCo and Au is thus below 2% when the gold lattice is rotated by 45° around the [001] axis. We can therefore with this choice of material expect that an heteroepitaxial growth is possible leading to a fully epitaxial spin valve. It was furthermore possible to benefit from a long experience gathered in the AG Bayreuther regarding the growth and magnetic properties of cubic FeCo on GaAs substrates. The previous studies showed that if the growth takes place at room temperature, negligible intermixing occurs between the GaAs and the FeCo. The minimization of this chemical roughness is essential to the operation of our MTT in order to obtain a high quality Schottky barrier. We therefore deposit the first FeCo layer only when the substrate temperature has cooled down to room temperature. The FeCo is evaporated from a Knudsen cell whose evaporating power is first increased while monitoring the quartz microbalances until a rate of 1ML/min is obtained. Once the rate is stable, we open the shutter obstructing the molecular beam from the sample. The deposited FeCo thickness depends on the desired electrical and magnetic response of the MTT and therefore varies in this work between 15 and 35 atomic layers. The RHEED pattern after deposition of 22ML is shown in figure 3.7. The pattern is characteristic of bcc-FeCo(001) crystalline structure. The wide streaks indicate that the surface is relatively rough. It is known that cubic FeCo grows on GaAs in a Volmer-Weber mode. The adsorbed FeCo atoms first form islands on the substrate. As more atoms impinge on the surface, those islands grow both laterally and vertically and eventually coalesce to form a closed layer. This growth mode leads to an increased surface roughness as compared to the one of the substrate. It has been measured on samples grown in an almost identical deposition

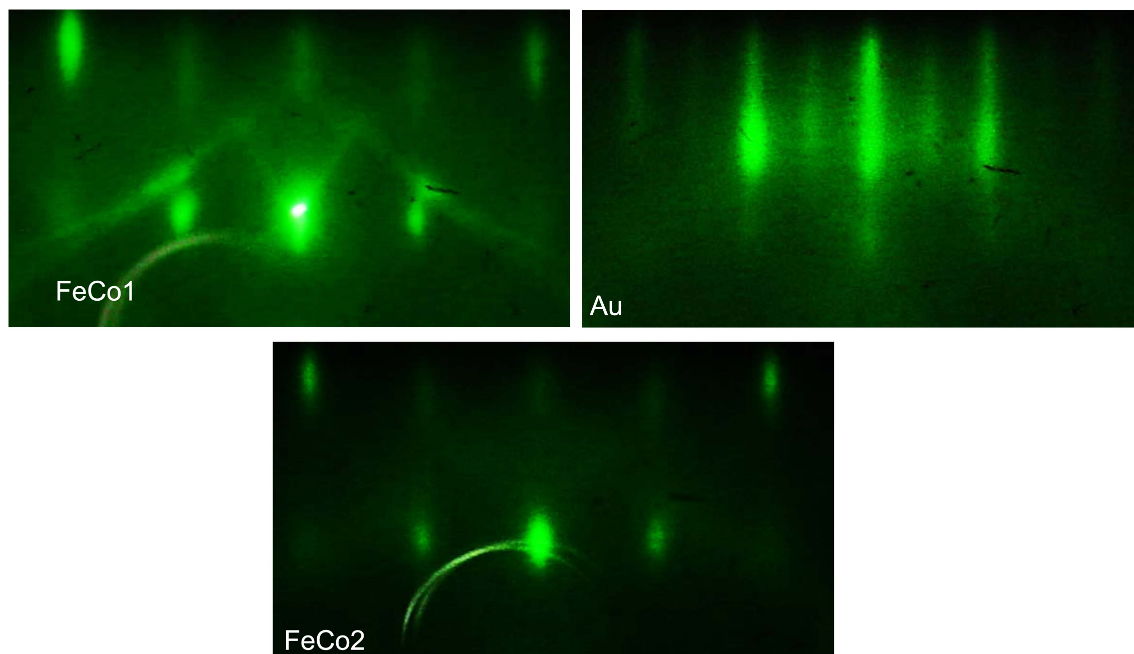

Figure 3.7: RHEED diffraction pattern of the spin valve's layers

setup that the peak to peak roughness increases from 0,6nm to 3nm when 25 ML FeCo are deposited on GaAs[21]. There has been reports that through ion bombardment and subsequent annealing at temperatures of about 200° C, the surface roughness of Fe(001) or FeCo(001) grown on GaAs(001) can be reduced[56][57]. The necessity in our case to avoid any kind of intermixing between the FeCo and the GaAs forbids the use of annealing temperature higher than 100° C and thus no post growth improvement of the surface quality is possible.

Subsequently, the gold layer is evaporated from a Knudsen cell in a similar fashion as the FeCo. It was found in our case that the desired magnetic properties could be obtained from 12 ML on but thicker Au thicknesses proved to provide a better magnetic switching of the spin valve probably due to a reduction of the orange peel coupling. On the other hand, the hot electrons traversing the gold layers will relax in a spin independent fashion leading to a reduction of the output current that scales exponentially with the gold thickness. A trade-off has therefore to be found and the optimum was in our case a spacer's thickness of 16ML. The RHEED of the gold surface shown in figure 3.7 clearly indicates a crystalline structure. A $p(2 \times 2)$ reconstruction originating from the diffusion of As at the surface is visible. The long streak are characteristic of a rough surface with islands a few nm height.

Finally, the second FeCo layer is evaporated. We used thicknesses comprised between 25 ML and 35 ML. The reduction of the RHEED intensity as compared to the first FeCo layer indicates that the layer has a somewhat reduced crystalline quality but remains nevertheless epitaxial.

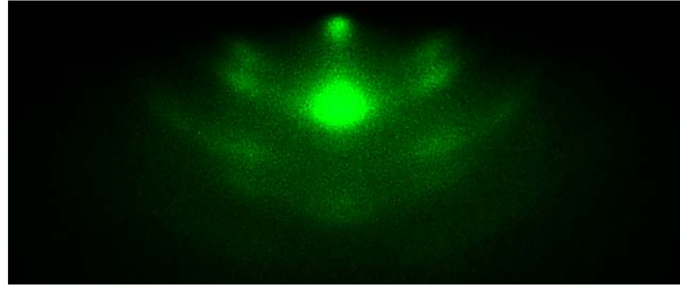

Figure 3.8: RHEED diffraction pattern of a 6ÅAl layer deposited on preoxidzed FeCo

3.2.4 Tunnel barrier deposition

The tunnel barrier is a key element in a MTT. For an optimum operation, the barrier should have a resistance as low as possible in order to increase the collector current. Furthermore, the breakdown voltage should be high so as to maximize the operational range of the MTT. Finally the barrier should have a low noise and its electrical properties should remain unaffected over long measurement times under high applied biases. The simultaneous optimization of all those parameters is however impossible as they scale inversely both with the barrier thickness and the chemical composition. As mentioned in the introduction, it was found in a previous work that the tunnel barrier was the most critical element and its poor quality was the reason why the improvement of the transfer ratio due to the epitaxiality of the spin valve could not be assessed. To palliate this problem, several methods have been used in this work to deposit the tunnel barrier and will be described here, along with their advantages and disadvantages.

Aluminum oxide

Ever since the development of spintronics, extensive research has been dedicated to the study and optimization of the deposition of thin oxide films for TMR elements. Most of it has been focused on the use of aluminum oxide. In most cases, advantage is taken of the propension of Al to wet surfaces leading to the deposition of very smooth films and the oxide is formed by oxidizing a predeposited metallic Al film. In this work two oxidation methods have been used: Natural oxidation and plasma oxidation.

Natural oxidation consists in the exposition of an aluminum surface to an oxygen atmosphere. The oxidation mechanism takes place at the Al grain boundaries. Once the grain surfaces are oxidized, metallic Al diffuses from inside the core to the surface and gets oxidized. It is thus of practical interest to reduce the grain size of the deposited metallic aluminum since it favors the oxidation process and furthermore, reduces the surface roughness and the risk of pinholes. In our case, it is expected that the epitaxial FeCo template on which the Al is grown will increase its grain size. For this reason we start by exposing the topmost FeCo surface to

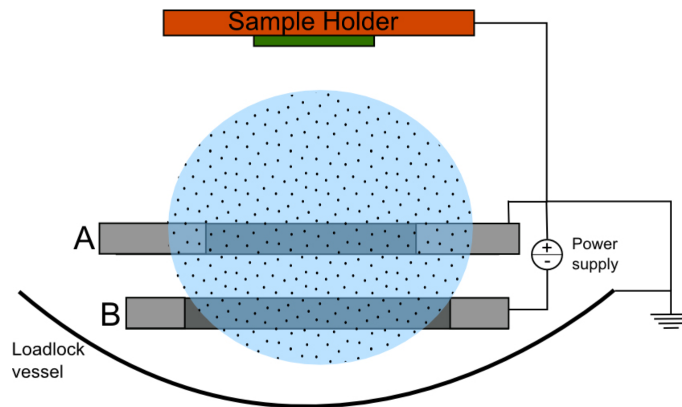

Figure 3.9: Plasma oxidation setup.

an 10mTorr pure oxygen atmosphere for 2min. The structural deterioration of the surface was ascertain by RHEED where a strong reduction of the intensity indicates a partial amorphization of the surface. Furthermore, if we compare the MOKE measurements of such layers capped by 5nm metallic Al with the ones of samples with the same layer structure but where the FeCo layers has not been exposed to an oxygen atmosphere, no difference is visible. This shows that the FeCo is either only very superficially oxidized or even that the oxygen present at the FeCo surfaces diffuses inside the metallic aluminum, leaving the FeCo unoxidized. A thin Al layer is then sputtered onto the surface. In order to further reduce the grain size and roughness, we use the lowest Ar pressure allowed by our magnetron guns (1.10^{-3} mbar) and the highest sputtering power allowing us to still accurately control the deposited thickness (50W), yielding a deposition rate of 1,77Å/sec. Through this method we can maximize the kinetic energy of the deposited atoms and thus increase the surface mobility, leading to a reduced roughness and grain size[58]. In an analysis of the natural oxidation kinetics of Al, Jeurgens showed that the oxide thickness is limited to about 7Å at room temperature[59] and similar observations were made by Hagler[50]. For this reason, we performed a stepwise oxidation by first depositing 6Å of metallic Al and then oxidizing it in the loadlock in a 100mbar pure oxygen atmosphere for 10min. This process is repeated up to 6 times depending on the desired Al_2O_3 thickness. The RHEED diffraction pattern of the first 6Å metallic Al presented in figure 3.8 shows that the Al still grows in a polycrystalline way on the preoxidzed FeCo. Furthermore, the diffraction pattern of the FeCo has completely disappeared indicating a close Al layer. The thermal oxidation process is technically easy to achieve and low thickness barriers with well controlled oxygen concentrations can be achieved. However, the stepwise deposition of the oxide is time consuming. Except for the case where low $R \times A$ sub-nanometer barrier are required, the plasma oxidation technique is usually preferred due to its speed and reliability.

When an oxygen plasma is created, the interactions between electrons and the O_2 molecules present in the gas result in the creation of different oxygen compounds and ions. More specifically reactive particles which require much lower activation

energies for the dissociation process that take place during oxidation such as O_3 or O will be created. As a result, the oxidation efficiency and speed will be greatly enhanced. For the purpose of our experiment, we integrated in the loadlock a plasma oxidation setup. The setup is described in figure 3.9. The loadlock is filled with a 99,99% purity O_2 gas. A rotationally symmetric DC glow discharge is then created with a negatively biased ($\approx 600V$) Al ring (ring B in figure 3.9). The ring is biased by using a advanced energy MDX 500W power supply. In between the Al ring and the sample, a second grounded Al ring is used to shield the sample from the ions sputtered from the negatively biased ring. The distance between the two rings is 2cm and the sample is lying some 4cm above the plasma.

In order to obtain the time necessary to the formation of a stochiometric Al_2O_3 layer from a plasma oxidation of a 2nm metallic Al, we calibrated the setup by depositing a Al(2nm)/Co(5nm) multilayer. Each Al layer was plasma oxidized and the oxidation time was varied from 10 to 100 sec. A XPS depth profile was then performed on the multilayer where the Al_{2p} and $Co_{2p3/2}$ peaks where measured. Since for a given material, the electron binding energies depends on the valence state of the atom as well as on his chemical environment, a chemical shift of the binding energy is observable when this material is oxidized. In this way we could obtain the required time for having a fully oxidized Al layer without any oxygen diffusion in the underlying electrode. The oxidation time fulfilling those requirements was found to be 90 sec at a pressure of 75 mTorr and at a power of 10W. Given those conditions, the barrier deposition and oxidation is as follows: we start by depositing 2nm metallic Al at the same power and Ar pressure as for the natural oxidation. The sample is then transfered into the loadlock where it is plasma oxidized under the optimum experimental conditions described above.

Magnesium oxide

MgO has been used as a barrier material extensively in last few years due to the high TMR it yields. In our case, the high TMR values are not relevant. MgO however offers several advantages: numerous experimental reports confirm that it is a well suited for being used on epitaxial bcc-Fe or bcc-FeCo templates[60][61], the potential high grain size of the oxide should lead to less scattering at the oxide-FeCo interface and potentially increase the output current and finally the deposition from a MgO target makes the deposition process easier by bypassing the need of further oxidation and its necessary increase in experimental unknown variables. We deposited the magnesium oxide from a pressed MgO target by RF sputtering in a 1.10^{-3} Ar atmosphere at a power of 75W yielding a deposition rate of 0,15Å/sec. As in the case of Al, a lower Ar pressure tend to to produce smoother films[62]. The RHEED diffraction pattern of the MgO surface deposited using the described parameters was extremely diffuse and only very faint reflexions were visible indicating that the MgO was growing in a polycrystalline way with a small grain size.

3.2.5 Insulation pads and top contacts

In order to insulate the top contacts from the GaAs surface, a thick Al_2O_3 layer is required. A direct contact between the emitter electrode (negatively biased) and the grounded substrate would result in a spurious current flowing directly from the electrode into the substrate. We use for this purpose a mask with two $1{\times}1mm^2$ big squares separated by a $200\mu m$ bridge (fig. 3.6 e)). The oxide deposited through this mask will thus serve two purposes: first to insulate the emitter contact from the substrate and second to reduce the active tunneling area defined by the contact area between the emitter electrode and the barrier oxide material. The methods to deposit aluminum oxide described in the previous subsection are well suited for thin oxide layers. However, it would be extremely time consuming to use them to grow thick layers ($\approx 250nm$). For this reason, the insulating pads are deposited by DC reactive sputtering. Reactive sputtering is the sputtering of an elemental target in the presence of a reactive gas that will react with the elemental atoms at the condensation areas in order to form a compound. It is usually assumed that only the reaction at the substrate will lead to the formation of a compound film. However, the reactive gas strongly interact with the elemental material at the target site modifying the target electrical properties and leading to the well known hysteretic behavior (fig. 3.10): When the flow rate of reactive gas (O_2 in this case) is increased, all of it will first be used through the reaction with the sputtered atoms at the substrate surface and the target surface will remain conducting. This situation prevails until the point where the flow rate of O_2 becomes faster than the gettering rate due to the oxidation at the sample's surface, i.e. a stoichiometric oxide is formed (point A). The excess gas then reacts with the target surface forming an oxide layer. The sputter rate of the oxide is usually 10 to 20 times lower than that of the metallic element. The reasons for this are the lower sputtering yield of the compound, the increase of the secondary electron emission coefficient of the oxides and the higher energy consumption resulting from it[63]. Since the sputter rate is decreased, so does the gettering of oxygen and the P_{O_2} increases. Eventually the O_2 flux will be too high and a cascade reaction will occur leading to a target in a fully oxidized state (also called poisoned state) where the sputtering rate and the oxygen consumptions are minimum (point B). When the flow of reactive gas is reduced from point B, the oxygen partial pressure will be reduced linearly until the compound material at the target surface is broken through (point C), at which point the sputter rate increases together with its getter action and the oxygen partial pressure will drop to its initial low value (point D). In order to sputter high quality compound materials films at high rate, it is necessary to operate in the very unstable region between the points A and B where the target is still metallic but where the amount of reactive gas is sufficient to form stoichiometric compounds. In this region, the amount of target surface that is oxidized depends on the ratio R of the oxidation speed of the target to the sputtering rate of atoms from the target.

Complicated feedback techniques can be used to vary the O_2 flow rate during

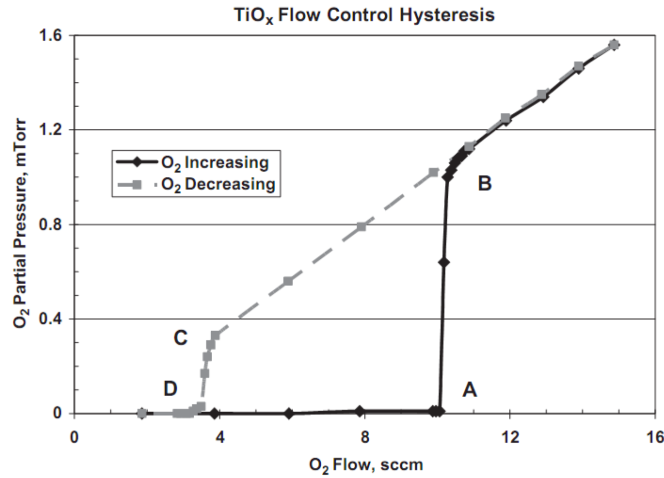

Figure 3.10: hysteresis cycle describing the DC reactive sputtering process from [64]

deposition to keep R constant. Since in our case the geometry allowed it, we used a much easier technique to stabilize the process: At small target to substrate distance (TSD), a high proportion of the sputtered atoms will reach the substrate. Inversely at large TSD the proportion of atoms sputtered from the target actually reaching the sample is smaller. The O_2 flux needed to obtain stoichiometric oxides depends on the impinging rate of elemental atoms at the sample's surface. This means that the required O_2 flux is lower for large TSD. Since however the sputtering rate at the target is barely modified by increasing the TSD, the value of R will be influenced solely by the O_2 flux. It is thus possible for large enough TSD to operate the target in the metallic mode and still obtain stoichiometric films at reasonable rates[65]. It is to be noted that the reduction of deposition rates resulting from the large TSD (usually a factor 2 or 3) is very small as compared to the reduction of deposition rates that would result from operating the target in a poisoned mode (factor 15 at least). Furthermore, the operation in poisoned mode leads to arc formations at the target which considerably reduce the homogeneity of the deposited films. The procedure used in this work is then as follows: First a 1:10 O_2-Ar gas is let in the deposition chamber till reaching a pressure of $1.25.10^{-3}$ mbar. The TSD is set at 300mm. We then ignite the plasma by using a DC power supply in power regulation mode with a power set at 50W. An immediate decrease of the gas pressure is visible due to the reaction of the oxygen with the Al at the sample surface. We can extrapolate the oxygen consumption from the total pressure decrease since the ratio of gas flux and the total pressure before sputtering is known. In order to make sure that the deposited film is indeed stoichiometric, the gas flux ratio was chosen so that a slight residual excess of oxygen was always present. The target contamination state is known by monitoring the cathode voltage which varies with the secondary electrons emission coefficient. We can thus ensure that the target operates in a metallic mode by comparing the cathode voltage during reactive deposition to the

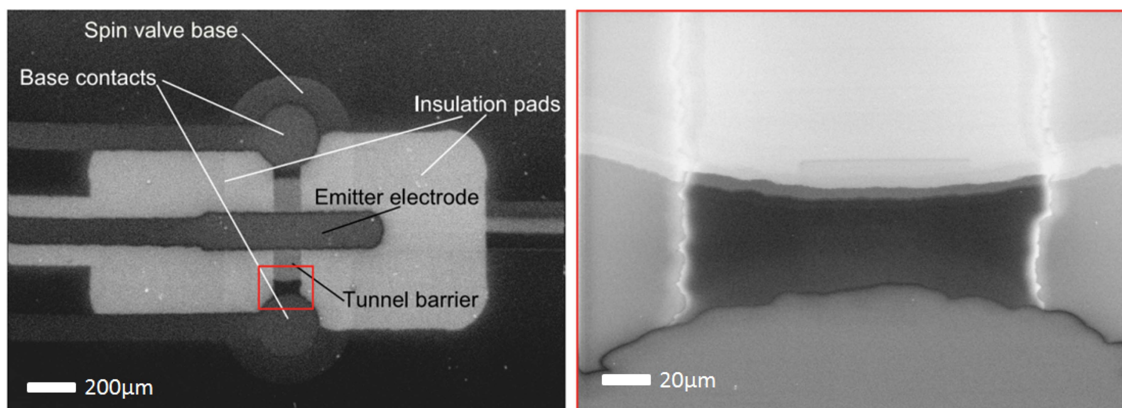

Figure 3.11: SEM picture of a full MTT fabricated by shadow mask. on the left, a full view of a MTT is shown. On the right, the part depicted by the red square is magnified

one measured during sputtering with only Ar. This process proved to be extremely reproducible and stable once the right sputtering parameters were found. With the deposition parameters described above, the 250nm Al_2O_3 were sputtered at a rate of 0,625Å/sec.

The top contacts for both the emitter and the base are then sputtered. The contacts consist in a bilayer of Ta(20nm)/Au(100nm) sputtered at 50W, the Ar pressure being 2.10^{-3} mbar. the Ta is used as an adhesion layer for the Au cap necessary for the sample bonding.

3.2.6 Comment on the shadow mask process

The completed MTT can be seen on the scanning electron microscope picture shown in figure 3.11. We can see that the mask positionning accuracy is more than enough for the fabrication of MTTs with those dimensions. The magnification of the part depicted by the red square is shown in the right panel. The edge roughness can be estimated to be about $8\mu m$. The layers deposited by MBE, where the atom in the molecular beam have a low kinetic energy and reach the surface almost perpendicular to it, had dimensions almost identical to the one of the mask. The dimensions of the thick layers grown by sputtering are however on average about $10\mu m$ longer than the ones of the masks through which they have been produced. This is due to the fact that the sputtered atoms impinge on the sample surface with a wide angular distributions and with a high kinetic energy resulting in an increased surface mobility and thus the atoms will tend to be deposited further inside the small distance between the sample surface and the mask. This effect can be reduced by ensuring that the alignment pins on the sample holder are adjusted in such a way that the distance between the sample surface and the mask is minimized. However, a sample-mask distance below 2 μm couldn't be achieved with our system without

risking that the mask touches the sample surface.

For the same reason, the morphology of the edges is as well influenced by the deposition process. The edge width was found to be about $1\mu m$ for the layer deposited by MBE and between $5\mu m$ and $10\mu m$ depending on the layer's thickness, for the ones deposited by sputtering. As along the width of the edges, a thickness gradient exists, it is particularly important to deposit the ferromagnetic layers by MBE rather than sputtering in order to minimize the switching field inhomogeneities due to the thickness gradient.

3.2.7 Bonding

At the end of the deposition process, each sample will contain four MTTs. In order to be measured, the MTTs need to be put onto a home made 20 contacts chip carrier. The surface onto which the MTTs can be placed is defined by a 5mm diameter circular copper plate that will insure a good thermal conductivity between the sample and the cryostat cold finger. We therefore start by cutting the sample in order to obtain two 3×3 mm^2 pieces each of them containing two MTTs. One of the pieces is then used immediately while the other one is stored for further measurements. The sample piece is then glued onto the copper bottom of the chip carrier with a two component conducting silver paste. This step is necessary in order to insure a good thermal contact between the sample and the copper ring. After 12 hours, the silver paste has dried. The sample is then bonded by means of an ultrasonic bonder. Au wires are used to contact the emitter and base contacts to the chip carrier in a four point geometry. The collector contact is measured directly at the copper plate which is in electrical contact with the reverse side of the GaAs substrate through the silver paste. The annealed InGa eutectic on the GaAs backside insures that this contact is Ohmic. In order to protect the tunnel barriers from electrical static discharges during the bonding process, all equipments, including all the chip carrier pins, are connected to ground during the whole duration of the bonding.

3.3 Electrical measurement setup

To fit the requirements of our experiment, a special low temperature transport measurement setup has been created using a closed cycle cryostat. On its cold finger a receptacle for our home made 20 contacts chip carrier is attached in such a way that it maintains the bottom copper plate of the chip carrier in thermal contact with the cold finger. The electrical connection between the measurement devices and the chip carrier are then made by connecting the contact pins of this receptacle to a plug on the side of the cryostat vessel, far away from the cold area, with the help of Kapton capped copper wires. As a result, the contact pins of the chip carrier are thermally coupled to the outside. In order to prevent a too high incoming heat load

on the contacts, wires with a diameter of 0.2mm are used. Furthermore, the 20 wires are wound around the first and second cooling stage of the cryostat. In this fashion the heat flow between the chip carrier and the outside environment can be almost completely removed. The temperature of the cryostat can be set to any desired value between 10K and 350K by mean of a Lakeshore temperature controller contacted to a resistive heater and a silicon diode placed directly inside the cold finger. A Keithley digital sourcemeter (DSM) is used for four-point electrical measurements and a Keithley electrometer is used for the measurement of the collector current of our MTT. Finally, rotating electromagnets provide an in-plane magnetic field of up to 1500Oe at the sample's site.

Chapter 4

Magnetic properties

4.1 Room temperature properties

In soft spin valves consisting of polycrystalline ferromagnetic layers, the desired difference in coercive fields is obtained through the choice of material. If no long range structural order exists, the influence of the magnetocrystalline anisotropy is usually fairly low and the magnetic behavior of the spin valve is expected to remain more or less constant regardless of the direction of the in plane external magnetic field. In contrast, our system consists of an epitaxial spin valve where the magnetocrystalline anisotropy is strong. This means that the shape of the hysteresis curve will strongly depend on the orientation of the external magnetic field. We will thus describe here the magnetic properties of our samples and the way they are influenced by their epitaxial structure. The magnetic properties of our epitaxial spin valve will depend on the coercive fields and the anisotropy constants both of which can be modified through structural (thickness, defect concentration, substrate induced strains) and chemical (composition, possible reaction with adjacent materials) variations.

As an example, the growth of bcc-FeCo on GaAs leads to an anisotropic behavior different than that of its bulk form. As the bcc-FeCo has a cubic structure in the (001) plane, the magnetic anisotropy has a fourfold symmetry. However, the contact of the thin FeCo layer with the GaAs(001) surface leads to an additional uniaxial interface anisotropy [66], similarly to what has been observed for bcc-Fe films on GaAs(001)[67]. This effect is not present when bcc-FeCo(001) is grown on fcc-Au(001). As a result, the anisotropies of the two ferromagnetic layers of our spin valve will be different. Figure 4.1 presents longitudinal MOKE measurements of the magnetization loops of a sample containing a single FeCo layer grown on GaAs(001) (a, c and e) and a full MTT (b, d and f).

For the bottom FeCo layer, the [110] axis is the magnetic easy axis for both the bulk fourfold and the uniaxial interface anisotropies[68][69]. Assuming for now that the top FeCo layer (30ML) has only a fourfold component to its anisotropy, the [110] corresponds as well to the magnetic easy axis. When the field is applied along this axis, for fields higher than 75Oe, the magnetization of both layers is saturated.

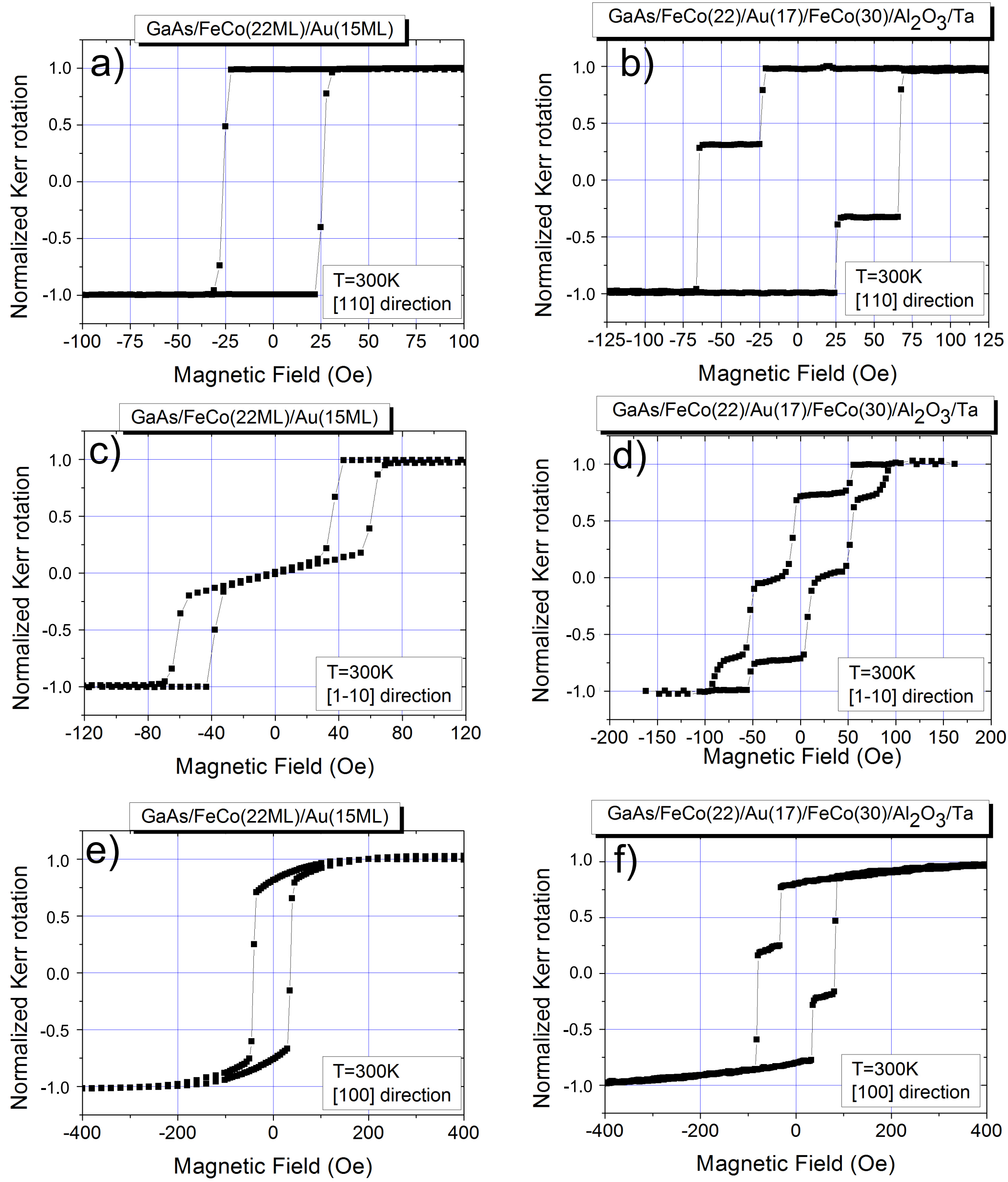

Figure 4.1: Magnetization loops at room temperature of two samples; one containing a single FeCo layer grown on GaAs(001) (a), (c), (e) and a full spin valve (b),(d) and (f)

As the field decreases, the magnetization of the bottom FeCo layer will first switch at about -25Oe. The sharp square switching is characteristic of magnetic switching through domain nucleation and wall motion. When the magnitude of the field is further increased toward negative values, the top FeCo layer will switch at about 70Oe. The difference in coercive field for the two FeCo layers is a direct result of their interactions with the different underlayers they are grown on.

The [1-10] axis corresponds to the magnetic easy axis of the fourfold component and to the hard axis of the uniaxial component of the bottom FeCo layer. For

this reason, this axis is sometimes called middle-hard axis for layers presenting both anisotropy components. This situation leads to a step-like hysteresis loop, as can be observed in figure 4.1 c). Let us first describe the magnetization behavior along the [1-10] axis taking place for the sample having a single FeCo layer. When the field reaches about 40 Oe, coming from a saturated state at positive fields, the magnetization first switches from the [1-10] axis to a direction close to the [110] easy axis by domain nucleation and wall motion. When the field is further reduced, a coherent rotation of the magnetization takes place as can be seen in the central linear part of the magnetization loop. Eventually, for negative fields, the magnetization will switch and align itself with the [-110] direction creating the second jump in the loop. The MOKE measurement (d) of the whole MTT presents with a complex magnetization process which is the superimposition of the two FM layers. From the comparison of (c) and (d), we can deduce that the top FeCo layer also has a step magnetization loop indicating that beside the fourfold anisotropy for which the [1-10] is the easy axis, some uniaxial anisotropy is still present. This result is in agreement with other studies [20].

Finally, MOKE loops were measured with the field applied and swept along the [100] direction. This direction corresponds to the hard axis of the fourfold anisotropy of both the bottom and top FeCo layers and to an intermediate axis for the uniaxial anisotropy. Due to the uniaxial anisotropy, the magnetization reversal of both layers does not take place solely by coherent rotation. At first, the magnetization of both layers rotate when the field's magnitude decreases from a saturated state. Eventually, the magnetization reaches a direction where the energy cost is lower for domain nucleation and wall motion leading to the jumps in the magnetization loops (e) and (f). The exact magnetic field values of those jumps (or magnetization direction) depends on the relative ratio of the uniaxial and fourfold anisotropy constant.

The previous description of the magnetic properties allowed us to gain some insight into the fundamental magnetic properties of the epitaxial spin valves by comparing the loops of single and double layer systems. In MTTs, the collector current reaches a minimum when the layer's magnetizations are fully antiparallel. MOKE measurements allow the determination of the magnetization component along the direction of the magnetic field. the GMR effect on the contrary is directly proportional to the cosine of the angle between the magnetizations of the two FM layers. In order to access the information directly relevant to the study of the transport in MTT, we therefore pursued by measuring the in plane GMR. Figure 4.2 presents in plane GMR measurements along the easy, middle hard and hard axis at room temperature together with the results of numerical simulations of the magnetization reversal calculated with a numerical model based on the Stoner Wolfrath model programmed by Dr. Tobias Martin. The simulation uses as input the values of the anisotropy constants, the thicknesses and the wall energies. The values used here are summarized in table 4.1.

Along the easy [110] axis, a square GMR loop is obtained resulting from the do-

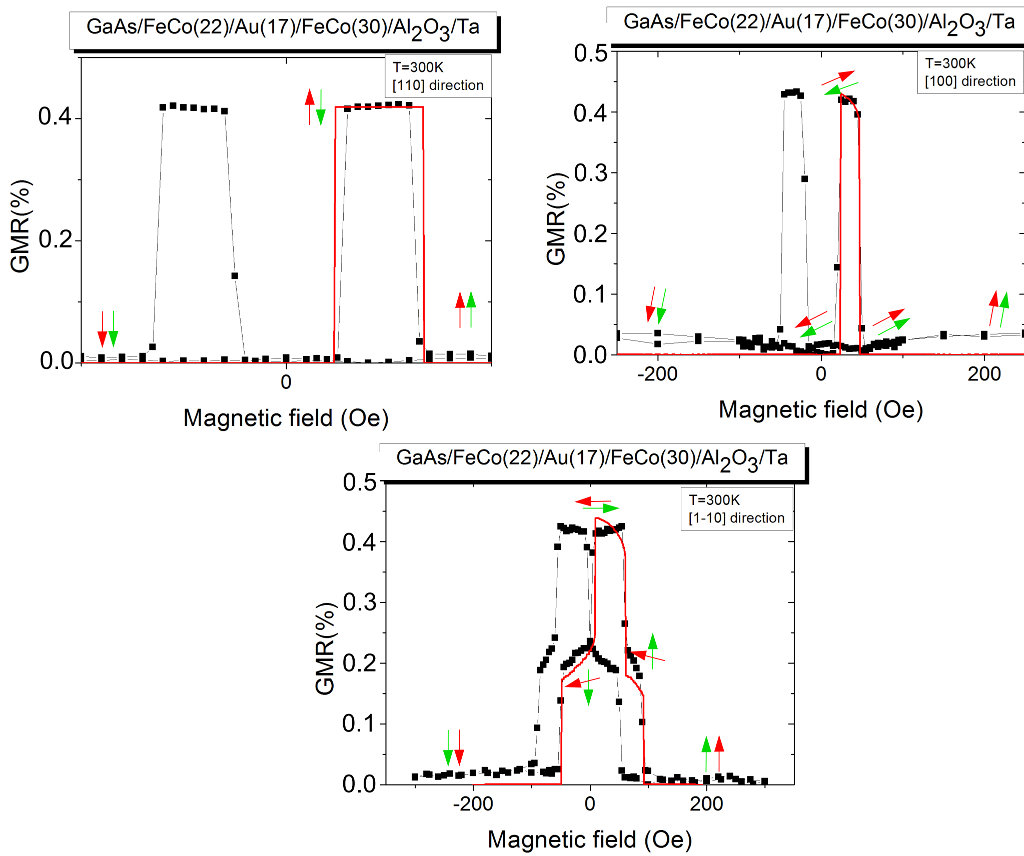

Figure 4.2: In plane GMR at room temperature along the [110], [1-10] and [100] axis. The results of simulation calculated with the program mmloop developed by Dr. Tobias Martin are plotted as red lines. The red arrow represents the bottom FeCo layer and the green the top one. The vertical direction is always taken as a reference direction aligned with the external magnetic field.

	$K_u(J.m^{-3})$	$K_1(J.m^{-3})$	$t(ML)$
bottom layer	10500	-14200	22
top layer	6000	-7400	30

Table 4.1: values used in the simulation of the magnetization reversal

main wall nucleation and motion like switching. The FM layers are in this case either parallel or antiparallel, leading to a straightforward interpretation of the magnetic behavior.

When the field is along the [100] axis, we can see that during the coherent rotations at forward and reverse fields, the magnetizations remain parallel. The different fields at which the two layers switch however induce an angle between their magnetizations in the region where only one of the layer has switched. From the value of the GMR in this region which is the same as the one along the [110] axis, we can deduce that both layers are antiparallel, which is confirmed by the simulations results.

Finally along the [1-10] axis, we can see that the simulations agree well with the

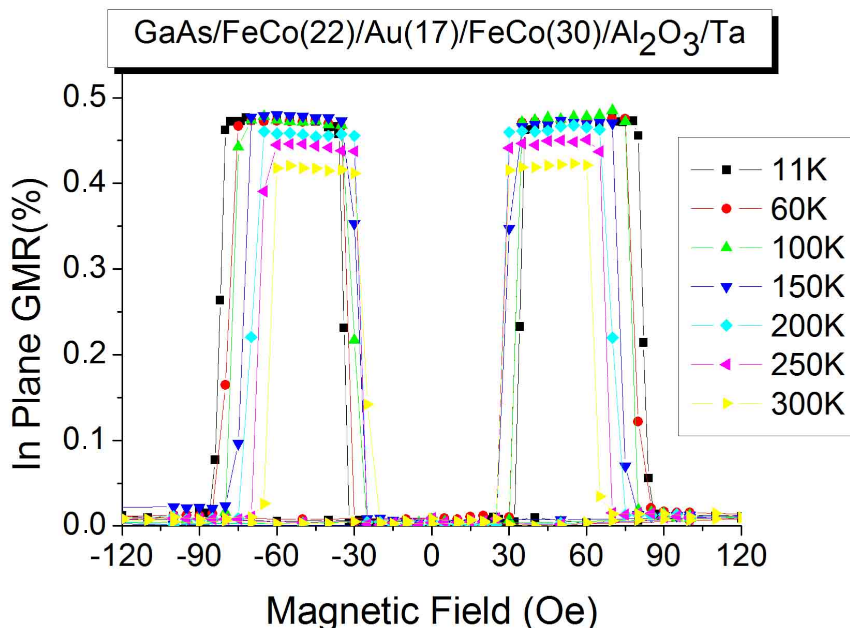

Figure 4.3: Temperature dependence of the GMR measured along the [110] direction

measured data which can be explained in the following way: coming from saturation at negative fields, at about 50Oe the bottom layer's magnetization first aligns itself along a direction close to the [110] direction by domain wall motion, creating a first jump in the loop. As the field is increased, a coherent rotation of the bottom magnetization takes place. At slightly positive fields, the magnetization of the second layer jumps to an angle about 90° away from the field direction while the bottom magnetization still rotates thus creating an almost antiparallel state, where the GMR reaches a maximum. At higher positive fields, around 30Oe, the top magnetization realign itself with the field, creating the third jump in loop. Finally at about 100Oe, the bottom layer undergoes a reorientation of its magnetization parallel to the applied field, accounting for the fourth jump.

4.2 Temperature dependence

The above discussion concerned only the magnetic behavior of MTTs at room temperature. However, all the collector current measurements contained in this thesis actually took place at cryogenic temperatures and a thorough description of the magnetic properties below room temperatures is necessary. We therefore investigated the magnetic behavior of our MTT down to 10K. Although there was a possibility to measure the temperature dependence of the magnetization by MOKE, we here only measured the in plane GMR. This method indeed presented several advantages over the MOKE measurements: First it was possible to conduct the GMR measurement in the same setup as the electrical characterization of the MTT itself. Furthermore, the GMR gives qualitatively the same magnetic response to an applied field as a

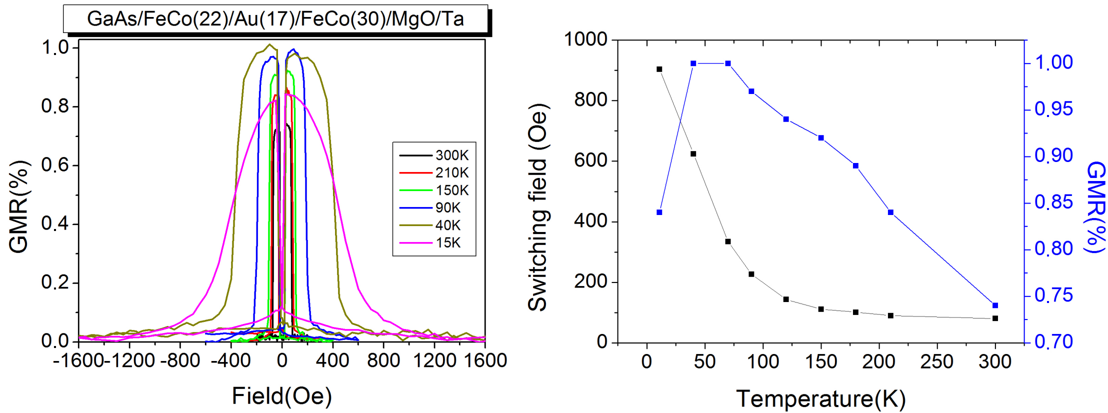

Figure 4.4: temperature dependence of the in plane GMR for a sample with rough interfaces (left). temperature evolution of the maximum GMR and the switching field of the top FeCo layer(right)

MTT. Finally, this allowed us to investigate directly the patterned MTTs whereas extended films are usually more suited for MOKE measurements. Since all MCR measurements presented in this thesis have been measured with the magnetic field aligned along the easy [110] axis, we will focus our study on GMR loops along this axis.

Figure 4.3 shows such a measurement for temperatures ranging from 300K to 10K. We can see that as the temperature drops, the coercive field of both layers increases as a result of the reduced thermal energy. The switching remains sharp over the whole temperature range, thus corresponding to an ideal case where the magnetizations can be kept antiparallel over the whole temperature range. The increase of the GMR ratio with decreasing temperature is a well known phenomenon ascribed to an increase of spin dependent inelastic scattering by magnons and spin independent elastic scattering by phonons with increasing temperature[70].

The ideal case presented above could however not be obtained in a fully reproducible manner. The magnetic properties were indeed found to vary strongly depending on the structural quality of the sample. For instance, the GMR curves presented in figure 4.4 measured on another sample exhibited a completely different temperature behavior. This sample was slightly rougher due to a decreased quality of the substrate preparation. For temperatures above 100K a wide field range does offer an antiparallel state. The increase of the switching field of the top FeCo layer is however much stronger than for the previous sample. This effect is probably defect related: the demagnetization field created by non magnetic defects create a potential barrier that hinders the propagation of domain walls. As the temperature drops, the thermal energy available is reduced and the domain walls cannot overcome this barrier without the magnetic field to be increased. When the temperature is further reduced to below 90K the GMR first reaches a maximum and then decreases. This effect can be ascribed to a reduction of the maximum angle between the magnetization of the two FM layers as can be seen on the GMR loops, especially at 15K. This

seems to indicate that some FM coupling exists between the two FM layers. Furthermore, the exact behavior of the magnetizations at low temperature was found to vary strongly between samples with nominally the same spin valve thicknesses. This non reproducibility is consistent with the difficulty mentioned in section (3.2.1) to reproducibly control the roughness of the substrates. A possible explanation is that some correlated roughness over the sample's thickness leads to some orange peel coupling. The magnitude of this coupling depends quadratically on the saturation magnetization, which increases as the temperature drops. Consequently, the effect of this coupling will be stronger at lower temperatures.

Chapter 5

Electrical properties

The proper operation of MTTs relies on the fact that all of its building blocks have simultaneously the required characteristics. The last chapter was concerned with the description of the magnetic properties of the epitaxial spin valve which will define the qualitative behavior of the electrical response of the MTTs to an applied magnetic field. This response can however be observed only if the emission and the collection of hot electrons takes place in such a way that the collector current is measurable, the lower limit being set by the accuracy of the electronics used to measure the collector current ($\approx 100fA$). The purpose of this chapter is to present the electrical properties of the tunnel emitter and Schottky collector that were used in this work and to assess their quality based on the impact they will have on the operational range, signal to noise ratio, reproducibility and long-life cycle of the MTTs.

5.1 Schottky diodes

In order to characterize the electrical properties of the Schottky barriers, a four point method was used, were two contacts were made to the base and two at the ohmic contact at the back of the substrate. By measuring the I(V) curves, important informations on the Schottky barrier height and the dominating transport mechanism over the barrier can be obtained. For voltages V such that $eV > 3kT$, the equation (2.2) can be approximated to

$$J = A^{*}T^{2} \exp\left[-\frac{q\Phi_{B}}{kT}\right] \exp\left[\frac{qV}{nkT}\right] \quad (5.1)$$

This equation can be used to fit the experimental I(V) curves in order to extract the value of the barrier height Φ_B and of the ideality factor n. When plotted on a semilogarithmic scale, the I(V) curve in the forward direction should give a straight line. The left panel of figure 5.1 shows the I(V) curve measured at room temperature for a sample prepared by annealing and sputtering as described in section (3.2.1).

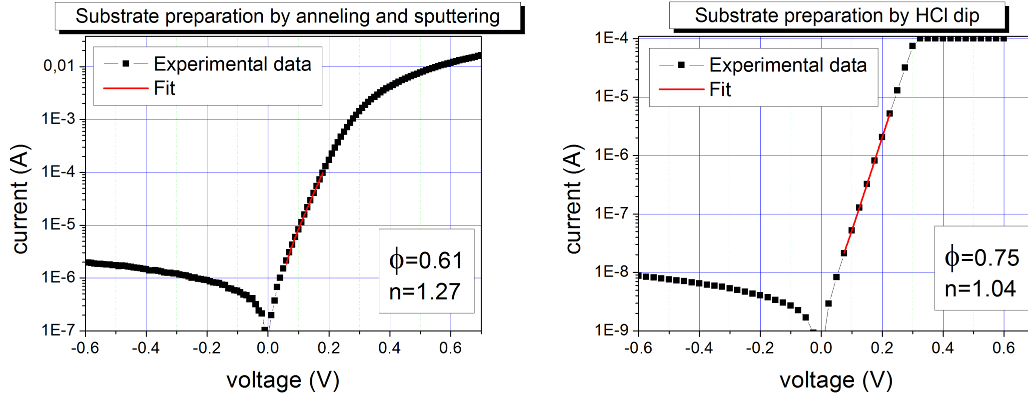

Figure 5.1: I(V) characteristics of FeCo/GaAs Schottky diodes were the substrate was prepared by annealing and sputtering (left) and by a HCl etch (right)

It can be seen that for voltages higher than ≈0.25V, the curve departs strongly from the expected behavior. This effect is due to the voltage independent series resistance of the Schottky diode, constituted by the resistance of the metallic layer, the semiconductor layer and the Ohmic contact (which is sample dependent due to the variable amount of InGa eutectic applied on the substrate's reverse side). We therefore restrict our fitting area to the portion of the curve where the current voltage characteristic corresponds to the thermionic regime. We obtain a barrier height $\Phi_B = 0.61 \pm 0.01$ and an ideality factor $n = 1.27 \pm 0.02$. Those results are in very good agreement both with the results obtained by Hagler[50] and Spitzer[21] on similar samples. The right panel of figure 5.1 shows the characteristic of a sample whose substrate comes from the same wafer as the previous sample but which has been prepared by an HCl etch. It is immediately visible that the current is several orders of magnitude lower yielding a barrier height if 0.75eV and an ideality factor of 1.04. As a result of the enhanced barrier height, the reverse current for the HCl sample is more than two orders of magnitude lower than the one prepared by annealing and sputtering. This strong discrepancy is most probably related to the chemical structure of the GaAs surface. GaAs(001) surfaces prepared by annealing and sputtering are known to produce Ga rich surfaces whereas those prepared by an HCl etch are As rich[71][72][73]. The bonds created directly at the interface are thus different and no common behavior should be expected. Another cause of difference could be the presence of an oxide layer at the MS interface of the HCl etched sample. However, Spitzer measured the barrier height and ideality factor on samples with GaAs(001) substrates which were prepared by simple annealing at temperature ranging from $200°C$ to $550°C$[74]. It was found that both remain more or less constant and close to the values obtained for the sample annealed at $550°C$, where the whole oxide layer had desorbed, thus indicating that an oxide layer wouldn't create such a drastic difference as the one observed here. It is interesting to note that the values of the Schottky barrier height of the HCl etched sample is relatively close to the one published by Van Dijken ($\Phi_B = 0.78eV$) for polycrystalline

samples (see for instance[75]). The lack of published experimental details regarding his substrate structure however prevents any further comparison.

In a MTT, the Schottky barrier is actually completely unbiased and its electrical properties influence the overall transport in two separate ways:

1. The height of the Schottky barrier defines the minimum electron energy necessary for collection of hot electrons
2. Due to deviations from the thermionic regime (mostly localized reductions of the Schottky barrier height at defects sites or thermally assisted field emission), some of the injected electrons that have been thermalized in the spin valve will still be able to cross over to the semiconductor. Those electrons will create a thermal component of the collector current independent on the magnetic field that can be, depending on the temperature, orders of magnitude higher than the *"real"* collector current and thus prevent its measurement.

Whereas the Schottky barrier height (SBH) is, as has been seen mostly material related, and cannot be changed without modifying the substrate and thus influencing the whole MTT structure, the thermal component of the collector current is related to the SBH homogeneity and to the doping and efforts can be undertaken to optimize the MTTs concerning both aspects.

5.1.1 Influence of the patterning method

In epitaxial Schottky diodes, inhomogeneous SBH distribution are usually not expected. However, patterning by means of optical lithography for the definition of the Schottky barrier involves a dry etching step which is believed to be responsible for the creation of defects at the edges of the structure which have a lower Schottky barrier height and thus a higher transmission of thermal electrons. It has been seen that through a wet etching repair step, the I(V) characteristics of dry-etched Schottky barriers can be greatly improved. Spitzer found [74] that in the case of Fe and FeCo on GaAs, a 70 sec citric acid bath would render the low forward bias part of the I(V) curve more linear and reduce the current in the reverse direction by several orders of magnitude. No further improvement could be seen when the wet chemical etching step was prolongated beyond this point, indicating that almost all defects had been removed. The shadow mask technique on the other hand, completely prevents the creation of such defects.

Figure 5.2 shows characteristics of FeCo/GaAs(001) Schottky diodes made by shadow mask (top panel) and by optical lithography, dry etching and a subsequent wet chemical repair step. In both cases, the dopant concentration is in the low 10^{16} cm^{-3} range. Since the area of the diodes are different, the current density J is preferred to the current. We will first focus our attention on the negative voltage part of both curves. According to the thermionic emission theory, J should

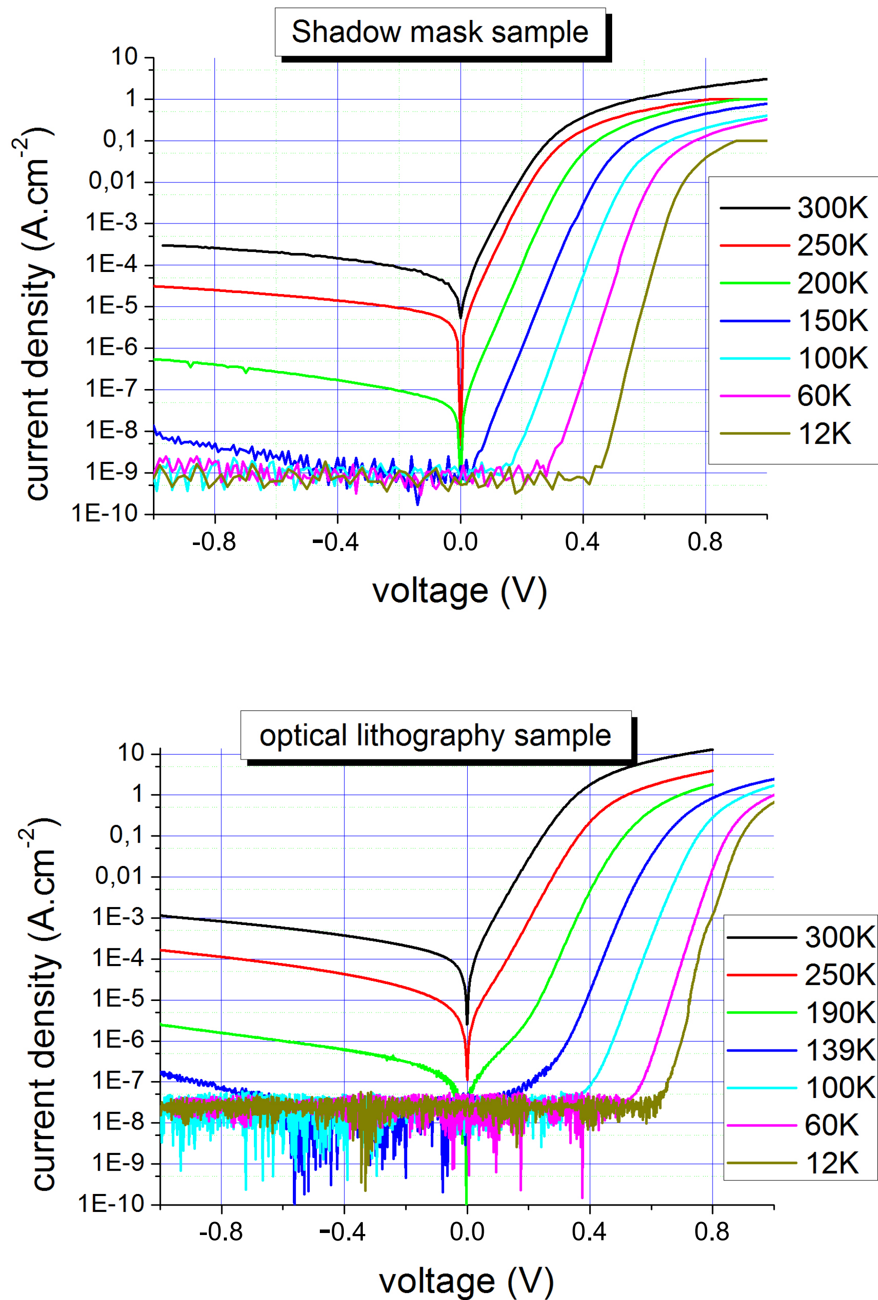

Figure 5.2: Temperature dependent J(V) curves for FeCo/GaAs(001) Schottky diodes structured by in situ shadow mask (top panel) and optical lithography

saturate in the reverse direction. However, experimentally this saturation is never observed and this departure from theory is inferred to the voltage dependency of the Schottky barrier height and width. Possible reasons for this are the image force, thermionic field emission (TFE) at the edges where the field is enhanced or inhomogeneous SBH distribution [76]. In our case, the magnitude of the reverse current is too high to be explained solely by the effect of the image force an its explanation has to be found in edge related effects and barrier inhomogeneity. One

of the recurrent argument used to explain the non saturation of the reverse current is a field enhancement at the edges leading to an increase of thermally assisted field emission at the edges. Since this effect takes place exclusively at the edges, we can use the fact that the Schottky diodes prepared by the two different methods have different geometries to determine whether edge enhanced TFE is the sole mechanism leading to the observed reverse current. The part of the current density due to edge enhanced TFE should scale with the perimeter to area ratio R_{PA}. For the shadow mask diodes $R_{\mathrm{PA}}^{\mathrm{mask}} = 39.4$ and for the diodes patterned by optical lithography $R_{\mathrm{PA}}^{\mathrm{opt}} = 150$. If the reverse current is solely due to edge enhanced TFE, it should thus be $R_{\mathrm{PS}}^{\mathrm{opt}}/R_{\mathrm{PS}}^{\mathrm{mask}} = 3,79$ higher for the sample patterned by optical lithography. Table 5.1 summarizes the ratios $\alpha = J_{\mathrm{opt}}(-1V)/J_{\mathrm{mask}}(-1V)$ for different temperatures. At room temperature, the current density ratio α is indeed close to 3.79. However, as the temperature drops, α tends to increase and at 150K, the current density for the sample patterned by optical lithography is already more than 10 times higher than for the shadow mask sample. Since the dopant concentration is the same for both samples, no temperature dependence of α would be expected in the case where the reverse current is due to TFE at the edges, thus implying that another transport mechanism influences the reverse bias characteristic, at least of the sample patterned by optical lithography, if not both samples. The relative influence of this mechanism gets stronger as the temperature drops.

T[K]	α
300	3.37
250	5.24
200	4.87
150	12.89

Table 5.1

If we now observe the forward characteristics, we can see that for the sample patterned by lithography, the low voltage part of the I(V) curves is not a straight line for temperatures below 250K. Those non-linearities are mostly visible for the temperatures 200 and 150K. They probably exist as well at lower temperatures but at current densities below the detection limit of our setup. This departure from pure thermionic emission is not visible on the shadow mask sample. Tung [77]calculated that such "soft" forward characteristics can originate from inhomogeneous SBH distribution. A small low SBH area surrounded by a high SBH area will modify the potential at the MS interface. It was shown that if the low SBH area is small compared to the depletion layer's width W, it will be pinched off by the surrounding high SBH region. The amount by which the low SBH channel is pinched off increases with the applied forward voltage and with the temperature. For this reason, behavior departing from the pure thermionic emission are expected to be visible for low voltages and temperatures. Furthermore, it was demonstrated that an isolated low SBH area acts more effectively on the overall current voltage curves if it is placed at the periphery of the diode structure, where the surrounding high SBH region cannot be approximated by an infinitely wide area[78]. A coherent explanation that would account for the differences between both types of diodes could therefore be the existence of some remaining small areas with low SBHs (defects) at the diode edges in the sample patterned by optical lithography that would tend to slightly

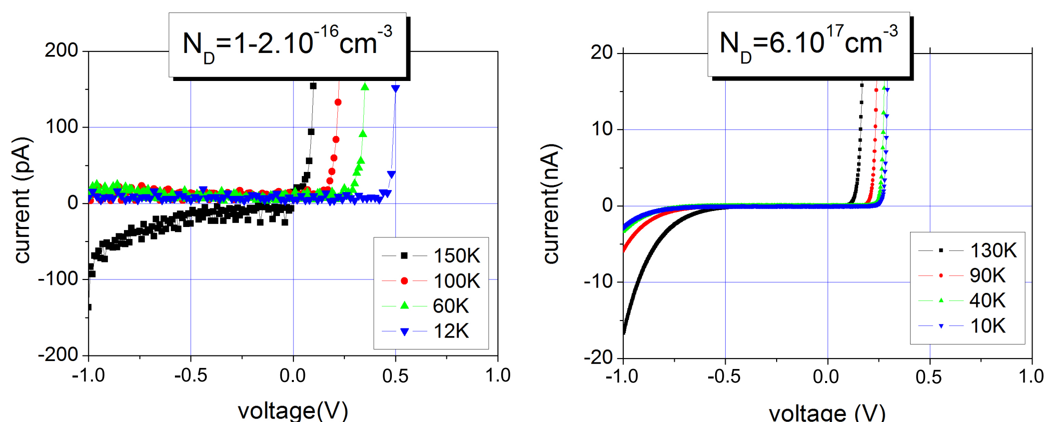

Figure 5.3: I(V) characteristics for different temperatures for two FeCo/GaAs diodes using two different dopant concentrations

increase the reverse current and modify the forward characteristic's shape for low temperatures and voltages. An exact comparison with the theory developed by Tung is however not directly accessible since the quantitative behavior of Schottky diodes including inhomogeneities varies strongly with the defects dimensions and density.

5.1.2 Influence of the donor concentration

Most works of MTTs on GaAs report the use of GaAs substrate with a dopant concentration of $1 \times 10^{17} cm^{-3}$. This dopant concentration is convenient as it allows the easy creation of a low resistance ohmic contact with the substrate's reverse side while still maintaining the electronic transport in the thermionic emission regime. It was already shown[21] that the use of a substrate with a doping concentration of $1-4\times10^{16}\mathrm{cm}^{-3}$ strongly reduced the amount of thermally excited electrons crossing the Schottky barrier. However, this study compared two samples made by optical lithography without wet chemical repair step. As has been seen in the previous section, edge defects lead to singular temperature dependent behaviors of the I(V) characteristics and there is no a priori indication that the increase of the thermal current with the doping concentration will be of the same order of magnitude for samples made by shadow masks.

The curves presented in figure 5.3 depict I(V) characteristics for two FeCo/GaAs(001) diodes with dopant concentration $N_\mathrm{D} = 1 - 2 \times 10^{16} cm^{-3}$ and $N_\mathrm{D} = 7 \times 10^{17} cm^{-3}$. As in [21], we find that the reverse current is markedly stronger for higher doping (scale in pA in fig. 5.3 left and in nA in fig. 5.3 right) and that the forward current varies faster with the temperature in the case of higher doping. The lower reverse current magnitude and higher temperature dependence for lower dopant concentration is to be directly related to the influence of the dopant concentration on the barrier width and thus on the contribution of the tunneling channel to the overall current. Spitzer found a ratio of 50 between the current in the reverse direction for high and low doping at a voltage of 0.5V and a temperature of

150K. In the case of shadow mask samples, we can extract from the I(V) curves that this ratio is already higher than 200 when we compare the current for the highly doped sample at 130K with the current for the low doped one at 150K. Considering that the reverse current is on average already about one order of magnitude lower for the high doped sample made by shadow masks than the high doped sample made by optical lithography, this fact clearly indicates that the defects damp the temperature reduction of the reverse current when N_D is reduced.

5.1.3 Summary

It was shown that the preparation of the GaAs substrates influences drastically the electrical properties of FeCo/GaAs(001) Schottky diodes. The SBH was found to be 0.61eV for substrates prepared by annealing and sputtering and 0.75eV for those prepared by an HCl etch. The discrepancy is ascribed to the different termination of the GaAs surface. The As terminated surface have a higher Schottky barrier and lower ideality factor and thus a reduced influence of thermal electrons on the measured collector current in a MTT. The HCl preparation methods is therefore to this respect more suited than the sputtering-annealing method. The comparison between the optical lithography and the shadow masks structuring methods, allowed us to demonstrate that optical lithography-induced edge defects can be partially but not completely removed. Those low SBH defects are expected to increase the thermal leakage current over the barrier and the shadow mask method therefore is more suited for observing the magnetic response of MTTs at room temperature.

5.2 Tunnel emitter barrier

As described in section (3.2.4), several approaches have been used in this work to fabricate the tunnel emitter. We will first present their basic electrical properties and comment on their potential use for the fabrication of MTTs with the shadow mask technique.

5.2.1 Aluminum oxide:natural oxidation

Using a four point measurement technique, the I(V) curves of naturally oxidized aluminum oxide tunnel barriers were measured both at room temperature and at 12K. As described in section (3.2.4), the thickness of the barrier was varied by changing the number of growth oxidation cycles. With four steps (3.1nm of oxide), an Ohmic relation between voltage and current was always observed. With increased thicknesses, tunneling-like I(V) curves could be obtained. Figure 5.4 depicts the measurement results of a barrier made using six steps (4.6nm of oxide). We can see that both at 300K and 12K the curves can be fitted by the Simmons model. However, it is found that $\varphi(300K) = 1.02\ eV$ whereas $\varphi(12K) = 1.60\ eV$. The pub-

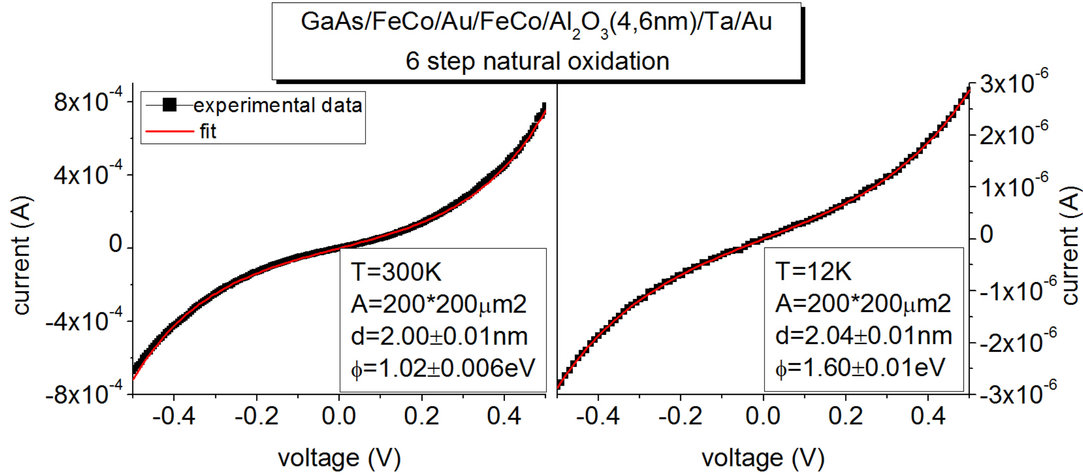

Figure 5.4: I(V) curves of a 4.6nm thick tunnel barrier oxidized by natural oxidation at 300K and 12K. The values of the barrier thickness d and height ϕ are extracted from a fit using the Simmons model

lished values of barrier heights of amorphous aluminum oxide are usually comprised between 1.6 eV and 1.8 eV. In principle, the barrier height is mostly temperature independent. The observed strong variation of φ with the temperature in our case could be explained by taking into account electron hopping in the tunnel barrier. Hopping effectively divides the tunneling through the barrier into several tunneling steps between localized metallic states within the barrier. Those localized states are usually impurities or unoxidized atoms. The influence of hopping is strongly temperature dependent and increases with the temperature. Furthermore, the hopping depends to a second order on the applied voltage thus influencing the parameters extracted from the Simmons fit[79]. It is thus most likely that in the case presented here, electron hopping contributes to the tunneling current at room temperature. As the temperature is reduced, the contribution of hopping is reduced down to a point where it becomes negligible. At this point, the extracted barrier height corresponds to the expected one. Another surprising aspect is the low mean barrier thickness extracted from the fit as compared to the thickness deposited. This effect is probably due to strong thickness variations of the insulator as explained in section (2.1). For barriers made with this method, breakdown voltage between 0.5V and 0.9V were measured, rendering impossible their use as emitter for a MTT. Both extrinsic and intrinsic-like breakdowns were observed. Interestingly, the breakdown mechanism was always constant within one sample (4 MTTs) hinting at an influence of the substrate preparation on the tunnel barrier properties.

5.2.2 Aluminum oxide:plasma oxidation

The I(V) curves of plasma oxidized aluminum oxide barriers are presented in figure 5.5. As in the case of naturally oxidized aluminum oxide barriers, those curves can

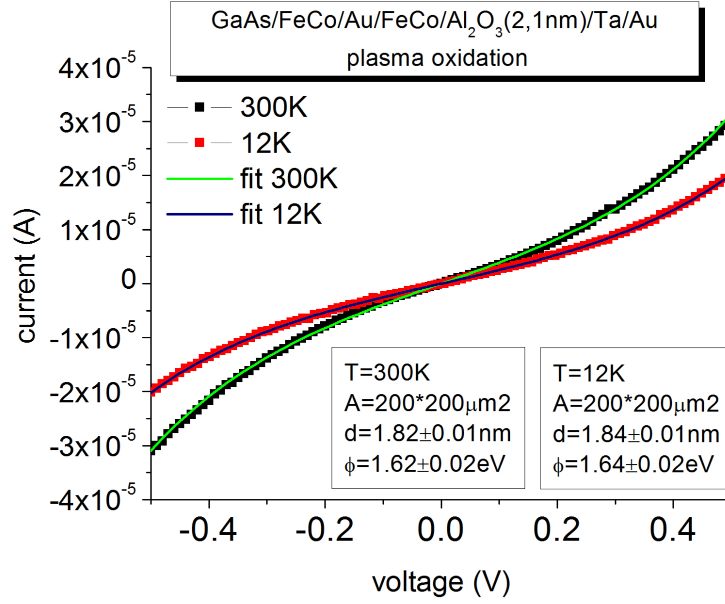

Figure 5.5: I(V) curve of plasma oxidized aluminum oxide tunnel barrier measured at 300K and 12K. The values of the barrier thickness d and height ϕ are extracted from a fit using the Simmons model

be well fitted by the Simmons model. However, in the case of plasma oxidized barriers, no variation of the tunnel barrier parameters with the temperature is observed indicating that the barrier chemical homogeneity is higher since no electron hopping takes place. Furthermore, the extracted thickness is much closer to the deposited oxide thickness. This effect was found to be reproducible and cannot therefore be attributed only to a punctual improvement of the substrate quality. It seems that the growth of thicker aluminum layers tends to provide smoother films. Another difference with naturally oxidized barriers lies in the value of the breakdown voltages. We found that for plasma oxidized barriers, V_{break} is comprised between 1.2V and 1.8V. Those values are substantially higher than those reported in the previous subsection and would allow the operation of a MTT within the range where a collector current is observable. For those barriers as well, both extrinsic and intrinsic breakdowns were observed, and the nature of the breakdown mechanism was always the same within one sample. The higher breakdown voltage values together with the more accurate determination of the mean barrier thickness indicate that the barrier roughness is lower for plasma oxidized barriers. The exact underlying reason is not known at this point and further investigations would be beyond the scope of this thesis.

5.2.3 Magnesium oxide

Finally, measurements and fits of 2.8nm MgO barriers are presented in figure 5.6. The lower quality of the fit is due to a slightly more pronounced asymmetry of the interfaces barrier height related to the polycrystalline structure of MgO. Again,

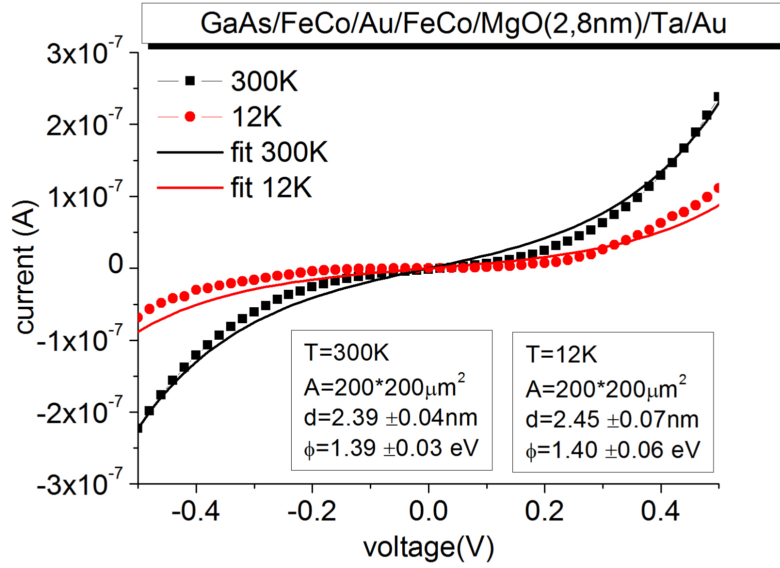

Figure 5.6: I(V) curve of a magnesium oxide tunnel barrier measured at 300K and 12K. The values of the barrier thickness d and height ϕ are extracted from a fit using the Simmons model

no temperature dependence of the barrier parameters are observed. The extracted barrier height of 1.4eV is lower than the theoretical value[80]. However, it has been shown that the height of MgO barriers as extracted from Simmons-like models are usually lower due to the presence of oxygen vacancies in the insulator[81], which is consistent with the fact that our barriers were deposited using only Argon as the sputtering gas. The breakdown voltages for MgO barriers were comprised between 1.6V and 2.7V with the presence of both extrinsic and intrinsic breakdown.

5.2.4 Applicability for MTT purposes

Out of the three types of barriers described previously, only plasma oxidized aluminum oxide and magnesium oxide barriers offer the desired characteristics for being used in a MTT. Indeed, the breakdown voltage for naturally oxidized aluminum oxide barriers was equal or slightly above the SBH thus rendering any collector current measurement almost impossible. The lower breakdown voltage can be ascribed to a stronger interface roughness of the barrier and the existence of localized conducting states in the oxide. Out of the two remaining fabrication methods, MgO was usually preferred due to the lower barrier height and the bypassing of the time consuming oxidation process. On a general basis, a trade-off had to be found between high breakdown voltage (thick barriers) and low resistance area product (thin barriers). The lower barrier height of MgO is thus technologically most interesting since it allows the deposition of thicker barrier while maintaining the resistance area small enough to be able to measure a collector current. This is highly desired since thicker barriers have a reduced probability of pinholes and a higher dielectric breakdown

voltage,

The extracted barrier height and thicknesses together with the breakdown voltages were found to be constant within one sample. On the other hand, variations in the resistance area product of more than two orders of magnitude were found between samples having the same barrier type and deposited thicknesses and was related to variations in the extracted mean barrier thickness. Those effects are related to the difficulty to reproducibly control the roughness of our samples, especially of the substrate. Using the model developed by Miller [28] and using the extracted barrier height and thickness of our MgO barriers, we calculated that a gaussian thickness distribution with a standard deviation of 3Å would already multiply the current measured at 1V by a factor of about 175 as compared to a perfectly homogeneous barrier.

Chapter 6

Spin dependent transport in the magnetic tunnel transistor

6.1 Requirements for collector current measurement

In this chapter, the results of electrical measurements made on MTTs with epitaxial spin valve base made by the shadow mask technique will be presented. Those measurement focus on the response of the collector current to an external in plane magnetic field at a given temperature and emitter voltage. The measurements were conducted in the setup described in section (3.3) and a schematic of the contact configuration on the sample can be seen in figure 6.1. Typically, the digital sourcemeter was used to bias the emitter barrier in a four point geometry where the emitter contact was put at a given negative voltage while the base contacts were grounded. The electrometer was connected to the collector contact in order to measure the current flow between this contact and the ground. In this configuration, the Schottky barrier remained completely unbiased so that only hot electrons could overcome it. The order of magnitude of the collector current was usually in the pA region if not lower and extra care had to be taken to prevent the apparition of ground loops that would cloud the real collector current. This was achieved by using only one common ground for the whole apparatus and measurement devices. Furthermore, no stray resistance paths should exist between the electrometer and the surrounding voltages. Special attention was thus required to ensure that the signal lines had no contact between themselves or to the chassis of the apparatus. The Kapton insulation of the 0.2 mm diameter Cu wires used for the signal lines appeared however to be quite fragile and regular inspection and replacement of those lines were necessary. Finally, in order to avoid triboelectric effects, a special Keithley low noise cable was used between the electrometer and the external plug of the cryostat.

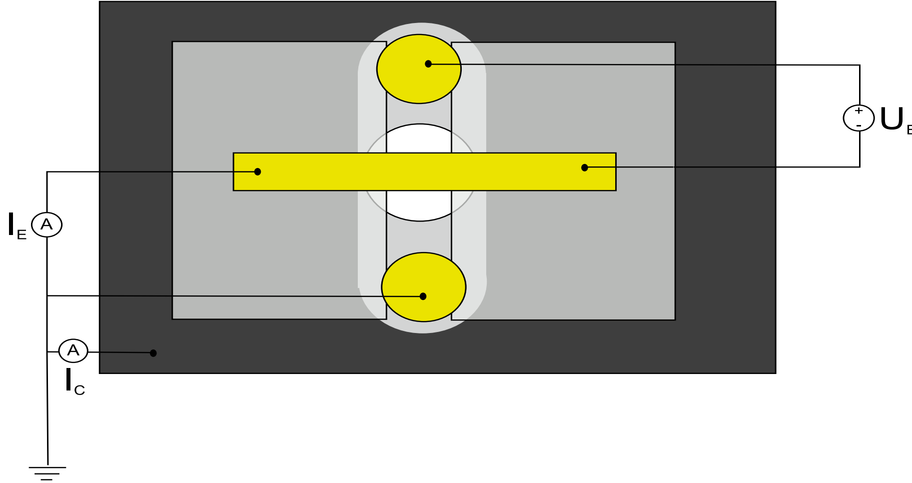

Figure 6.1: electrical connections in a MTT

6.2 Magneto-current ratio measurements

In the course of this work, two types of samples have been measured. the main difference between them lied in the method use to prepare the substrate. The MTT structures of two characteristic samples are presented in table 6.1. The HCl sample is referred to as sample 1 and the sputtering-annealing as sample 2. Figure 6.2 shows

	sample 1	sample 2
preparation method	HCl	sputtering-annealing
t_{FeCo1}(nm)	3	3.4
t_{Au}(nm)	3.4	3.9
t_{FeCo1}(nm)	3.9	3.4
$t_{barrier}$(nm)	2.2	3
barrier material	Al_2O_3 plasma oxidized	MgO

Table 6.1: Layer description of two characteristic MTT

the magnetic field dependence of the collector current measurements for sample 1 measured with the magnetic field applied along the [110] axis. The loops were the average of 6 loops ($V_{bias} = 0.9V$ and $V_{bias} = 1.1V$) and 3 times ($V_{bias} = 1.0V$). It was observed that the shape was only partially reproducible from one loop to the other. In-plane GMR loops measured on this sample at room temperature were characterized by two sharp switching at fields of 20Oe and 55Oe which are considerably lower than the switching fields measured here. As shown in section (4.2), the qualitative behavior of the magnetic switching in our epitaxial spin valves depends strongly on the roughness of the sample. For smooth samples, a slight temperature dependence of the coercive fields was observed and the switching along the easy axis of both FM layers was always sharp. In contrast, rough samples showed a much more pronounced temperature dependence of the switching fields due to wall pinning and below a certain temperature, the shape was also modified

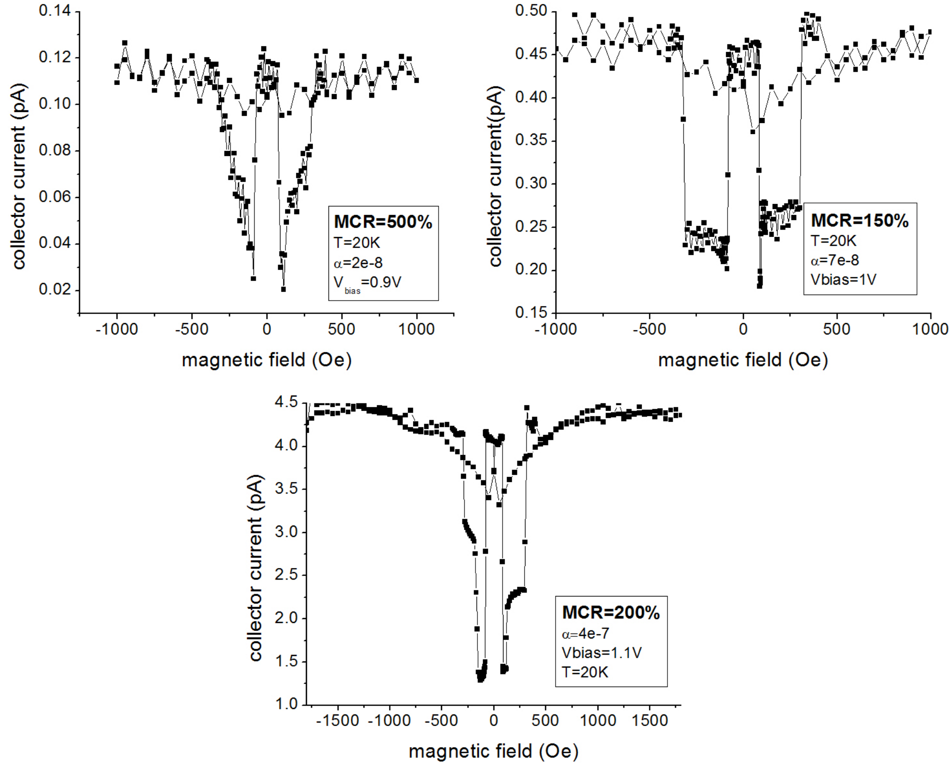

Figure 6.2: magneto current ratio for sample 1for three different emitter voltages

due to a FM coupling of the two FM layers. From the above discussion we can deduce that sample 1 is relatively rough which is consistent with the preparation method used for the substrate. As a result of the non reproducible switching and the incomplete antiparallel state obtained, the MCR is smaller than what would be expected for the FM layers' thicknesses. For the same reasons, the variation of the MCR with the emitter bias is non monotonic and depend in this case mostly on the maximum angle between the FM layers for a given measurement loop. When the MCR of single loops was measured, values of up to 800% could be obtained for an emitter voltage of 0.9 V. Finally, the collector current could only be measured up to an emitter voltage of 1.1V at which point dielectric breakdown occurred. The sudden increase of the emitter current together with the constant resistance of the emitter barrier before breakdown indicated that the breakdown was intrinsic.

The measurements made on sample 2 are shown in figure 6.3. Opposite to what was observed on sample 1, clear plateau-like antiparallel state could be obtained with this sample. As a result, the value of the MCR is increased by several hundred percents, reaching a value of 820% at the lowest voltage which gave a collector current high enough to be measured with our electrometer, namely 1V. Using the values published by Heindl [82] for the energy dependence of the effective attenuation length of FeCo we can compare the measured MCR with the theoretical one based on

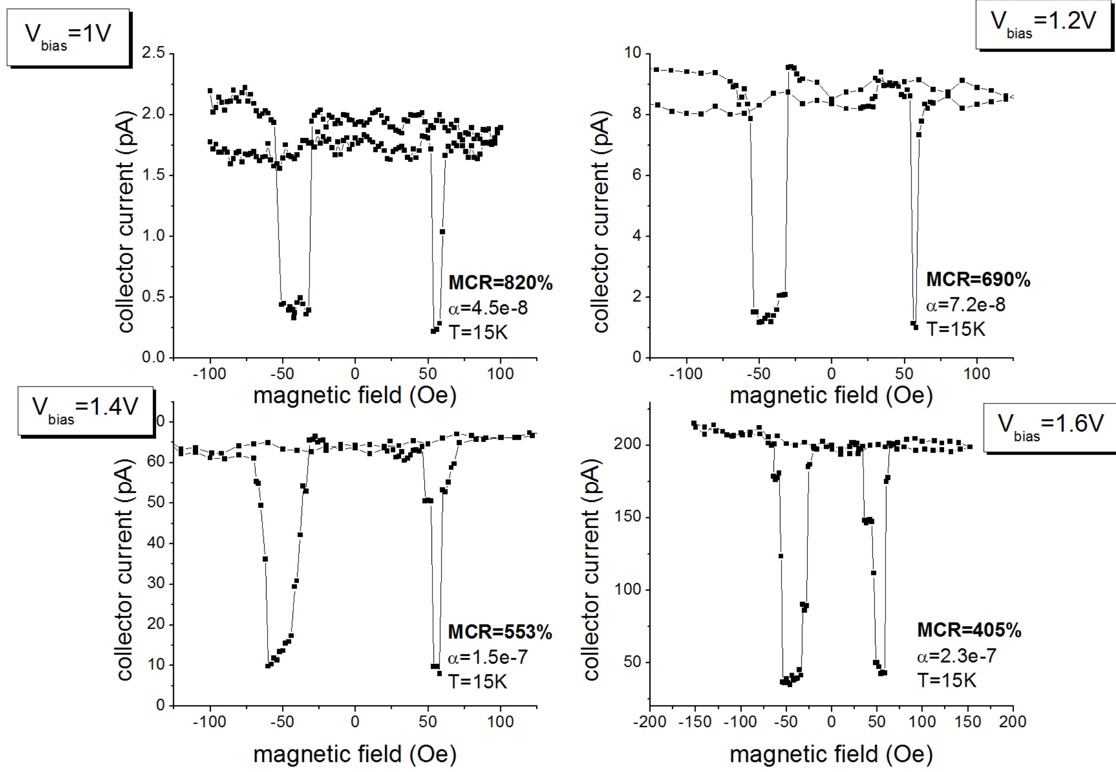

Figure 6.3: magneto current ratio for a sample 2 for four different emitter voltages

the simple analytical phenomenological model described in (2.4). Using an effective attenuation length of 9Å for the minority electrons and of 42Å for the majority electrons at $1.6V$, we obtain a theoretical value of 660%. The higher theoretical value is consistent with the fact that the attenuation length obtained by Heindl are measured by BEEM on samples grown on a GaAsP substrate. The Schottky barrier height created upon intimate contact between an FeCo layer and GaAsP is around $1eV$ which is about $0.4eV$ higher than for GaAs. The lower SBH of our samples induce for a given emitter voltage a bigger excess energy for the electrons and thus, more inelastically scattered electrons should be able to go over the Schottky barrier. Consequently, the expected MCR at a given emitter voltage is smaller for a sample grown on GaAs than on GaAsP.

6.3 Energy dependence

One of the main advantage of the MTT design is the possibility to vary the electronic energies through the emitter voltage. This property enables the study of the energy dependence of the magneto-current ratio as well as the collector current and transfer ratio, both in the parallel and antiparallel case. Figure 6.4 shows the collector

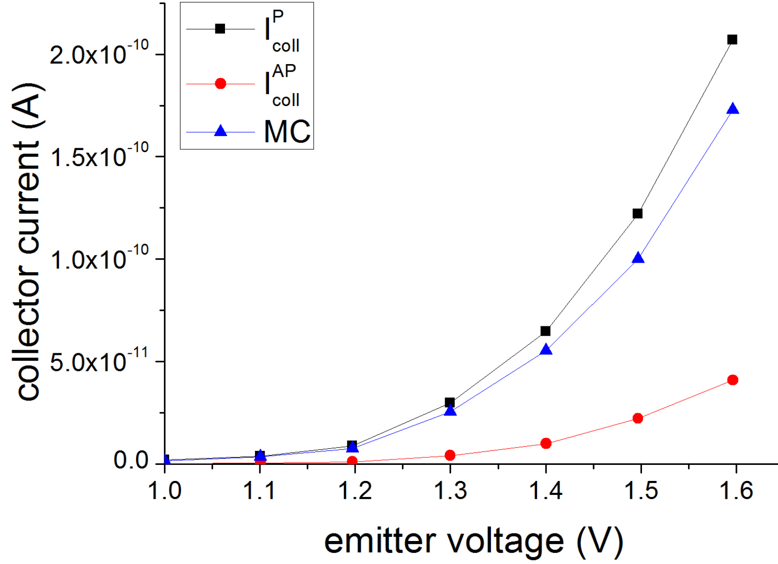

Figure 6.4: emitter voltage dependence of the collector current in the parallel and antiparallel cases and the magneto current ($MC = I^{P}_{coll} - I^{AP}_{coll}$) for sample 2 at 11K

current and magneto current ($MC = I^{P}_{coll} - I^{AP}_{coll}$) for sample 2. In the case where a fully antiparallel state can be obtained, the MC denotes simply the collector current difference between the parallel and antiparallel states. However when, as in the case of sample 1, the maximum angle between the magnetizations is smaller than 180° and most importantly varies from loop to loop, special care has to be taken in the interpretation of the data and a generalization based solely on the measurement made on such sample should be avoided. We will therefore focus our attention on sample 2. We can see that the collector currents in the parallel and antiparallel state both increase strongly with the electron energy. As pointed out in section (2.5.1), this effect is due to the combination of the increased transmission of the tunnel barrier, the augmentation of the semiconductor available phase space and the increased probability of inelastically scattered electron to still be collected. The two first reasons mentioned act on the collector current in a spin independent fashion. The last one on the other hand will have a direct influence on the MC: For moderate electron energies, inelastically scattered electrons will still lose too much energy to be collected whereas some of the minority electrons emitting a spontaneous spin wave will still be collected. As a result, an increase of $I^{\mathrm{P}}_{\mathrm{col}}$ will be observed as compared to its purely ballistic value and the MC will be augmented.

To further discuss the behavior of the sample presented here, we plotted the MCR dependence on the emitter voltage (fig.6.5 black curve). We observed here a monotonic decrease of the MCR with the bias voltage. Previous studies reported a non monotonic behavior[75, 83]. The reason for this behavior was found to be related to the elastic scattering taking place at the metal-semiconductor interface.

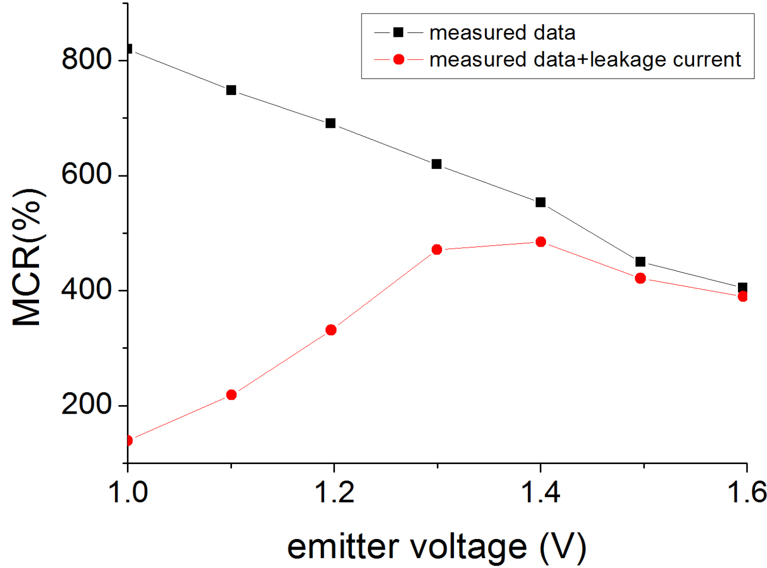

Figure 6.5: emitter voltage dependence of the MCR for sample 2 at 11K (black curve). The red curve uses the same experimental data but a voltage dependent leakage collector current corresponding to a 1TΩ stray resistance is added

It was further shown that this scattering channel had to be quite large in order to explain the non monotonic behavior, which was consistent with the fact that the metal adjacent to the SC was polycrystalline. The fact that no such observation was made here is probably due to the epitaxial structure of our spin valve that reduces the amount of defect scattering. In some other cases, the MCR was found to first increase with the electronic energy and then decrease above a certain emitter value which was comprised between 1.2 and 1.6V[50, 21]. In the case of the data presented by Hagler[50], the different energy dependence of the MCR can be explained by the different materials used in the spin valve. As was shown in [37], the evolution of $\lambda_{\uparrow}/\lambda_{\downarrow}$ is qualitatively different for Fe and Ni. We further showed in section 2.5.1 by using the values of $\lambda_{\uparrow}$ and $\lambda_{\downarrow}$ from [37] as an input to simulate the spin polarized transport in two MTTs with different FM layer structure (Fe/Au/Ni and Ni/Au/Ni) that the emitter bias dependence of the MCR was qualitatively different for the two layer structures; The MTT with an Ni/Au/Ni base showed a constant decrease of his MCR for increasing emitter voltage whereas the MTT with a Fe/Au/Ni base showed a non monotonic behavior with a maximum of the MCR around $1.5eV$. The data measured by Spitzer[21] used the same FeCo alloy as the one used here for the ferromagnetic electrodes and the exact reason as to why the qualitative variation of the MCR with the emitter voltage is different in his measurements and the one presented here is not clear. It was observed in our case that a slight punctual decrease of the insulation of the signal lines in the cryostat could give rise in some cases to a parallel current path presenting an Ohmic behavior. Depending on the

lines this parallel resistance connects, an emitter voltage dependent leakage current could be picked up by the electrometer and would contribute to the collector current, thereby modifying the emitter voltage dependence of the MCR. As an example of the potential effect this artifact would have, the red curve of figure 6.5 uses the same experimental data as the black one but a leakage current resulting from a parallel Ohmic resistance of 1TΩ between the emitter voltage line and the collector current line is artificially added to the collector current. We can see that the qualitative behavior of the MCR with V is completely changed. We do not know at this point if this is the reason for the discrepancy observed between the data presented here and the measurements of Spitzer. Some structural differences between the samples presented here and the ones of Spitzer could as well lead to the observed discrepancy. To conclude, it should be pointed out that Heindl observed as well a monotonic decrease of the MCR with increasing emitter bias using the same FeCo alloy [82]. The fact that the data were measured by BEEM should in principle not have a direct influence on the emitter voltage dependence of the MCR.

One of the main reason for using an epitaxial spin valve was the increase of the overall transmission of the MTT. It has been shown that the use of epitaxial layers can substantially increase the transfer ratio [84] The transfer ratio is defined as the ratio of the collector current to the emitter current in a given magnetic configuration. The transfer ratios obtained in this work are plotted in figure 6.6. Since most of the energy dependence of the transfer ratio arises from the increased phase space in the semiconductor, we plotted the variation of α against the difference between the emitter voltage and the Schottky barrier height, which is different for sample 1 and 2. For both samples, the transfer ratios in the parallel and antiparallel state increase with the excess emitter voltage. However, we can see that the two MTTs behave differently and that the transfer ratio for sample 1 is substantially higher than for sample 2 and increases faster. The thickness of the FM layers and the spacer in sample 1 are 6.9nm and in sample 2, 3.4nm and 6.8nm and 3.9nm. The small thicknesses difference cannot explain the difference observed in the transfer ratio. Another difference between the two sample lies in the material used for the tunnel barrier. Assuming that defects at the interface of the tunnel barrier increase the momentum distribution width of the injected electrons[85], it would be expected for sample 1 (amorphous aluminum oxide) to have a wider distribution than sample 2 (polycrystalline MgO). This would result in a decrease of the collector current and thus of α for sample 1 which is the opposite of what is observed. The reason for the difference is to be found in the presence of parallel current path in the tunnel barriers. Indeed, the breakdown of sample 1 appeared as a sudden increase of the current when the breakdown voltage was reached while for voltages below V_{break}, the current for a given voltage remained constant over several minutes. This behavior is characteristic of an intrinsic breakdown. In the contrary, the breakdown of sample 2 appeared as a slow increase of the resistance with the voltage time product which

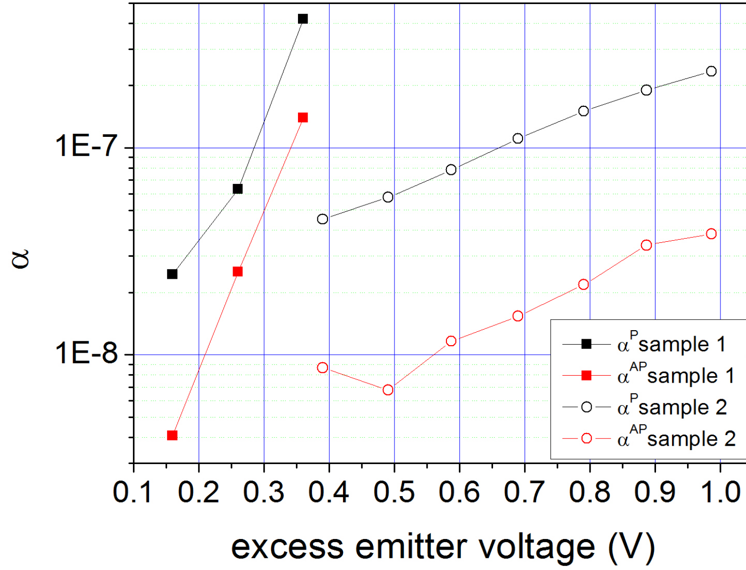

Figure 6.6: Bias dependence of the transfer ratio

is characteristic of extrinsic breakdown. Furthermore, we could observe that during the measurement of MCR loops, the emitter current was slowly increasing. Those effects are to be ascribed to the presence of one or several pinholes whose size increased with the applied voltage and the measurement time. As a result, the emitter current increase is stronger than if only tunneling was taking place and α appears smaller. This type of effect was believed to be the main reason for the small transfer ratios (2.10^{-9} for an excess voltage of 0.9V) observed by Spitzer. The intrinsic like breakdown of sample 1 together with the higher α obtained indicate that the transfer ratios measured on sample 1 do correspond to the physical quantity to be measured here, namely the ratio of the collected current to the injected current due to hot electrons. The measured value of α=4.10^{-6} at an excess voltage of 0.35V is more than two orders of magnitude higher than the one obtained by Hagler for the same excess voltage using a Py/Cu/FeCo spin valve where the Py and the Cu were polycrystalline. The layer stack he used had 0.5nm less FM material and his spacer was 0.7nm thicker. Furthermore, he used Cu as a spacer which as been reported to yield higher transmission than Au by more than one order of magnitude[86]. It is thus clear that the transfer ratio is substantially increased due to the epitaxial nature of the spin valve. However, a quantitive estimation of the influence of the crystalline structure on α cannot be obtained only from the comparison of the results presented here with the ones of Hagler due to the different materials used in the spin valve.

6.4 Conclusions and outlook

The main goal of this work was the creation of MTTs with epitaxial spin valve. The aim of this study was the assessment of the improvement of the transmission due to the reduced defect density in the metallic layers. Using a fabrication technique based on the shadow mask method, operating MTTs could be fabricated. The highest MCR measured on our samples was 820%. It was found that the MCR decreases monotonically with the emitter voltage at a temperature of 12K, contrary to what was found in a previous study[21]. A transfer ratio of $4{\cdot}10^{-6}$ in the parallel configuration at 12K and for an emitter voltage 0.35V above the Schotty barrier height was measured. This value is two orders of magnitude higher than the one obtained from a previous study on MTTs using polycristalline layers, thus indicating that the use of epitaxial layers drastically increases the transmission. The main shortcoming of the use of an epitaxial spin valve is the necessity to prepare the GaAs substrate. This substrate preparation makes it hard to reproducibly control the roughness; This leads to a variable quality both of the magnetic switching and of the tunnel barrier. To this respect, the possibility to directly combine a semiconductor MBE with a metal MBE so as to deposit the base and emitter structures on a GaAs epi-layer freshly grown without any vacuum break would be extremely beneficial since no substrate cleaning procedure would be needed. This solution will be from 2010 on readily available by the adjunction of a metal MBE chamber to the alrady existing semiconductor MBE of the Lst. Wegscheider.

The shadow mask method was found to be much more versatile and time efficient than the optical lithography and MTTs with different tunnel barrier materials could be fabricated. Furthermore, the quality of the Schottky diodes prepared by shadow mask was found to be higher. Another advantage of the shadow mask technique is that it requires almost no modifications for the implementation of alternative MTT designs such as the one with a single FM layer in the base using a FM metal as emitter. Due to the reduced number of interfaces, this design yields higher transfer ratios than the one used here. However the reports of such MTTs so far (using the following layer structure: GaAs/FeCo/Al_2O_3/NiFe) indicate a low MCR due to the fact that the MCR is limited by the spin polarization of the injected electrons. To this respect, the possible use of MgO as a tunnel emitter, that was experimentally achieved for the first time in this work, would be extremely beneficial.

Chapter 7

Summary and outlook

The main goal of this work was the fabrication of a Magnetic Tunnel Transistor (MTT) with an epitaxial spin valve base using the shadow mask technique. The MTT is a spintronic device constituted by the concatenation of a non magnetic tunnel barrier (emitter), a spin valve (base) and a Schottky barrier (collector). Its operation principle relies on the fact that the relaxation of hot electrons is spin dependent in ferromagnetic metals. The electrons are first injected into the base through the emitter barrier. The energy of the electrons can be set by modifying the bias voltage across the emitter barrier. For electronic energies higher than the Schottky barrier height, some of the electrons that are injected into the base will be collected into the collector. The condition for this is that the energy loss due to the interactions with the thermal electron bath in the base is small enough for the electron to retain an energy higher than the Schottky barrier height. The relaxation of the hot electrons in the base follows an exponential attenuation law and is more effective for minority spins than for majority spins. As a result, the MTTs are highly sensitive to externally applied magnetic fields. The normalized difference between the collector current in the parallel and antiparallel case is called the Magneto-Current Ratio (MCR=(I^{P}-I^{AP})/I^{AP}).

Due to the exponential attenuation of the hot electron in the base, the transfer ratio α, that is the ratio of the emitted to the collected current, is usually small in MTTs. This is possibly the main limitation for the use of MTTs as a magnetic field sensors since it drastically reduces the signal to noise ratio. Through the use of an epitaxial base where the density of defects is reduced, it is expected to increase α. To circumvent the limitations of optical lithography patterning as well as remove the amount of defects it creates, most noticeably at the tunnel and Schottky barriers, shadow masks are used for the fabrication of the MTTs in the present study.

Device fabrication

The MTTs were fabricated using a combination of MBE and sputtering technique. The deposition chamber used, further offered the possibility to deposit layers, both by MBE and by sputtering, through shadow masks. A mechanical system was used

to ensure that the masks could be positioned with a lateral accuracy of about $2\mu m$ with respect to the sample. In this fashion, complex layer structures and patterns could be fabricated in situ. Four masks could be stored in the MBE chamber and six in the sputtering chamber.

The GaAs(001) substrate was first cleaned and the native oxide and carbonated contaminants were removed from the surface. To this purpose, two distinct methods were used. The first method consisted in the use of Ar ion bombardment at elevated temperatures. Through this method, smooth (rms roughness of about 5Å), contaminant free surfaces could be obtained. However, due to the measurement technique used for the temperature determination, small variations in the substrate to substrate quality could not be avoided. Alternatively, the GaAs surface could be etched, prior to introduction into the deposition chamber, by means of chemical etch step in a 37% HCl solution. This step was found to efficiently remove the contaminants from the surface. The substrate roughness obtained by this method was however about twice as high as the one determined on substartes prepared with the ion bombardment technique.

The FeCo/Au/FeCo epitaxial spin valve was subsequently grown on the GaAs surface by MBE. The growth took place at room temperature to avoid intermixing between the GaAs and the FeCo. In order to obtain a good magnetic switching, a gold thickness of 16ML was used. The thickness was further chosen so as to minimize the spin independent relaxation of hot electrons in the gold layer. The thickness of the FeCo layers was varied but remained between 20 and 25ML for the bottom FeCo layer and between 25 and 35ML for the top FeCo layer. In order to avoid a direct ferromagnetic contact between the two FeCo layers, two separate masks were used for the spin valve. The first mask was used for the first FeCo and the Au layers and was a rectangular pattern $700\times1200\mu m^2$ big. The second mask was used for the second FeCo layers. Its shape was the same as the first one except for the fact that it was smaller. Its dimensions were $400\times900\mu m^2$.

The tunnel barrier was then deposited through a mask whose pattern was a disk of $500\mu m$ diameter. Several deposition techniques and materials were used. The first method used was the deposition by DC sputtering of aluminum and its subsequent oxidation in an oxygen atmosphere. The oxidation of Al taking place primarily at the grain boundaries, the grain size of the deposited Al was minimized so as to maximize the oxidation efficiency. First the FeCo surface was slightly oxidized by exposing it to an oxygen atmosphere for 2 min. The partial amorphization of the surface was ascertained by the drastic diminution of the intensity of the RHEED pattern. Furthermore, the sputtering parameters were chosen to yield the lowest grain size possible. Due to the fact that the oxidation depth by natural oxidation of aluminum is limited to 7Å, we used a stepwise deposition method where a 6Å thin Al layer was first deposited and then oxidized. This process was repeated as many times as necessary in order to obtain the desired thickness. Another technique that was used is the deposition by DC sputtering of an aluminum layer and its

subsequent oxidation by an oxygen plasma. The deposition parameters for the aluminum were the same as described above. However, due to the higher reactivity of the oxygen plasma, the oxidation depth was not limited to 7Å and there was no need for a stepwise deposition/oxidation method. A 2nm thick layer of Aluminum was therefore deposited. The sample was then transfered in a separate chamber and oxidized by means of a rotationally symmetric DC glow discharge oxygen plasma. The last method used was the RF sputtering of a 2.5nm magnesium oxide layer from a pressed MgO target.

In order to insulate the substrate from the emitter contacts, a thick Al_2O_3 was deposited by DC reactive sputtering using 1:10 O_2:Ar gas mixture. The layer was deposited through a mask consisting in two $1 \times 1 mm^2$ squares with a space $200\mu m$ space in between, thus leaving a $200\mu m$ wide channel open in order to contact the emitter and the base. Finally, the emitter and base contact were deposited by DC sputtering. A 20nm thick Ta layer was first used as an adhesion layer. Then a 100nm thick gold layer was deposited in the same fashion. Both layer were deposited through the same mask. the mask comprised both the base and emitter contacts. The base contacts were two disks of $300\mu m$ diameter. The emitter contact was a $150\mu m$ wide stripe. The effective tunnel barrier area obtained in this fashion was $150 \times 200\mu m^2$

Characterization

The magnetic properties of the MTTs were measured by longitudinal MOKE at room temperature. It was found that the switching behavior of the spin valves was largely dictated by the different layers on which the FeCo layers were grown. A separate switching of the two ferromagnetic layers could be obtained yielding an antiparallel configuration about 50 Oe wide along the magnetic easy axis at room temperature. The in plane GMR of the samples was further investigated in order to obtain complementary informations on the magnetic behavior of our samples. It was found that an antiparallel state could be obtained along the magnetic easy, middle hard and hard axis. The influence of the temperature was also studied. It was found that it depends strongly on the roughness of the samples. For smooth samples, a behavior similar to the one observed at room temperature was measured. The only difference was a slight increase of the switching fields with decreasing temperatures. In contrast, for rough samples, the switching field were strongly influenced by the temperature. Furthermore, below 90K, a ferromagnetic coupling possibly of the Néel type existed between the two ferromagnetic layer and no clear antiparallel state could be observed.

The properties of both the Schottky diodes and the tunnel barriers were measured in a four point geometry at in the temperature range 12-300K. The FeCo/GaAs Schottky diodes were found to be strongly influenced by the substrate preparation method. For substrates prepared by ion bombardment, a Schottky barrier height of $0.61eV$ and an ideality factor of 1.27 were measured whereas for the ones prepared

by an HCl etch, we obtained a Schottky barrier height of $0.75eV$ and an ideality factor of 1.02. The discrepancy was ascribed to the different surface termination that the preparation yield (As-terminated for HCl and Ga-terminated for ion bombardment). The influence of the structuring method was investigated by comparing Schottky diodes made by optical lithography and shadow mask deposition. It could be measured that the diodes made by lithography and dry ion etching have a higher defect density with lower Schottky barrier height at the edges due to the dry etching. Those could be only partially removed by a subsequent wet chemical repair step. In contrast deposition through shadow masks does not create such defects. Those defects are detrimental to the quality of the diodes since they lower their rectifying action, thereby reducing their efficiency as a high pass filter for the ballistic electrons in the MTT. The influence of the dopant concentration was as well studied and it could be observed that the reduction of the thermal current due to the reduction of the doping was markedly stronger for samples made by shadow masks.

Finally, the tunnel barriers were characterized and the efficiency of the different barrier materials and oxidation methods was assessed. Electronic hopping was found to be responsible for part of the transport in naturally oxidized barriers, indicating that the barriers were not fully oxidized. Furthermore, a large discrepancy between the deposited thickness and the mean thickness obtained from the electrical data indicated that the barriers were very rough. As a result, their breakdown voltages were too low for them to be used as an emitter in MTTs. The barriers made by plasma oxidation in contrast, were fully oxidized and smoother and the magnitude of the breakdown voltage was consequently twice as high. The MgO barriers were as well smooth and no hopping could be measured. Their breakdown voltage was the highest. It was further measured that for all types of barriers, both intrinsic and extrinsic breakdown occurred. However, the type of breakdown was always constant within one sample, thus indicating that the barriers quality was varying from substrate to substrate.

Spin dependent transport in the Magnetic Tunnel Transistor

The MTTs were measured at 12K.Magneto-Current Ratio ($MCR = (I^{\mathrm{P}} - I^{\mathrm{AP}})/I^{\mathrm{AP}}$) of up to 820% were measured, depending on the emitter voltage. As in the case of the GMR, it was found that the substrate roughness influences the magnetic switching of the MTTs. As a result, some MTTs showed no antiparallel state and the MCR was consequently reduced. The MCR was monotonically decreasing with increasing emitter voltages. This decrease contradicts other experimental reports made on MTTs with polycristalline layers and it is believed that the qualitative behavior results form the different densities of defects[75]. A transfer ratio α of $4{\cdot}10^{-6}$ in the parallel configuration at 12K and for an emitter voltage 0.35V above the Schotty barrier height was measured. This value is two orders of magnitude higher than the one obtained from a previous study on MTTs using polycristalline layers, thus indicating that the use of epitaxial layers drastically increases the transmission.

Furthermore, the aforementionned study used Cu as a spacer layer, which is known to yield a higher transmission than Au. The increase of α due to the reduction of the defect density is therefore even higher than the difference measured here. By comparing α on samples having a tunnel emitter with or without pinholes, it could be seen how Ohmic current path in the barrier effectively reduces the measured transfer ratio.

The shadow mask technique employed in this work has proved to be much more versatile and time efficient than the patterning by optical lithography. Furthermore, it allows the patterning of different MTT designs with minimum modifications. However, in order to improve the process reliability, an improved technique should be used to fabricate the masks. This would allow the definition of tunnel barriers with smaller areas, thereby increasing the breakdown voltage and long life cycle of the barriers and decreasing the likelihood of having pinholes in the barriers.

In order to further improve the fabrication process, the possibility to deposit the spin valve base and the tunnel emitter on a freshly grown GaAs epi-layer without any vacuum break would be greatly beneficial since no annealing of the substrate or ion bombardment would be necessary. An alternative way would be of course to use different substrates such as Si which can be readily prepared by chemical means prior to the growth of the res of the MTT layers. The use of an epitaxial MgO barrier would allow the fabrication of a fully epitaxial MTT. By minimizing the interface scattering at the tunnel barrier, the transfer ratio could be further increased thereby achieving one step further towardt he use of MTT as an efficient spin injector. Another approach that could be used to increase α is the use of different spacer materials such as Cu. However, the growth conditions would have to be carefully optimized so that the layers remain epitaxial while no increase in the roughness occurs.

Appendix A

Simulation framework

The Monte Carlo (MC) algorithm is a statistical numerical method based on a probabilistic approach. In the case of transport simulations, the MC method consists in the numerical solving of the Boltzmann equation for electrons constricted in a given device structure under the influence of external fields and interaction with other particles or quasi particles. The motion is subdivided into several elementary paths called free flights which lengths are chosen stochastically according to the probabilities describing the interaction of the electrons and the aforementioned perturbations influencing the transport. At the end of each free flight, the electrons undergo a collision with another particle. The nature of this collision and its outcome are again decided stochastically in accordance with the probability laws describing particle-particle interactions. We will here describe the details of the framework used in this work to simulate transport in a MTT structure. The core of the scheme is directly adapted from the method described in [87]. Three main phases are considered:

1. emission of hot electrons from the tunnel barrier into the base
2. hot electron transport through the base
3. collection at the metal-semiconductor interface

A.1 Hot electron emission

The computation of the injected electrons distribution is necessary as it will define the initial state of the simulation. We start by randomly selecting a state in the emitter. We assume here that the electrons in the emitter form a free electron gas and a usual quadratic dispersion relation is taken. At T=0K, only the states within the Fermi sphere will be occupied. As T is increased, the electronic distribution broadens following a Fermi-Dirac distribution. Since above a certain k-vector value k_{high}, the occupation probability will be negligible, we restrict our sampling to the

sphere in the k-space of radius

$$k_{\text{high}} = (1 + \frac{6k_{\text{B}}T}{E_{\text{F}}})$$

We then use the algorithm known as the von Neumann algorithm to select the states inside the sampling sphere. It consist in randomly selecting a state in the cube of side k_{high}. This procedure is repeated until the wavevector of the selected state falls inside the sampling sphere. The tunneling probability P_{tun} of this state is then calculated as the product of the occupation probability $f(E)$ in the emitter, the vacancy probability in the base $1-f(E+eV)$ and the WKB probability $P_{\text{WKB}}(E_\perp)$, where $f(E)$ is the Fermi-Dirac distribution at the energy E and

$$P_{\text{WKB}}(E_\perp) = exp\left[-\frac{1}{\hbar}\int_0^t \sqrt{2m\left(-\frac{eV}{t}x + E_{\text{F}} + \varphi - E_\perp\right)}dx\right]$$

V is the voltage drop across the tunnel barrier, φ and t are the mean barrier height and thickness, x is the distance from the emitter metal-insulating material interface and $E_\perp$ is the kinetic energy in the direction perpendicular to the interface. The tunneling probability is then compared to a random number α between 0 and 1. Only if $\alpha < P_{\text{tun}}$ will the electron tunnel through the barrier.

Since below a certain energy, the tunneling probability tends to zero, we restrict further our sampling space, thereby increasing the computation efficiency, by defining a minimum wavevector $k_{\text{low}}^2 = \frac{2m}{\hbar^2}(E_F - eV - 8k_{\text{B}}T)$ and by selecting our states within the spherical ring which radius is comprised between k_{low} and k_{high}. In order to compute the actual current density, we still need to calculate the incident charge flux on the emitter metal-insulator interface. This flux is proportional to the velocity toward the interface $\hbar k_\perp/m$ and the electronic charge e. Furthermore, to account for the fact that we use a discrete ensemble, we have to multiply those factors by the phase space volume of the sampled state $\Delta^3 k = n/N$ where n is the real space density and N is the sampling number. However, since the computation takes place at non zero temperatures, we need to replace N by the sum of the occupation probabilities, $N_{\text{th}} = \sum f(E)$. Furthermore to account for the fact that we use a sampling phase space that is smaller than the actual one, we define an effective sampling number in order to include as well the states comprised in the sphere which radius is inferior to k_{low}

$$N' = N_{\text{th}} + N\frac{Volume(k < k_{\text{low}})}{Volume(k_{\text{low}} < k < k_{\text{high}})}$$

Finally the current density can be written as:

$$I_{\text{emitter}} = eA\frac{\hbar n}{mN'}\sum k_\perp \tag{A.1}$$

where the sum is over the electrons that tunnel through the barrier. The electron ensemble obtained in this fashion is then used as an initial ensemble that will be used as an input for the transport simulation in the base and the collector

A.2 Hot electron transport in the base

The hot electron transport is considered as being a succession of scattering events, separated by free flights. The scattering events considered here can take place either in the bulk of the layers or at the interfaces. Bulk scattering comprehend thermal spin waves scattering and inelastic scattering. Elastic defect scattering is the only mechanism considered for the interfaces. Each of those scattering mechanisms is assigned a given probability law and will induce specific reactions.

In the case of inelastic scattering, we use the energy and spin dependent inelastic mean free paths for Fe Ni and Au published in [37]. Those inelastic mean free path take into account the effect of electron electron scattering and spontaneous spin wave emission. In the energy range considered, electron electron scattering reduce the hot electrons by about half. An electron electron scattering event will therefore preclude any further possible collection of the scattered electron. A minority electron spontaneously emitting a spin wave can however if the spin wave wavevector is short enough still be collected. However, since there was no available unambiguous data, neither on the relative importance of spontaneous spin wave emission over e-e scattering nor on the spin wave wavevector and electron energy dependence of the spontaneous spin wave emission probability, we assumed here that any inelastic scattering would reduce the electrons energies to a level below the lowest one required for overcoming the Schottky barrier.

Thermal spin wave scattering is included by using measurements of the temperature dependent spin wave scattering length from [88]. Since the maximum possible energy for thermal spin wave is about 60meV and the thermal spin wave have with 90% probability a wavevector lower than $0{,}1k_{\mathrm{F}}$ in Fe, we considered thermal spin wave scattering to be a purely elastic process and that the modifictiono f the lectronic wavevector was negligible. The sole effect of thermal spin wave scattering is to flip the spin of the scattered electron. Further, we considered the spin wave scattering lengths to be energy independent.

Finally, since the magnitude of defect scattering strongly varies within the literature and since it has been shown that the defects are mostly localized at the interfaces [11] [19] and induce no spin asymmetry, defect scattering are accounted for by the use of a scattering factor D which is taken as a variable parameter. When an electron reaches an interface, it will have the probability D to scatter on a defect. In this case, its wavevector's direction will be randomly redistributed in an isotropic manner.

In order to calculate the free flight length, we define the effective attenuation length to be

$$\lambda_{\text{eff}} = \frac{\Lambda_{\text{in}}(E)\Lambda_{\text{tsw}}(T)}{\Lambda_{\text{in}}(E) + \Lambda_{\text{tsw}}(T)}$$

where Λ_{in} and Λ_{tsw} are the inelastic mean free path and the thermal spin wave scattering length respectively. The probability for a given electron to travel the distance l at an energy E and temperature T is then

$$P = \exp\left(-\frac{l}{\lambda_{\text{eff}}}\right)$$

The calculation of the free flight length l_{ff} is then just the stochastic determination of a distance according to this probability law: first a random number α is chosen and then l_{ff} is calculated as

$$l_{\text{ff}} = -\lambda_{\text{eff}} ln(\alpha)$$

at the end of a free flight, the selection of the scattering mechanism is done by defining a total scattering probability $P_{\text{tot}} = P_{\text{in}} + P_{\text{tsw}}$. we then compare a random number between 0 and 1 with $P_{\text{in}}/P_{\text{tot}}$. The outcome of this comparison will determine which type of scattering event the electron will undergo. The numerical procedure used to simulate the transport in the whole base is described in the flowchart in figure A.1.

Finally, it should be mentioned that all through the calculation, the real bandstructure of the material is taken into account only through Λ_{in} and Λ_{tsw}. Λ_{tsw} was measured in polycrystalline materials with no indication of a preferred orientation and the values of Λ_{in} used are k-averaged. Any anisotropy effect is therefore excluded from our calculation.

A.3 Collection at the metal-semiconductor interface

We consider the bandstructure of GaAs to consist in the valleys centered around the Γ, X and L points. The parameters describing a valley i are the density of state effective mass m_{i}, the nonparabolicity parameter α_{i}, the energetic separation from the minimum of the conduction band $d_{\Gamma\text{i}}$ and the position in k space of the valley's minimum k_{i}. The numerical values used in the simulation are summarized in table A.1. Within the valley i, the dispersion relation is then

$$E_{\text{SC}} = \frac{\hbar^2 k_{\text{SC}}^2}{2m_{\text{i}}^*} = \frac{\hbar^2 \left\|\vec{k} - \vec{k_{\text{i}}}\right\|^2}{2m_i\left(1 + \alpha_{\text{i}} E_{\text{SC}}\right)}$$

where $\vec{k}$ is the wave vector in the semiconductor taken from the center of Brillouin zone. The condition for collection at the metal-semiconductor interface is that there are available states in the semiconductor matching the electron energy and parallel

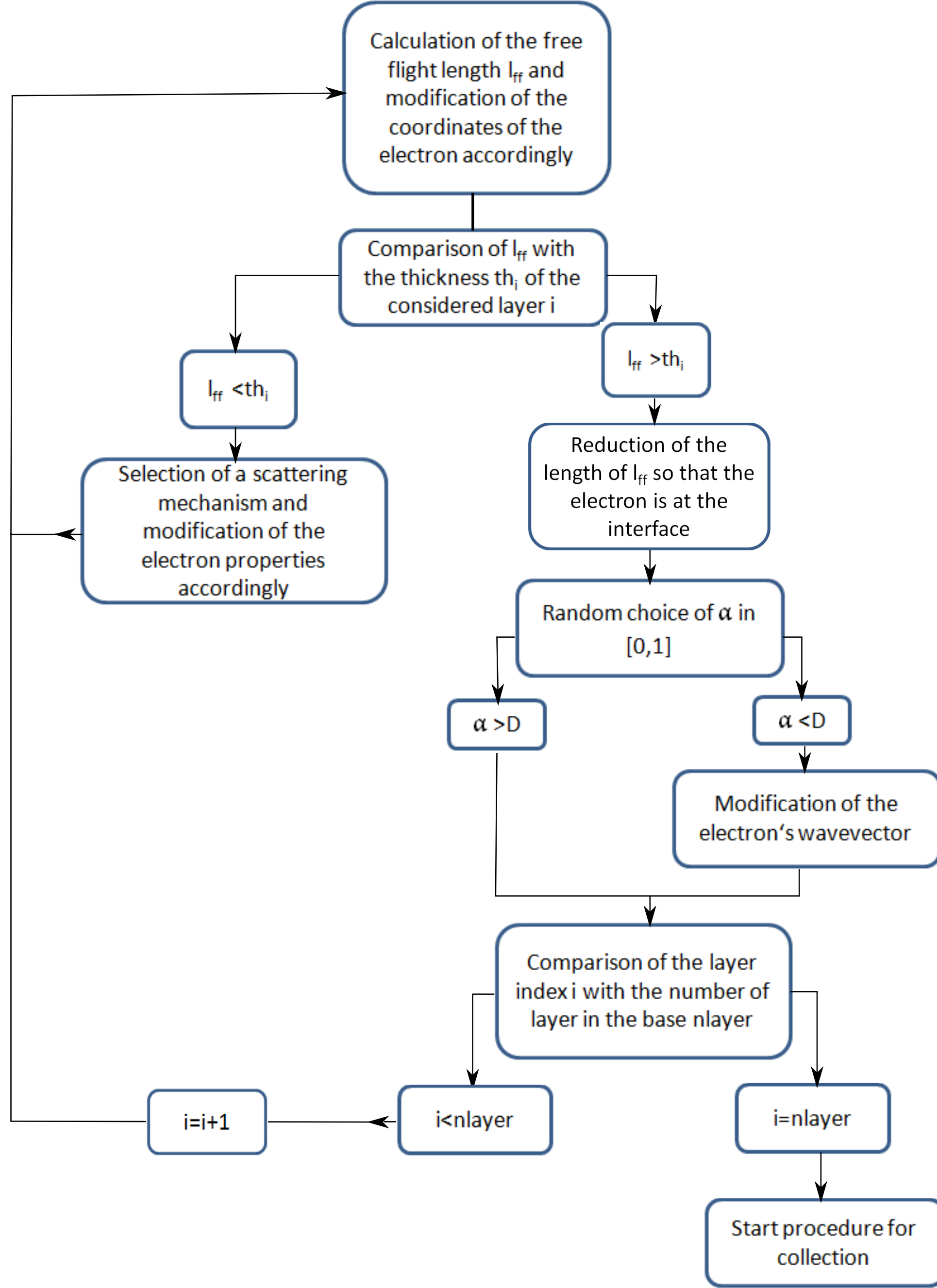

Figure A.1: Flowchart of the simulation procedure in the base

wavevector, since those two parameters are conserved when crossing the interface. This translates into a set of two conditions for each valley: the energy of the electron has to be higher than the Schottky barrier height Φ_B and the parallel wavevector has to lie within the projection on the interface Brillouin zone of the constant energy sphere or

$$E - (E_C - E_F) \geq \Phi_B + d_{\Gamma i} \tag{A.2}$$

m_Γ	$0.063m_\mathrm{e}$
m_L	$0.85m_\mathrm{e}$
m_X	$0.85m_\mathrm{e}$
$d_{\Gamma\mathrm{L}}$	0.29eV
$d_{\Gamma\mathrm{X}}$	0.48eV
α_Γ	$0.69\mathrm{eV}^{-1}$
α_L	$0.65\mathrm{eV}^{-1}$
α_X	$0.5\mathrm{eV}^{-1}$

Table A.1: numerical values used in the numerical simulations to describe the properties of the GaAs collector

and

$$k_{\mathrm{SC}\parallel} \leq r_\mathrm{i}(E) = \frac{\sqrt{2m_\mathrm{i}^* \left[E - (E_\mathrm{F} - E_\mathrm{C}) - \Phi_\mathrm{B} - d_{\Gamma\mathrm{i}}\right]}}{\hbar} \tag{A.3}$$

The parallel wavevector in the semiconductor $k_{\mathrm{SC}\parallel}$ has already been modified so as to center it at the center of the valley considered. The conditions on energy and parallel wavevector conservation necessarily imply that due to bandstructure effects, the perpendicular component of the wavevector will be modified when entering the semiconductor. Indeed, the equation stating the conservation of the energy is

$$E_\mathrm{M} - (E_\mathrm{F} - E_\mathrm{C}) = E_\mathrm{SC} + \Phi_\mathrm{B} + d_{\Gamma\mathrm{i}}$$

Given the conservation of parallel wavevector, this equation is equivalent to

$$\frac{\hbar^2 k_{\mathrm{M}\parallel}^2}{m} + \frac{\hbar^2 k_{\mathrm{M}\perp}^2}{m} - (E_\mathrm{F} - E_\mathrm{C}) = \frac{\hbar^2 k_{\mathrm{SC}\parallel}^2}{m_\mathrm{i}^*} + \frac{\hbar^2 k_{\mathrm{SC}\perp}^2}{m_\mathrm{i}^*} + \Phi_\mathrm{B} + d_{\Gamma\mathrm{i}}$$

which can be rewritten as

$$k_{\mathrm{SC}\perp} = \sqrt{k_{\mathrm{M}\parallel}^2 \frac{m_\mathrm{i}^*}{m} - k_{\mathrm{SC}\parallel}^2 + k_{\mathrm{M}\perp}^2 \frac{m_\mathrm{i}^*}{m} - \frac{2m_\mathrm{i}^*}{\hbar^2}\left(E_\mathrm{F} + \Phi_\mathrm{B} + d_{\Gamma\mathrm{i}} - E_C\right)} \tag{A.4}$$

Even if the electron satisfies the condition (3.1) and (3.2), there is a possibility that it will bounce back off the interface due to quantum mechanical reflection. The probability for this to happen is

$$P_\mathrm{QM} = \frac{4k_{\mathrm{M}\perp}\frac{m_\mathrm{i}^*}{m}\left(k_{\mathrm{SC}\perp} + k_{\mathrm{i}\perp}\right)}{\left[k_{\mathrm{SC}\perp} + k_{\mathrm{i}\perp} + k_{\mathrm{M}\perp}\frac{m_\mathrm{i}^*}{m}\right]^2}$$

The collection procedure is then:

1. verify if the electron satisfies the collection conditions (A.2) and (A.3)
2. if it does calculate $k_{\mathrm{SC}\perp}$

3. calculate P_{QM} and pick a random number u

4. if $u < P_{\mathrm{QM}}$ the electron is collected and participate to the collector current

At any step of the procedure, if the electron considered does not fulfill one of the test, it will bounce back into the base and the procedure for the transport in the base is resumed. Once the complete evolution of all sampled states has been simulated, the collector current is calculated as in equation (A.1).

Bibliography

[1] M. N. Baibich, J. M. Broto, A. Fert, F. N. Van Dau, F. Petroff, P. Etienne, G. Creuzet, A. Friederich, and J. Chazelas. "Giant magnetoresistance of (001)fe/(001)cr magnetic superlattices". *Phys. Rev. Lett.*, **61**, 2472 (1988).

[2] G. Binasch, P. Grünberg, F. Saurenbach, and W. Zinn. "Enhanced magnetoresistance in layered magnetic structures with antiferromagnetic interlayer exchange". *Phys. Rev. B*, **39**, 4828 (1989).

[3] J. M. "Tunneling between ferromagnetic films". *Phys. Lett. A*, **54**, 225 (1975).

[4] J. S. Moodera, L. R. Kinder, T. M. Wong, and R. Meservey. "Large magnetoresistance at room temperature in ferromagnetic thin film tunnel junctions". *Phys. Rev. Lett.*, **74**, 3273 (1995).

[5] S. Ikeda, J. Hayakawa, Y. Ashizawa, Y. M. Lee, K. Miura, H. Hasegawa, M. Tsunoda, F. Matsukura, and H. Ohno. "Tunnel magnetoresistance of 604% at 300 K by suppression of Ta diffusion in CoFeB / MgO / CoFeB pseudo-spin-valves annealed at high temperature". *Appl. Phys. Lett.*, **93**, 082508 (2008).

[6] C. A. Mead. "Operation of tunnel emission devices". *J. Appl. Phys.*, **32**, 646 (1961).

[7] M. Heiblum and M. V. Fischetti. "Ballistic hot electron transistors". *IBM J. Res. Develop*, **34**, 530 (1990).

[8] L. Bell and W. Kaiser. "Observation of interface band structure by ballistic electron emission microscopy". *Phys. Rev. Lett.*, **61**, 2368 (1988).

[9] L. D. Bell and W. J. Kaiser. "Ballistic electron emission microscopy: A nanometer-scale probe of interfaces and carrier transport". *Annu. Rev. Mater. Sci.*, **26**, 189 (1996).

[10] D. J. Monsma, R. Vlutters, and J. C. Lodder. "Room Temperature-Operating Spin-Valve Transistors Formed by Vacuum Bonding". *Science*, **281**, 407 (1998).

[11] R. Jansen. "The spin-valve transistor: A review and outlook". *J. Phys. D: Appl. Phys.*, **10**, 38950 (2003).

[12] S. van Dijken, X. Jiang, and S. S. P. Parkin. "Spin-dependent hot electron transport in $Ni_{81}Fe_{19}$ and $Co_{84}Fe_{16}$ films on GaAs (001)". *Phys. Rev. B*, **66**, 094417 (2002).

[13] R. Sato and K. Mizushima. "Spin-valve transistor with an Fe-Au-Fe(001) Base". *Appl. Phys. Lett.*, **79**, 1157 (2001).

[14] G. Rodary, M. Hehn, T. Dimopoulos, D. Lacour, J. Bangert, H. Jaffres, F. Montaigne, F. N. van Dau, F. Petroff, A. Schuhl, and J. Wecker. "Development of a magnetic tunnel transistor based on a double tunnel junction". *J. Magn. Magn. Mater.*, **291**, 1097 (2005).

[15] J. H. Lee, K. I. Jun, K. H. Shin, S. Y. Park, J. K. Hong, K. Rhie, and B. C. Lee. "Large magnetocurrents in double-barrier tunneling transistors". *J. Magn. Magn. Mater.*, **286**, 138 (2005).

[16] S. van Dijken, X. Jiang, and S. S. P. Parkin. "Giant magnetocurrent exceeding 3400% in magnetic tunnel transistors with spin-valve base layers". *Appl. Phys. Lett.*, **83** (2003).

[17] X. Jiang, R. Wang, S. van Dijken, R. Shelby, R. Macfarlane, G. S. Solomon, J. Harris, and S. S. P. Parkin. "Optical Detection of Hot-Electron Spin Injection into GaAs from a Magnetic Tunnel Transistor Source". *Phys. Rev. Lett.*, **90**, 256603 (2003).

[18] I. Appelbaum, B. Huang, and D. J. Monsma. "Electronic measurement and control of spin transport in silicon". *Nature*, **447**, 295 (2007).

[19] R. Vlutters, O. M. J. van '. Erve, R. Jansen, S. D. Kim, J. C. Lodder, A. Vedyayev, and B. Dieny. "Modeling of spin-dependent hot-electron transport in the spin-valve transistor". *Phys. Rev. B*, **65**, 024416 (2001).

[20] E. Heindl, J. Vancea, G. Woltersdorf, and C. H. Back. "Hot-electron transport and magnetic anisotropy in epitaxial spin valves". *Phys. Rev. B*, **76**, 104435 (2007).

[21] A. Spitzer. *Realisierung eines magnetischen Tunneltransistors mit epitaktischer Spinvalve-Basis und Magnetostrom-Effekt bei Zimmertemperatur.* Ph.D. thesis, Institut für Experimentelle und Angewandte Physik, Universität Regensburg (2008).

[22] J. G. Simmons. "Generalized Formula for the Electric Tunnel Effect between Similar Electrodes Separated by a Thin Insulating Film". *J. Appl. Phys.*, **34**, 1793 (1963).

[23] J. G. Simmons. "Generalized Thermal J-V Characteristic for the Electric Tunnel Effect". *J. Appl. Phys.*, **35**, 2655 (1964).

[24] W. F. Brinkman, R. C. Dynes, and J. M. Rowell. “Tunneling Conductance of Asymmetrical Barriers”. *J. Appl. Phys.*, **41**, 1915 (1970).

[25] E. Burnstein and S. Lundqvist, eds. *Tunneling phenomena in solids*. Plenum press, New York (1969).

[26] B. J. Jonsson-Akerman, R. Escudero, C. Leighton, S. Kim, and I. K. Schuller. “Reliability of normal-state current-voltage characteristics as an indicator of tunnel-junction barrier quality”. *Appl. Phys. Lett.*, **77**, 1870 (2000).

[27] V. D. Costa, F. Bardou, C. Beal, Y. Henry, J. P. Bucher, and K. Ounadjela. “Nanometric cartography of tunnel current in metal-oxide junctions”. *J. Appl. Phys.*, **83**, 6703 (1998).

[28] C. W. Miller, Z.-P. Li, and I. K. Schuller. “Impact of interfacial roughness on tunneling conductance and extracted barrier parameters”. *Appl. Phys. Lett.*, **90**, 043513 (2007).

[29] W. Oepts, H. J. Verhagen, R. Coehoorn, and W. J. M. de Jonge. “Analysis of breakdown in ferromagnetic tunnel junctions”. *J. Appl. Phys.*, **86**, 3863 (1999).

[30] B. Oliver, Q. He, X. Tang, and J. Nowak. “Dielectric breakdown in magnetic tunnel junctions having an ultrathin barrier”. *J. Appl. Phys.*, **91**, 4348 (2002).

[31] J. Kirschner. “Direct and exchange contributions in inelastic scattering of spin-polarized electrons from iron”. *Phys. Rev. Lett.*, **55**, 973 (1985).

[32] J. Hong and D. L. Mills. “Spin dependence of the inelastic electron mean free path in fe and ni: Explicit calculations and implications”. *Phys. Rev. B*, **62**, 5589 (2000).

[33] J. Kirschner, D. Rebenstorff, and H. Ibach. “High-resolution spin-polarized electron-energy-loss spectroscopy and the stoner excitation spectrum in nickel”. *Phys. Rev. Lett.*, **53**, 698 (1984).

[34] M. Etzkorn. *Spin waves with high energy and momentum in ultrathin Co-films studied by spin-polarized electron energy loss spectroscopy*. Ph.D. thesis, Mathematisch-Naturwissenschaftlich-Technischen Fakultt der Martin-Luther-Universitt Halle-Wittenberg (2005).

[35] M. Plihal, D. L. Mills, and J. Kirschner. “Spin wave signature in the spin polarized electron energy loss spectrum of ultrathin fe films: Theory and experiment”. *Phys. Rev. Lett.*, **82**, 2579 (1999).

[36] J. Hong and D. L. Mills. “Theory of the spin dependence of the inelastic mean free path of electrons in ferromagnetic metals: A model study”. *Phys. Rev.*, **59**, 11821 (1999).

[37] V. P. Zhukov, E. V. Chulkov, and P. M. Echenique. "Lifetimes and inelastic mean free path of low-energy excited electrons in Fe, Ni, Pt, and Au: Ab initio GW+ T calculations". *Phys. Rev.*, **73**, 125105 (2006).

[38] V. P. Zhukov, E. V. Chulkov, and P. M. Echenique. "Lifetimes of Excited Electrons In Fe And Ni: First-Principles GW and the T-Matrix Theory". *Phys. Rev. Lett.*, **93**, 1 (2004).

[39] T. Banerjee, J. C. Lodder, and R. Jansen. "Origin of the spin-asymmetry of hot-electron transmission in Fe". *Phys. Rev. B*, **76**, 140407 (2007).

[40] P. L. de Andres, F. J. Garcia-Vidal, K. Reuter, and F. Flores. "Theory of ballistic electron emission microscopy". *Prog. Surf. Sci.*, **66**, 3 (2001).

[41] C. Crowell and S. Sze. "Current transport in metal-semiconductor barriers". *Solid-State electron.*, **9**, 1035 (1966).

[42] B. Sharma, ed. *Metal-semiconductor Schotky barrier junctions and their applications.* Plenum press, New York (1984).

[43] J. J. O'Shea, T.Sajoto, S. Bhargava, D. Leonard, M. Chin, and V. Narayanamurti. "Measurement of heterojunction band offsets using ballistic electron emission microscopy". *J. Vac. Sci. Technol. B.*, **12**, 2625 (1994).

[44] M. l. Ke, D. I. Westwood, C. C. Matthai, B. E. Richardson, and R. H. Williams. "Hot-electron transport through Au/GaAs and Au/GaAs/AlAs heterojunction interfaces: Ballistic-electron-emission-microscopy measurement and Monte Carlo simulation". *Phys. Rev. B*, **53**, 4845 (1996).

[45] L. J. Schowalter and E. Y. Lee. "Role of elastic scattering in ballistic-electron-emission microscopy of Au/Si(001) and Au/Si(111) interfaces". *Phys. Rev. B.*, **43**, 9308 (1991).

[46] D. L. Smith, E. Y. Lee, and V. Narayanamurti. "Ballistic Electron Emission Microscopy for Nonepitaxial Metal/Semiconductor Interfaces". *Phys. Rev. Lett.*, **80**, 05473 (1998).

[47] C. R. Crowell and S. M. Sze. "Quantum mechanical reflection of electrons at metal-semiconductor barriers: electron transport in semiconductor-metal semiconductor structures". *J. Appl. Phys.*, **37**, 2683 (1966).

[48] E. Y. Lee and L. J. Schowalter. "Phonon scattering and quantum mechanical reflection at the Schottky barrier". *J. Appl. Phys.*, **70**, 2156 (1991).

[49] S. M. Sze, C. R. Crowell, G. P. Carey, and E. E. LaBate. "Hot-Electron Transport in Semiconductor-Metal-Semiconductor Structures". *J. Appl. Phys.*, **37**, 2690 (1966).

[50] T. Hagler, C. Bilzer, M. Dumm, W. Kipferl, and G. Bayreuther. “Semi-epitaxial magnetic tunnel transistor: Effect of electron energy and temperature”. *J. Appl. Phys.*, **97**, 10D505 (2005).

[51] J. Hong and R. Q. Wu. “Bias and temperature dependence of hot electron transport in a spin-valve structure”. *J. Appl. Phys.*, **93**, 7525 (2003).

[52] R. Jansen, P. S. A. Kumar, O. M. J. v. Erve, R. Vlutters, P. de Haan, and J. C. Lodder. “Thermal Spin-Wave Scattering in Hot-Electron Magnetotransport Across a Spin Valve”. *Phys. Rev. Lett.*, **85**, 3277 (2000).

[53] M. G. Kang, S. H. Sa, H. H. Park, K. S. Suh, and K. H. Oh. “The characterization of etched GaAs surface with HCl or H_3PO_4 solutions”. *Thin Solid Films*, **309**, 634 (1997).

[54] K. E. Mello, S. R. Soss, S. P. Murarka, T.-M. Lub, and S. L. Lee. “Epitaxial quality of thin Ag films on GaAs(100) surfaces cleaned with various wet etching techniques”. *Appl. Phys. Lett.*, **68**, 681 (1996).

[55] Z. Song, S. Shogen, M. Kawasaki, and I. Suemune. “X-ray photoelectron spectroscopy and atomic force microscopy surface study of GaAs[100] cleaning procedures”. *J. Vac. Sci. Technol. B*, **13**, 77 (1995).

[56] M. Dumm. *Herstellung und Charakterisierung vollstandig epitaktischer magnetischer Tunnelelemente mit Halbleiterbarriere*. Ph.D. thesis, Institut für Experimentelle und Angewandte Physik, Universität Regensburg (2005).

[57] T. L. Monchesky, B. Heinrich, R. Urban, K. Myrtle, M. Klaua, and J. Kirschner. “Magnetoresistance and magnetic properties of fe/cu/fe/gaas(100)”. *Phys. Rev. B.*, **60**, 10242 (1999).

[58] E. E. Fullerton, J. Pearson, C. H. Sowers, S. D. Bader, X. Z. Wu, and S. K. Sinha. “Interfacial roughness of sputtered multilayers: Nb/si”. *Phys. Rev. B*, **48**, 17432 (1993).

[59] L. P. H. Jeurgens, W. G. Sloof, F. D. Tichelaar, and E. J. Mittemeijer. “Growth kinetics and mechanisms of aluminum-oxide films formed by thermal oxidation of aluminum”. *J. Appl. Phys.*, **92**, 1649 (2002).

[60] M. Bowen, V. Cros, F. Petroff, A. Fert, .-J. M. de Teresa, L. Morellon, and M. R. Ibarra. “Large magnetoresistance in Fe-MgO-FeCo(001) Epitaxial tunnel junctions on GaAs(001)”. *Appl. Phys. Lett.*, **79**, 645 (2001).

[61] S. Yuasa, A. Fukushima, T. Nagahama, K. Ando, and Y. Suzuki. “High Tunnel Magnetoresistance at Room Temperature in Fully Epitaxial Fe/MgO/Fe Tunnel Junctions due to Coherent Spin-Polarized Tunneling”. *J.J.A.P.*, **43**, L588 (2004).

[62] W. Shen, D. Mazumdar, X. Zou, X. Liu, B. D. Schrag, and G. Xiao. "Effect of film roughness in MgO-based magnetic tunnel junctions". *Appl. Phys. Lett.*, **88**, 182508 (2006).

[63] I. Safi. "Recent aspects concerning DC reactive magnetron sputtering of thin films: A review". *Surf. Coat. Technol.*, **127**, 203 (2000).

[64] W. D. Sproul, D. J. Christie, and D. C. Carter. "Control of reactive sputtering processes". *Thin Solid Films*, **491**, 1 (2005).

[65] S. Schiller, G. Beister, and W. Sieber. "Reactive high rate D.C. sputtering: Deposition rate, stoichiometry and features of TiO_x and TiN_x films with respect to the target mode". *Thin Solid Films*, **111**, 1259 (1984).

[66] M. Dumm, M. Zoelfl, R. Moosbuhler, M. Brockmann, T. Schmidt, and G. Bayreuther. "Magnetism of ultrathin FeCo (001) Films on GaAs (001)". *J. Appl. Phys.*, **87**, 5457 (2000).

[67] M. Zoelfl, M. Brockmann, M. Koehler, S. Kreuzer, T. Schweinboeck, S. Miethaner, F. Bensch, and G. Bayreuther. "Magnetic films epitaxially grown on semiconductors". *JMMM.*, **175**, 16 (1997).

[68] M. Dumm, B. Uhl, M. Zolfl, W. Kipferl, and G. Bayreuther. "Volume and interface magnetic anisotropy of $Fe_{1-x}Co_x$ thin films on GaAs(001)". *J. Appl. Phys.*, **91**, 8763 (2002).

[69] M. Sperl. "Temperaturabhngigkeit der Magnetisierung in ultraduennen epitaktischen FeCo-Schichten mit verschwindender Kristall-Anisotropie". Diplomarbeit, *Institut für Experimentelle und Angewandte Physik, Universität Regensburg* (2004).

[70] E. Y. Tsymbal and D. G. Pettifor. "Perspective of giant magneto resistance". *in Solid State Physics, **ed. H. Ehrenreich and F. Spaepen** (Academic press 2001)*, **56**, 113 (2001).

[71] K. E. Mello, S. R. Soss, S. P. Murarka, T.-M. Lub, and S. L. Lee. "Epitaxial quality of thin Ag films on GaAs(100) surfaces cleaned with various wet etching techniques". *Appl. Phys. Lett.*, **68**, 681 (1995).

[72] Z. Song, S. Shogen, M. Kawasaki, and I. Suemune. "X-ray photoelectron spectroscopy and atomic force microscopy surface stu dy of GaAs[100] cleaning procedures". *J. Vac. Sci. Technol. B*, **13**, 77 (1995).

[73] O. E. Tereshchenko, S. I. Chikichev, and A. S. Terekhov. "Composition and structure of HCl-isopropanol treated and vacuum annealed GaAs(100) surfaces". *J. Vac. Sci. Technol. A*, **17**, 2655 (1999).

[74] A. Spitzer. "Schottky-Kontakte auf GaAs". Diplomarbeit, *Institut für Experimentelle und Angewandte Physik, Universität Regensburg* (2004).

[75] S. van Dijken, X. Jiang, and S. S. P. Parkin. "Nonmonotonic Bias Voltage Dependence of the Magnetocurrent in GaAs-Based Magnetic Tunnel Transistors". *Phys. Rev. Lett.*, **90**, 197203 (2003).

[76] R. T. Tung. "Recent advances in Schottky barrier concepts". *Mater. Sci.Eng. R*, **35**, 1 (2001).

[77] R. T. Tung. "Electron transport at metal-semiconductor interfaces: General theory". *Phys. Rev. B*, **45**, 13509 (1992).

[78] J. P. Sullivan, R. T. Tung, and M. R. Pinto. "Electron transport of inhomogeneous schottky barriers: A numerical study". *J. Appl. Phys.*, **70**, 7403 (1991).

[79] B. Oliver and J. Nowak. "Temperature and bias dependence of dynamic conductance–low resistive magnetic tunnel junctions". *J. Appl. Phys.*, **95**, 546 (2004).

[80] W. H. Butler, X.-G. Zhang, T. C. Schulthess, and J. M. MacLaren. "Spin-dependent tunneling conductance of $fe|mgo|fe$ sandwiches". *Phys. Rev. B*, **63**, 054416 (2001).

[81] S. Gu-zo, P. Turban, C. Lallaizon, J. C. L. Breton, P. Schieffer, B. L-pine, and G. J. z quel. "Spatially resolved electronic properties of MgO/GaAs(001) Tunnel barrier studied by ballistic electron emission microscopy". *Appl. Phys. Lett.*, **93**, 172116 (2008).

[82] E. Heindl, C. Kefes, J. Vancea, and C. H. Back. "Hot electron spin attenuation lengths of bcc Fe_34 Co_66 - Room temperature Magnetocurrent of 1200 %". *to be published.*

[83] X. Jiang, S. van Dijken, R. Wang, and S. S. P. Parkin. "Bias voltage dependence of magnetocurrent in magnetic tunnel transistors". *Phys. Rev.*, **69**, 014413 (2004).

[84] E. Heindl. "Ortsaufgeloeste magnetische Charakterisierung von Tunnel Transistoren mit Ballistischer Elektronen Emissions Mikroskopie (BEEM)". Diplomarbeit, *Institut für Experimentelle und Angewandte Physik, Universität Regensburg* (2006).

[85] R. Jansen, T. Banerjee, B. G. Park, and J. C. Lodder. "Probing momentum distributions in magnetic tunnel junctions via hot-electron decay". *Appl. Phys. Lett.*, **90**, 192503 (2007).

[86] S. van Dijken, X. Jiang, and S. S. P. Parkin. “Comparison of magnetocurrent and transfer ratio in magnetic tunnel transistors with spin-valve bases containing Cu and Au spacer layers”. *Appl. Phys. Lett.*, **82**, 775 (2003).

[87] I. Appelbaum and V. Narayanamurti. “Monte Carlo calculations for metal-semiconductor hot-electron injection via tunnel-junction emission”. *Phys. Rev. B*, **71**, 045320 (2005).

[88] R. Vlutters, O. M. J. van t́ Erve, S. D. Kim, R. Jansen, and J. C. Lodder. “Interface, Volume, and Thermal Attenuation of Hot-Electron Spins in Ni_{80} Fe_{20} and Co”. *Phys. Rev. Lett.*, **88**, 027202 (2002).

Acknowledgement

During the four and a half years of my PhD thesis I have enjoyed working in two different labs. I would like to thank everyone at the Lst. Back and at INESC-MN for their helping me accomplishing this project. Many people have contributed in a way or another to this thesis and I would like to address my special thanks to:

- First of all of course, Prof. Dr. Guenther Bayreuther for allowing me to pursue my PhD on this exciting and challenging topic, for his constant involvement and support to this project.
- Prof. Dr. Christian Back for giving me the chance of doing this PhD at his chair as well as his guidance.
- Dr. Georg Woltersdorf for his continuous help and the many interesting discussions.
- Prof. Dr. Paulo Freitas and Dr. Susana Freitas for welcoming me at INESC and for being competent, understanding and supporting supervisors
- All the members of the "ultrasmooth" Marie Curie research and training network whitout which I wouldn't have started this PhD in the first place.

Of course, many other people have been of tremendous help over the course of this PhD among which and in no specific order, Alex W, Alex S, Bjorn, Matthias S, Matthias K, Eva, Bernie, Phillip, Martin D, Martin B, Thomas, Roland, Peter, Manu, Uli, Frank, Tobi, Dieter, Friedl, Anja, Claus, Romain, Thibaut and Ricardo. It is my hope that I have been able to provide them with at least a small help in return.

Finally and most importantly, I would like to thank may family friends and of course Madzi for their unconditional moral support.